Quantitative imaging of magnetization transfer parameters in vivo using MRI

John G. Sled

Department of Electrical and Computer Engineering

McGill University, Montreal

December, 2000

A thesis submitted to the Faculty of Graduate Studies and Research in partial fulfillment of the requirements of the degree of Doctor of Philosophy.

Abstract

MAGNETIZATION transfer (MT) imaging is a relatively new magnetic resonance imaging (MRI) technique that generates contrast dependent upon the phenomenon of magnetization exchange between semi-solid macromolecular protons and water protons. This technique has the ability to indirectly image semi-solids, such as protein matrices and cell membranes, whose magnetization dies away too quickly to be imaged directly. Preliminary in vitro and in vivo results suggest that MT quantification may allow improved characterization of the pathologically heterogeneous lesions of multiple sclerosis (MS) by providing a measure of demyelination. However, MT imaging, as currently applied, is only a semi-quantitative technique that reflects a complex combination of tissue and experimental parameters in addition to MT.

In this thesis a novel quantitative imaging technique is described that yields all of the observable properties of the binary spin bath model for MT. Based on a new model of the steady-state behavior of the magnetization during a pulsed MT-weighted imaging sequence, as well as new methodological developments in MRI relaxometry, this approach yields parametric images of the fractional size of the restricted pool, the magnetization exchange rate, the T_2 of the restricted pool and the relaxation times in the free pool. Validated experimentally on agar gels and samples of uncooked beef, the method is demonstrated in studies of two normal subjects and a patient with multiple sclerosis.

Résumé

Le transfert de magnétisation (le TM) est une nouvelle technique en imagerie par résonance magnétique (l'IRM) où le contraste dépend de l'échange de magnétisation entre les protons des macromolécules semi-solides et les protons de l'eau. Puisque la magnétisation des semi-solides, tel les matrices de protéines et les membranes cellulaires, s'atténue trop rapidement, la formation d'images doit se faire indirectement. Les résultats préliminaires in vitro et in vivo suggèrent que la quantification du TM permet une meilleure caractérisation des lésions hétérogènes de la Sclérose en Plaques puisqu'elle peut quantifier la sévérité de la démyélinisation . Cependant, la méthode de TM utilisée présentement en imagerie clinique demeure semi-quantitative et dépend, en plus du TM, de plusieurs facteurs expérimentaux et tissulaires.

Cette thèse décrit une nouvelle technique d'imagerie quantitative qui permet une mesure de toutes les propriétés observables du modèle binaire de TM *spin bath*. Basée sur un nouveau modèle de la magnétisation l'état d'équilibre pendant une séquence pulsée d'imagerie pondérée en TM , ainsi que sur certains nouveaux développements méthodologiques en relaxométrie de l'IRM, cette technique génère des images paramétriques de la concentration relative des spins restreints, du taux d'échange de magnétisation, du T_2 des spins restreint, et des temps de relaxation des spins libres. La méthode est validée expérimentalement avec des gels d'agar et des échantillons de boeuf cru. Elle est aussi appliquée sur deux sujets normaux ainsi que sur un patient souffrant de Sclérose en Plaques.

Acknowledgments

I am grateful to many people for the support and assistance that has made this thesis possible: Jeff Atkinson, Brad Gill, Valentina Petre, and Bojana Stefanovic for their assistance in acquiring the MRI data; Sridar Narayana and Douglas Arnold for their assistance in acquiring the MS patient data; and also Gabriel Léger and Sylvain Milot for their help in translating the abstract to French. I would like to express my appreciation for the guidance and insight that my supervisor, Bruce Pike, has provided at every stage of this work. Lastly, I would like to thank Noor, my wife, for her support and encouragement throughout.

In addition, I would like to acknowledge the financial support I have received from the Natural Sciences and Engineering Research Council of Canada (NSERC) and Hydro Quebec, for which I am grateful.

Preface

This monograph is closely based on four papers:

J. G. Sled and G. B. Pike. Standing-wave and RF penetration artifacts caused by elliptic geometry: an electrodynamic analysis of MRI. *IEEE Transactions on Medical Imaging*, vol. 17, no. 4, pp. 653–662, 1998.

J. G. Sled and G. B. Pike. Correction for B_1 and B_0 variations in quantitative T_2 measurements using MRI. *Magnetic Resonance in Medicine*, vol. 43, no. 4, pp. 589–593, 2000.

J. G. Sled and G. B. Pike. Quantitative interpretation of magnetization transfer in spoiled gradient echo MRI sequences. *Journal of Magnetic Resonance*, vol. 145, pp. 24–36, 2000.

J. G. Sled and G. B. Pike. Quantitative imaging of magnetization transfer exchange and relaxation properties in vivo using MRI. *Magnetic Resonance in Medicine*, (submitted) September 2000, *I.I. Rabi Young Investigator Award competition paper*.

At the time of this writing, three have been published and the forth is under review. The first paper is briefly summarized within the main text and included in full as an appendix. The second appears as part of Chapter 5 in manuscript form. The remaining two have been seperated into parts so as to fit the organization of this monograph.

Contributions of authors

The contributions of the two authors, John G. Sled and G. Bruce Pike, to the papers which are part of this work should be clarified as follows. Mr. Sled, in the capacity of doctoral candidate, developed the methodology, conducted the experiments, and wrote the bulk of the text of these papers, while Dr. Pike as the candidate's supervisor provided guidance, mentorship, and supervison of the project.

Contents

Abstract **ii**

Résumé **iii**

Acknowledgments **iv**

Preface **v**

Contributions of authors **vi**

Contents **x**

List of figures **xii**

List of tables **xiii**

1 Introduction **1**

2 A review of magnetization transfer **4**

3 Modeling pulsed magnetization transfer **12**

3.1 Methods 12

3.1.1 Modeling pulsed MT sequences 12

3.1.2 Outline of experiments . . . 15
3.1.3 A signal equation for pulsed MT sequences . . . 16
3.1.4 Numerical simulations . . . 18
3.1.5 Experimental validation . . . 18
3.1.6 Parameter estimation . . . 21
3.2 Results . . . 22
3.2.1 Numerical simulations . . . 22
3.2.2 Experimental validation . . . 23
3.2.3 Parameter images . . . 30
3.3 Discussion . . . 31
3.4 Derivation of the MTSPGR signal equation . . . 36

4 Field variations and quantitative imaging 39

4.1 Theory of field variations and imaging . . . 40
4.1.1 Methods . . . 41
4.1.2 Results . . . 44
4.1.3 Discussion . . . 47
4.2 Measuring field variations . . . 50
4.2.1 Measuring the main magnetic field . . . 50
4.2.2 Measuring the RF field . . . 52

5 Relaxometry of the free pool 54

5.1 Quantitative T_2 measurements . . . 55
5.1.1 Introduction . . . 55
5.1.2 Methods . . . 57
5.1.3 Results . . . 63

5.1.4 Discussion and conclusion 65
5.2 Quantitative T_1 measurements 67

6 Magnetization transfer imaging **72**

6.1 Theory 72
6.2 Parameter estimation 74
6.3 Experiments 77
6.3.1 Validation 79
6.3.2 In vivo experiments 80
6.4 Results 80
6.4.1 Validation results 80
6.4.2 In vivo results in normals 82
6.4.3 In vivo results in an MS patient 84
6.5 Conclusion 86

7 Discussion and conclusions **87**

7.1 Quantitative magnetization transfer imaging 87
7.2 Future work 90
7.3 Summary and conclusions 91

A Radio frequency field variations **93**

A.1 Introduction 94
A.2 Methods 97
A.2.1 Modeling the excitation field and reception sensitivity 97
A.2.2 Simulating spin echo images 104
A.2.3 Phantom studies 105
A.2.4 Comparing fields and images 107

A.3 Results 108
A.3.1 Variations in field strength 108
A.3.2 Simulated spin echo images 111
A.3.3 Pulse sequence sensitivity 111
A.3.4 Influence of media properties 113
A.3.5 Comparison with phantom studies 115
A.3.6 Field variations in the human head 118
A.4 Discussion 118
A.5 Conclusions 121
A.6 Computing an approximate solution 121

Bibliography **123**

List of figures

3.1 Comparison of ODE solutions with variants of the MTSPGR signal equation 24

3.2 Fitted curves for type I and type V experiments 26

3.3 Comparison of parameter estimates for various experimental designs 29

3.4 Parameter images based on a simultaneous fit of type IV and type V experiments 30

4.1 Simulated spin echo images 45

4.2 Comparison of predicted and measured excitation fields 47

4.3 Comparison of predicted and measured spin echo images 48

4.4 Pulse sequence schematic for B_0 measurements 51

4.5 Pulse sequence schematic for B_1 measurements 53

5.1 Observed T_2 for a multi-echo experiment 60

5.2 Steps for the quantitative T_2 sequence 61

5.3 Quantitative T_2 images for the cylindrical phantom 64

5.4 Quantitative T_2 images in brain 65

5.5 Excitation profile for Look-Locker T_1 sequence. 70

5.6 Flip angle compensation for slice profile effects in estimating T_1. 71

6.1 An MT-weighted spoiled gradient echo pulse sequence 75

6.2 Decomposition of the MT-weighted imaging sequence 76
6.3 A fit of the signal equation to MT data for uncooked beef 81
6.4 Parameter images for a normal subject 83
6.5 The signal equation fit to in vivo measurements 83
6.6 Parameter images for a patient with multiple sclerosis 85

A.1 Elliptic cylinder geometry and coordinate system 99
A.2 Signal intensity versus B_1 field strength 106
A.3 Magnitude contours of B^+ 110
A.4 Simulated spin echo images 112
A.5 Comparison of simulated spin echo images 114
A.6 Comparison of predicted and measured excitation fields 116
A.7 Comparison of predicted and measured spin echo images 117
A.8 Field map for a human subject 119

List of tables

3.1 Model parameters for 2%, 4%, and 8% agar 15

3.2 Summary of experiments 20

3.3 Parameter estimates for agar gels 28

3.4 Parameter estimates for agar gels derived from parameter images 32

5.1 Average T_2 for cylinder compartments before and after correction 64

6.1 MT-weighted pulse sequence parameters. 78

6.2 Parameter estimates for grey and white matter 84

6.3 Parameter estimates from four ROIs on a scan of an MS patient. 86

A.1 Summary of excitation field comparisons 116

A.2 Summary of spin echo image comparisons 118

Chapter 1

Introduction

MAGNETIZATION transfer (MT) imaging is a relatively new MRI technique that generates contrast dependent upon the phenomenon of magnetization exchange between semi-solid macromolecular protons and water protons. This technique has the ability to indirectly image semi-solids, such as protein matrices and cell membranes, whose signal decays too rapidly to be imaged directly. Preliminary in vitro and in vivo results suggest that MT quantification may allow characterization of the pathologically heterogeneous lesions of multiple sclerosis (MS) by providing a measure of demyelination. However, MT imaging, as currently applied, is only a semi-quantitative technique that reflects a complex combination of tissue and experimental parameters in addition to MT.

This thesis addresses the problem of measuring, in vivo, parametric images of the exchange rates, relaxation properties, and concentrations that characterize the MT phenomenon. To this end, a new approach is described for modeling imaging experiments that employ pulsed off-resonance irradiation to achieve MT contrast. Integral to this approach are a number of approximations that allow the derivation of a closed form solution for the signal from MT-weighted imaging pulse sequences in which the magnetization is in steady state. The speed with which the signal equation can be computed makes it feasible to esti-

mate the parameters that characterize the MT phenomenon by fitting the signal equation to each voxel in a set of MT weighted measurements.

While the development of the signal equation gives a theoretical basis for quantitative MT imaging, accounting for experimental factors and the relaxation mechanisms not associated with MT is essential to the accuracy and reproducibility of these measurements. Given the reliance of MT experiments on saturation from relatively intense radio-frequency (RF) irradiation, the main experimental factor to consider is the spatial variation in the RF field strength. The symmetries inherent in these variations and their implications for imaging are elucidated by an analysis from first principle of the interaction between the RF excitation field and the subject. On the basis of this work it is made clear that the most direct and practical means of compensating quantitative measurements for these RF field variations is to measure the fields directly on a subject-by-subject basis.

Besides the need for MT-weighted measurements, a complete characterization of the MT phenomenon requires measurement of the T_1 and T_2 relaxation times of the water protons. The approach of using in vivo field measurements to account for spatial variations in the excitation field is adapted to T_2 and T_1 relaxometry through the use of angular momentum theory. This novel approach is of particular relevance for T_2 studies with many closely spaced echoes that are needed to produce T_2 spectra.

Drawing together these developments, specifically in modeling the phenomenon, efficient parameter estimation, compensation of image artifacts, and relaxometry, the final chapters of the thesis describe a complete protocol for in vivo quantitative imaging of the parameters that characterize MT. These intrinsic parameters have a physical interpretation that can be used to study structural changes in by both normal and pathological tissue. The application of this approach is demonstrated by in vivo studies of the head in normal subjects and an MS patient. By distinguishing changes in the properties of the semi-solid pool

of protons from those of the surrounding water, the ambiguity that hampers the interpretation of current clinical MT imaging techniques is eliminated.

Chapter 2

A review of magnetization transfer

MAGNETIZATION transfer is a phenomenon observed using magnetic resonance in which spins in two or more distinct magnetic environments exchange magnetization either by through-space cross-relaxation or chemical exchange. Among the many applications of this phenomenon in nuclear magnetic resonance (NMR), the one of interest for in vivo human imaging is that in which the ^{1}H atoms bound to free moving water molecules, which provide the signal normally observed in MRI, exchange magnetization with ^{1}H atoms bound to molecules with comparatively restricted motion. Without the benefit of rapid tumbling these slower moving spins exist in a relatively stable but heterogeneous magnetic environment which causes them to lose coherence on a time scale orders of magnitude too short ($T_2 < 100\,\mu$s) to allow imaging with current MRI technology. However, by taking advantage of magnetization exchange [41, 84] between the free and restricted environments, one can indirectly determine the properties of the ^{1}H atoms in the restricted environment and by extension the molecules to which they are bound.

Initial biological experiments based on magnetization transfer (MT) [35, 36, 43, 44, 74] described the phenomenon in terms of an exchange of spins between bulk water and water molecules on the surface of macromolecules, the so-called hydration layer. These spin-

s in the hydration layer in turn exchange with ^{1}H atoms at the periphery of the macromolecules and then diffuse through the bulk macromolecular protons. Interpreting the MR behaviour of such a system is a general case of a solid-liquid mixture with overlapping resonances [140]. A useful simplification of the problem is to model the system as having two pools of ^{1}H atoms, having either relatively free ($^1\mathrm{H_f}$) or relatively restricted ($^1\mathrm{H_r}$) motion. McConnell proposed such a model as a modification to the Bloch equations which accounts for exchange of a single chemical species between two magnetic environments. These equations, expressing exchange in terms of first order rate constants, are equivalent [65] to those derived by Solomon [141] for the through-space cross-relaxation of two non-equivalent spins. Known collectively as the binary spin bath model, this system exhibits dual-exponential recovery of longitudinal magnetization (T_1 recovery) and mono-exponential decay of transverse magnetization (T_2 decay).

Characterizing the binary spin bath model by these decay rates yields little insight since the observed T_2 is that of the free pool and the longitudinal recovery rates reflect a combination of the underlying relaxation properties, exchange rate, and pool sizes. Teasing out the individual model parameters requires one to make a number of measurements on the system while selectively modifying the magnetization state of one of the two pools. An approach that yields the cross-relaxation rate [6, 20, 41, 161] first described by Forsen and Hoffman [41] is to selectively saturate the restricted pool while leaving the free pool unchanged. The difference in the longitudinal recovery rate (the apparent T_1) measured with and without saturation determines the cross-relaxation rate. However, the validity of implementing this approach using off-resonance irradiation is in doubt [64] both on the grounds of saturating the restricted pool and avoiding direct saturation of the free pool.

An alternative approach to characterizing the binary spin bath model proposed by Edzes and Samulski [35, 36] is to selectively invert the spins of the free pool and determine the

exchange rate and relative pool size from the two longitudinal recovery rates for the inverted system [35, 36, 49, 96]. A related approach [51, 48] employs two $\pi/2$ pulses to tip the free pool magnetization into the transverse plane and then back again so as to partially saturate the restricted pool through magnetization exchange during the interval between the two pulses. A limitation of both of these approaches is that they yield only the exchange and not the relaxation properties of the restricted pool.

An approach that overcomes this limitation is to characterize the steady-state response of the system to off-resonance irradiation and determine the relaxation properties from the so-called Z-spectra [53, 54] that are obtained. While the resonance frequency for the free and restricted pools are in general the same, the short T_2 of the restricted pool makes it sensitive to a much broader range of irradiation frequencies. Hence, irradiation sufficiently offset from the resonance frequency will selectively saturate the restricted pool with only limited direct saturation of the free pool. By measuring the steady-state response of the system at a number of offset frequencies, a property that can be readily determined is the linewidth of the restricted pool and hence its T_2. In combination with a field gradient used during the irradiation period [144], such data can be acquired rapidly in a spectrometer.

Following the introduction of Z-spectroscopy, the methodology underwent a number of refinements. Accounting for direct saturation of the free pool [163] by the off-resonance irradiation substantially improved the agreement with experimental data for small offset frequencies. A more subtle refinement is the inclusion of exchange of transverse magnetization in the model [164]. However, this correction is often safe to neglect since the T_2 of the restricted pool is so much shorter than that of the free pool. With the exchange of transverse magnetization largely in one direction, the apparent T_2 of the free pool including exchange is almost indistinguishable from that of a system having a shorter T_2 for the free pool and no transverse exchange.

Further refinements to the binary spin bath model came in the treatment of the restricted pool. The spectral lineshape of a system described by the Bloch equations is inherently Lorentzian and hence appropriate for liquids. By replacing the Bloch equations for the restricted pool in the spin bath model with a single longitudinal component [64, 145] described by a Gaussian lineshape, typical for solids, the model was extended to accurately characterize MT in agar gel [64]. The freedom to choose a lineshape for the restricted pool is complicated by the fact that not all materials fit either the limiting case of a liquid-like Lorentzian lineshape or a solid-like Gaussian lineshape. In bovine serum albumin solutions, a transition from a Lorentzian to Gaussian lineshape has been observed in MT experiments [69] as the concentration increases. Intermediate cases arise when the directions of molecular motion that causes the narrowing of the lineshape are restricted [23], such as in polymers, liquid crystals, biological membranes, and molecules adsorbed on surfaces. In tissues, a lineshape called a super-Lorentzian has been found to accurately characterize the restricted pool [97]. First observed in lamellar liquid crystals [158] and later in cells [11, 12], this lineshape is postulated to arise in biology when the motion of individual molecules is limited to a particular direction by the orientation of membranes and the like while the orientation of the membranes themselves is random such that the ensemble of molecules has no preferred direction. Given sufficient data, one need not be restricted to a parametric lineshape and may instead derive the lineshape from the data [80].

Although the reduction of the Bloch equations to a single longitudinal component can be justified by a geometrical argument [81] for weak irradiation and short T_2, this approach has an earlier precedent, the Redfield-Provotorov theory of spin temperature in solids [50]. In the absence of transverse magnetization, a system can be described by a spin temperature whose inverse is analogous to longitudinal magnetization. For experiments on a clinical MR scanner, the time scale is short enough and the irradiation weak enough compared to

the main magnetic field B_0 that the Zeeman and dipolar terms in the Hamiltonian have their own associated temperatures. This additional pool of spins, termed the dipolar reservoir, is easily incorporated into the spin bath model [98, 166].

Given that a variety of magnetization transfer systems are well characterized by the binary spin bath model, how should the model be interpreted in terms of the more complex picture of bulk water, hydration layers, peripheral and bulk macromolecular protons? While Edzes and Samulski [36] proposed that spin temperature differences could arise between peripheral and bulk macromolecular protons, subsequent studies have consistently assumed (with the exception of [18]) that a single temperature is sufficient to describe the macromolecular protons. With respect to the hydration layer, Koenig and others [18, 74, 80] have argued that these spins are in a state of rapid exchange with bulk water since bonds between the water molecules and macromolecules last on the order of 300 ps. Based on this interpretation, the two pools of the binary spin bath model correspond to bulk water protons and bulk macromolecular protons respectively. However, some authors have proposed that a third, intermediate, proton pool is needed to explain experimental data in tissue [3, 140]. Contrary to the usual interpretation, the results of Adler et al. [3] suggest that the intermediate pool, nominally the hydration layer, exchanges more rapidly with the macromolecular pool than the bulk water. A difficulty with such experiments is that a close fit to experimental data does not on its own validate the model. Several authors have proposed alternative models for tissue in which more than one MT process is present [29, 142, 147].

Parallel to the development of a physical model for MT has been the development of imaging applications that take advantage of magnetization transfer dependent contrast (MTC). Imaging using MTC was first demonstrated by Wolff and Balaban [161] in rabbit kidney using continuous-wave (CW) off-resonance irradiation to partially saturate the restricted pool. This approach can be used both to provide image contrast [103, 161]

and to determine of model parameters in a manner analogous to an NMR experiment [117, 118, 119]. However, since CW irradiation is generally not available for clinical MRI scanners, the majority of human MT imaging has been performed using shaped off-resonance RF pulses [107, 126, 128] or short intense on-resonance binomial RF pulses [67, 66, 113, 108, 114, 127, 167, 71, 90, 59, 27]. In either case the pulses are designed to selectively saturate (at least partially) the short T_2 semi-solid spins without any direct effect on the liquid component(s) [55, 56, 57, 112, 125]. In an attempt to isolate MT effects, acquisitions are often performed with and without $^1\mathrm{H_r}$ saturation pulses to compute ratio or percent difference images (so called MTR images).

The use of pulsed irradiation to generate MT contrast requires further refinement of the physical model. A number of authors have described analytic methods for computing the transient behaviour of the binary spin model in response to step changes in irradiation [4, 122, 168, 165, 166]. However, there has been a discrepancy in the analysis of pulsed experiments with respect to generalizing the behaviour of the restricted pool; the irradiation induced transition rate has either been assumed constant [55, 58] or time-varying [4, 108, 122, 168, 165, 166]. This question of the treatment of pulsed irradiation is considered further in Chapter 3.

The ease with which MT contrast can be incorporated into standard imaging protocols [61, 120, 162] and the novelty of the resulting contrast has led to a multitude of MTC applications. These include mild head trauma [92], frontal lobe epilepsy [37], muscular dystrophy [91], brain tumours [102], ischemic vascular dementia [146], CNS tuberculosis [60], and Alzheimer's disease [62]. However, MTC is most commonly associated with the study of white matter in patients with multiple sclerosis (MS).

While the exact mechanisms of MT in white matter are not known, its importance has been clearly established [8, 33, 42, 73, 75]. Cholesterol [73, 72] and sphingomyelin [21]

have been suggested to be the dominant constituents of myelin responsible for MT; however, the most comprehensive in vitro analysis has been performed by Kucharczyk et al. [75] who studied all the major lipid components of white matter in a multilamellar vesicle model system and measured T_1, T_2, and MT at varying pH. They observed that galactocerebroside had the greatest effect on relaxivity and that the MT effect produced was two to three times greater than with either cholesterol or sphingomyelin alone.

While the use of MTC in studies of MS has produced intriguing results that have led to its use in MS clinical trials, the reduction of the entire MT phenomenon to a single MTR value has left the interpretation of these results incomplete and somewhat controversial. What is widely accepted is that a large reduction in MTR within MS lesions is an indicator of demyelination and tissue damage. There are several lines of evidence to support this [17, 40] including: animal models with histopathological correlations [32, 31, 79]; in vivo human studies of purely demyelinating diseases such as leukoencephalopathies [30, 77, 130] and; a post mortem study of MS patients [154].

Perhaps more interesting than large MTR reductions within lesions are the small reductions observed in normal appearing white matter [32, 38, 45, 83, 94, 109]. It has been observed [39, 52, 110, 111] that focal MTR reductions antedate the appearance of MS lesions on conventional T_2-weighted scans. One explanation for the MTR abnormalities in normal appearing white matter is the presence of microscopic or biochemical pathology not directly visualized on the conventional MR images [32, 38, 39, 82]. Another factor that may contribute is Wallerian degeneration remote from observed focal lesions [79]. Alternatively, the small MTR reductions may be of a purely edematous origin with no significant myelin degradation. In any event, the detection of diffuse pathology provides strong support for the use of global assessments of disease using methods such as whole brain MTR histograms [68, 105, 106, 121, 152, 153].

While MTR values are quantitative in the sense that they are reproducible and comparable among subjects and repeated scans [9, 131], the resulting images reflect a complex combination of sequence and relaxation parameters in addition to MT [108, 113]. Moreover, characterizing the MT phenomenon by a single value prevents a physical interpretation and overlooks potentially useful diagnostic information. In an effort to overcome this limitation of MT imaging techniques, a number of authors have proposed methods that yield intrinsic properties based on the binary spin bath model. Quesson et al. [119, 118] have described a technique similar to an NMR experiment in which continuous-wave off-resonance irradiation is used to prepare the magnetization before performing conventional imaging. Lee and Dagher [76] proposed a similar technique with fewer measurements that yields only the fractional size of the restricted pool. An alternate technique, yielding all of the parameters of the binary spin bath model, described by Chai et al. [22] measures the approach to steady state for trains of binomial pulses of varying duty cycle and duration. Another method recently described by Gochberg et al. [49] saturates the restricted pool by successive inversions of the free pool so as to estimate the fractional size of the restricted pool and the relaxation properties of the free pool.

The challenges of developing a clinical imaging technique that yields exchange and relaxation properties based on the binary spin bath model are three fold. First, one needs to forgo the use of continuous-wave irradiation, which is not widely available, and the large power deposition that is typical of NMR experiments. Second, sufficient data to constrain all aspects of the model needs to be collected within a relatively short period, such as 30 to 60 minutes. And third, a computationally efficient model of the experiment is needed so that estimation of the model parameters at every voxel becomes feasible. Existing methods either do not meet all of these criteria or yield only a subset of the model parameters.

Chapter 3

Modeling pulsed magnetization transfer

In this chapter (based on [138]) a method is described for analyzing general pulsed MT experiments in which off-resonance saturation pulses are interleaved with on-resonance excitation (imaging) pulses. This method is applied to develop a signal equation for MT-weighted spoiled gradient echo sequences. Using this signal equation, various experimental designs are assessed for imaging the cross-relaxation rate, the fractional size of the restricted pool, and the relaxation times T_1 and T_2 of the two pools. Experiments on agar gels demonstrate the feasibility of using pulsed MT-weighted MRI sequences to rapidly produce quantitative images of the exchange and relaxation properties within an object.

3.1 Methods

3.1.1 Modeling pulsed MT sequences

The binary spin bath model is employed to describe a pulsed MT experiment in which spins exist in either of two magnetic environments. The magnetization of the so-called free pool is described by the Bloch equations while that of the restricted pool is modeled using the

Redfield–Provotorov theory [50]. A first order rate constant governs exchange between the two pools.

For experiments on clinical scanners, the time scale is short enough and the irradiation is weak enough compared to the main magnetic field B_0 that the Zeeman and dipolar terms in the Hamiltonian have their own associated temperatures. Expressed as five coupled differential equations the behaviour of the magnetization in such a system in a reference frame rotating at a frequency offset Δ from resonance is given by:

$$\frac{dM_{x,f}}{dt} = -\frac{M_{x,f}}{T_{2,f}} - \Delta M_{y,f} - \mathsf{Im}(\omega_1) M_{z,f} \tag{3.1}$$

$$\frac{dM_{y,f}}{dt} = -\frac{M_{y,f}}{T_{2,f}} + \Delta M_{x,f} + \mathsf{Re}(\omega_1) M_{z,f} \tag{3.2}$$

$$\frac{dM_{z,f}}{dt} = R_{1,f}(M_{0,f} - M_{z,f}) - k_f M_{z,f} + k_r M_{z,r} + \mathsf{Im}(\omega_1) M_{x,f} - \mathsf{Re}(\omega_1) M_{y,f} \tag{3.3}$$

$$\frac{dM_{z,r}}{dt} = R_{1,r}(M_{0,r} - M_{z,r}) - k_r M_{z,r} + k_f M_{z,f} - W M_{z,r} + W\beta' \tag{3.4}$$

$$\frac{d\beta'}{dt} = W\left(\frac{2\pi\Delta}{D}\right)^2 (M_{z,r} - \beta') - \frac{1}{T_D}\beta' \tag{3.5}$$

where the subscripts f and r denote the free and restricted pools and the subscripts x, y, and z denote the various components of a magnetization vector. $\beta' = \beta - \beta_0$, where β is the inverse spin temperature associated with the dipolar order of the restricted pool and β_0 is its equilibrium value in the absence of irradiation. T_D is the dipolar relaxation time. The excitation field strength, $\omega_1 = \gamma B_1$, is complex and time varying for general pulses with a circularly polarized coil. The parameter D is related to the linewidth of the restricted pool [50]; for a Gaussian lineshape this is given by $D^2 = 1/3T_{2,r}^2$. By definition, $k_r = k_f/F$ where $F = M_{0,r}/M_{0,f}$ is the ratio of the pool sizes.

The transition rate W for the saturation of the restricted pool is given for CW experiments in the absence of B_0 field gradients by

$$W = \pi\omega_1^2 G(\Delta) \tag{3.6}$$

where G is the lineshape function for the restricted pool. When G is a Lorentzian, the behaviour of the system approximates that of the Bloch equations for small $T_{2,r}$ [81]. Gaussian lineshapes have been found appropriate for solids and gels [64] as have super-Lorentzians for tissues [80]. If the system is assumed to be in steady state then more complex irradiation patterns than a continuous-wave can be accounted for by summing the transition rates of the various spectral components [55, 56].

For sufficiently short pulses the approximation that the magnetization of the restricted pool is constant during a repetition period of a pulse sequence may not be satisfactory. In such circumstances the transition rate W will be time varying. Treating the restricted pool as a causal linear system, the lineshape can be interpreted as the real part of a complex susceptibility function from which the impulse response of the system is readily computed to be

$$g(t) = \frac{2}{\pi} \int_0^\infty G(\Delta) cos(\Delta t) d\Delta \,, \quad t > 0 \,. \tag{3.7}$$

Convolving this response function with the instantaneous irradiation power yields the time varying transition rate

$$W(t) = \pi \omega_1^2(t) * g(t) \,. \tag{3.8}$$

However, for shaped MT pulses with bandwidths narrow compared to the linewidth, the transition rate can be approximated as

$$W(t) = \pi \omega_1^2(t) G(\Delta) \tag{3.9}$$

where Δ is the centre frequency of the off-resonance irradiation.

While equations (3.1)–(3.5) and (3.9) are proposed as an accurate model for describing pulsed MT experiments, in practice using these ordinary differential equations to estimate the parameters of the spin bath model from experimental data is computationally infeasible. Given that one needs to conduct a series of experiments in order to completely character-

ize the binary spin bath model and that, due to the complexity of the model, the process of estimation is inevitably iterative, one may need to numerically solve these equations upwards of ten million times for an imaging protocol. In subsequent sections a number of approximate solutions are described that lend themselves to rapid computation. These approximations were made in view of the experiments that are described briefly in the following section.

3.1.2 Outline of experiments

The signal equation has been validated using two acquisition strategies and various concentrations of agar gel, a material whose MT properties have been well characterized [64] in spectrometers by the binary spin bath model. Using a Gaussian lineshape for the restricted component and neglecting the dipolar reservoir, the model parameters reported by Henkelman et al. [64] at 1.5 T for 2%, 4%, and 8% agar are given in Table 3.1.

Table 3.1: Model parameters for 2%, 4%, and 8% agar based on CW experiments reported by Henkelman et al. [64]. The corresponding values of R_1^{obs} were $0.49 \pm 0.02\,\mathrm{s}^{-1}$, $0.68 \pm 0.03\,\mathrm{s}^{-1}$, and $1.14 \pm 0.05\,\mathrm{s}^{-1}$ respectively.

	2% agar	4% agar	8% agar
k_f	0.9 $\pm$0.1 s^{-1}	1.8 $\pm$0.2 s^{-1}	3.9 $\pm$0.5 s^{-1}
F	0.0051 $\pm$0.001	0.011 $\pm$0.002	0.022 $\pm$0.004
$R_{1,f}$	0.51 $\pm$0.07 s^{-1}	0.70 $\pm$0.10 s^{-1}	1.08 $\pm$0.16 s^{-1}
$R_{1,r}$	1 $\pm$1 s^{-1}	1 $\pm$1 s^{-1}	1 $\pm$1 s^{-1}
$T_{2,f}$	63 $\pm$8 ms	32 $\pm$4 ms	16 $\pm$2 ms
$T_{2,r}$	12.9 $\pm$0.1 μs	12.9 $\pm$0.1 μs	12.9 $\pm$0.1 μs

Two types of experiments were performed on agar gels. The first, referred to as a magnetization transfer prepared (MTP) sequence, consists of a train of shaped off-resonance pulses that drive the system into steady state after which the z magnetization of the free pool is measured using a 90° pulse. Phase cycling [13] rather than RF spoiling is used to select the FID of the 90° pulse so as to make this experiment analogous to the NMR experiments described in [64], in which a period of continuous-wave irradiation was used to drive the system into steady state before measurement with a 90° pulse.

The second type of experiment, a spoiled gradient-echo sequence (MTSPGR), has an MT pulse followed by a slice selective low angle excitation pulse and readout at every repetition. RF spoiling and crusher gradients are used to disperse transverse magnetization produced by the MT pulses and prevent the formation of stimulated echoes. When comparing the two types of sequences, one should refer to the repetition period for the MT pulse (T_{MT}) which for the MTSPGR sequence is the same as the repetition time of the excitation (TR).

3.1.3 A signal equation for pulsed MT sequences

One can predict the outcome of a pulsed MT experiment by numerically solving the ordinary differential equations (3.1)–(3.5) over a time interval long enough for a steady state to establish. This method is used as the standard for evaluating various approximate signal equations. Following the derivation of [108], the pulse sequences are decomposed into a number of stages for which the ordinary differential equations (ODEs) have simple exact or approximate solutions. Concatenating these solutions together and solving algebraically for the magnetization in steady state yields a signal equation that can be rapidly computed.

The differential equations have simple solutions in three cases, instantaneous pulsed excitation, continuous-wave excitation, and free precession. These solutions can be combined

in a number of ways. For example, concatenating the solution for a period of continuous wave excitation followed by a period without saturation yields the responses to an off-resonance rectangular pulse. More subtle treatments can be achieved by using different approximate solutions for the two pools.

Since the behaviour of the free pool near resonance tends to be complicated, neither a continuous-wave or rectangular pulse approximation is satisfactory. Instead the effect of an MT pulse on the free pool is modeled as an instantaneous fractional saturation of the longitudinal magnetization. This saturation fraction is computed by simulation of the Bloch equations taking into account the pulse envelope and $T_{2,f}$ decay, but neglecting exchange with the restricted pool and $R_{1,f}$ recovery. Neglecting these terms is compensated for by including $R_{1,f}$ recovery and exchange in the adjacent stages of the approximate sequence. This approach is taken to uncouple $T_{2,f}$ from $R_{1,f}$ and k_f thus limiting the number of parameters upon which the saturation fraction depends. With the saturation fraction only dependent on $T_{2,f}$ for a particular pulse envelope, these fractions, which are relatively expensive to compute, are computed in advanced and reused in subsequent calculations.

Two models are considered for the restricted pool, one in which it experiences continuous wave excitation of equivalent average power and another in which the MT pulse is replaced by a rectangular pulse having equivalent average power and a width equal to the full-width-at-half-maximum of the instantaneous pulse power $\omega_1^2(t)$. While the former model can take into account the bandwidth of the shaped pulses, this correction proved negligible for these experiments.

An additional variation that was considered was to neglect the dipolar term in the Hamiltonian. Altogether, this gave four models to evaluate, two variants of the signal equation each with and without the dipolar term. For each model, the excitation pulse was incorporated as an additional fractional saturation of the free pool and, due to its low power,

was not considered for the restricted pool. The formulas for the steady-state magnetization are given in section 3.4 at the end of this chapter.

3.1.4 Numerical simulations

Numerical simulations were used to investigate two aspects of the methodology. The first was to determine how closely the various signal equations predict the results of the numerical simulations, which are assumed to be correct. The second was to determine which pulse sequence designs yield the best predictions. While the latter was not pursued exhaustively, consideration was given to the five pulse sequences for which experimental data was also collected. Simulations with and without the dipolar terms were made for each of three materials having the properties of 2%, 4%, and 8% agar given in Table 3.1. These simulations were also used to assess bias in the parameter estimation technique described in section 3.1.6.

The numerical simulations were computed using a standard ODE solver in which the simulation was stopped when the difference in magnetization at the readout time differed by less than 0.05% from that at the previous repetition. Spoiling was modeled by setting the transverse components of the magnetization to zero after each MT pulse.

3.1.5 Experimental validation

The MTP sequences consisted of a 7.7 s train of MT pulses (for $T_{MT} = 15$ ms this corresponds to 512 pulses) followed by a 90° on-resonance excitation pulse and gradient echo readout with $TE = 4$ ms. Based on numerical simulations 7.7 s was sufficient to establish steady state for these experiments. The MT pulses used were Hanning windowed Gaussians with duration 10.24 ms or 30.72 ms (bandwidth 200 Hz and 67 Hz) whose offset frequency and power could be varied. Phase cycling of the 90° pulse in three repeated acquisition was

used to separate its FID from coherences generated by the MT pulses.

The MTSPGR experiments consisted of a gradient echo sequence with $TE = 4\,\text{ms}$ and $TR = T_{MT}$ either 50 ms or 25 ms. Excitation pulse angles of 10° and 7° were chosen for the two cases based on the MT contrast relative to noise determined by numerical simulation. A combination of strong crushing gradients and RF spoiling [170] was used to eliminate any residual transverse magnetization between repetitions. On the basis of numerical simulation, a period of 12.8 s of initial pulsing was determined to be sufficient to establish steady state and was used in all MTSPGR studies before data was acquired.

The agar gels for these experiments were prepared in cylindrical 1 litre bottles, 16 cm high. This allowed for a spectrum of offset frequencies to be tested in a single experiment by employing a linear field gradient [144] along the cylinder axis during the MT pulses. Since in practice a logarithmic series of frequency offsets is of interest, data were acquired in three stages, capturing a range from zero to 1 kHz, 10 kHz, and 100 kHz respectively.

The raw data from these experiments is biased by a combination of non-uniform coil sensitivity and non-uniform excitation (B_1) field strength ([135], appendix A), the later of which affects both the MT and excitation pulses. Rather than model the two effects, an additional gradient echo scan was collected without MT pulses which was used to estimate a smooth non-uniformity field [139] and normalize the intensity of the MTSPGR data. This approach compensates for reception sensitivity variations as well as variations in the excitation pulses. In addition, the main magnetic field variations (B_0) were measured using a phase difference imaging technique ([46], section 4.2.1) and the offset frequencies of the MT pulses were corrected accordingly.

A summary of the various experiments conducted using spatial encoding of MT offset frequency is given in Table 3.2. Each experiment was repeated for three different MT pulse angles (powers). The average irradiation power corresponding to each of the three pulses

is the same for each type of experiment.

Table 3.2: Summary of experiments using spatial encoding of MT offset frequencies.

Experiment	Type	TR	pulse duration	MT pulse angles			excitation angle
I	MTP	15 ms	10.24 ms	219°	438°	657°	90°
II	MTP	50 ms	30.72 ms	693°	1386°	2079°	90°
III	MTSPGR	50 ms	10.24 ms	400°	800°	1200°	10°
IV	MTSPGR	50 ms	30.72 ms	693°	1386°	2079°	10°
V	MTSPGR	25 ms	10.24 ms	283°	566°	849°	7°

As an additional experiment a series of MTSPGR images were used to compute parameter images for the various material properties. For this experiment pulse sequences IV and V were used with only the low and high power pulses. Each experiment was conducted for sixteen offset frequencies ranging from 800 Hz to 80 kHz. While these experiments were normalized using a scan without MT pulses as before, B_1 field strength was also measured using a modified stimulated echo pulse sequence [151] and used to correct the MT pulse power at each voxel. Images were made for a transverse section of the three gel bottles along with a bottle of 254 μM $MnCl_2$ solution.

The parameters k_f, F, $R_{1,f}$, $R_{1,r}$, $T_{2,f}$, and $T_{2,r}$ are not uniquely determined for experiments in the steady state [19]. Following the approach of [64], this was resolved by making an independent measurement of the apparent relaxation rate R_1^{obs} and estimating $R_{1,r}$. In the absence of irradiation, a binary spin bath system can be expected to relax with two spin-lattice relaxation rates. However, for typical inversion recovery experiments only

the longer of the two can be observed. Hence $R_{1,f}$ is related to R_1^{obs} by

$$R_{1,f} = \frac{R_1^{obs}}{1 + \left(\frac{\left[\frac{k_f}{R_{1,f}} \right] (R_{1,r} - R_1^{obs})}{(R_{1,r} - R_1^{obs}) + k_f/F} \right)} . \tag{3.10}$$

$R_{1,r}$ was chosen rather arbitrarily to be $1\,\mathrm{s}^{-1}$ with an uncertainty, for the purpose of error calculations, of $\pm 1\,\mathrm{s}^{-1}$. In practice, this has little impact on subsequent estimates of the other parameters.

R_1^{obs} was determined for each gel using a standard inversion recovery sequence with a TR of 2 s and a range of inversion times. Estimates were made using a non-linear least-squares fit to the data. For completeness the apparent T_2 of the gels was also measured using a 32 echo quantitative T_2 imaging sequence [115]. All experiments were conducted at 1.5 T on a Siemens Vision scanner (Siemens Medical Systems, Erlangen).

3.1.6 Parameter estimation

The material properties were estimated for each experiment by non-linear least-squares fitting of the MTSPGR signal equation with $T_{2,f}$, $T_{2,r}$, k_f, and F as independent parameters. The corresponding value of $R_{1,f}$ for each parameter estimate was determined using equation (3.10) and the estimates of R_1^{obs} and $R_{1,r}$. In practice a scale factor could also be included as a free parameter in the fit; however, since the data is normalized, this scale factor was fixed for each parameter estimate such that the signal magnitude in the absence of MT pulses is one. This same technique was employed to estimate the parameters used to generate the numerical simulations described in section 3.1.4.

For the purposes of parameter estimation, one need not be restricted to data from a single type of experiment. The material properties were also estimated based on a simultaneous fit to data from all five experiment types. In principle, the inversion recovery data

used to estimate R_1^{obs} could also be included in a simultaneous fit to the MT data. However, the precision of the R_1^{obs} estimates was such that this added complication was deemed unnecessary.

For the experiments in which frequency offsets were encoded spatially, the number of measurements was too large to process easily. For these experiments the data was approximated using cubic B-splines and sampled regularly in logarithmic steps from 300 Hz to 80 kHz with 10 samples per decade. For the imaging experiments, which had comparatively few measurements, no resampling was performed.

The MTP type experiments were analyzed using the same formula as for the MTSPGR experiments by taking the limit in which the excitation flip angle goes to zero. The analytic formula given by Henkelman et al. [64] for CW experiments can also be used to analyze the MTP type experiments. The two approaches differ in their handling of the free pool magnetization at small offset frequencies, where the simulation of the Bloch equations used in the MTSPGR signal equation differs from the Lorentzian lineshape approximation used in the CW equation. In practice, the two formulas agree closely for MTP experiments at offset frequencies greater than 1 kHz. However, the MTSPGR signal equation has the flexibility to take the duty cycle of the irradiation into account.

3.2 Results

3.2.1 Numerical simulations

In comparing the results of the ODE simulations to the predictions of the signal equations, the two were found to be generally in agreement. The residual differences, most noticeable for the 8% agar, followed a number of trends. At low frequency offsets, from 100Hz to 1 kHz, the signal equation consistently underestimates the simulation, likely as result of the

approximations used in modeling the free pool. This trend appears in all four cases shown in Figure 3.1. Since the effect of decreasing $T_{2,f}$ is to shift the low frequency portion of the curve to the right, one can expect this discrepancy to result in $T_{2,f}$ being overestimated. Parameters derived from simulations for each of the five experiment types were found to overestimate $T_{2,f}$ on average by 2 ms for each gel.

In the range 1 kHz to 10 kHz off-resonance, the deviation depended both on the variant of the signal equation and the type of experiment. In general, the rectangular pulse variant (RP) of the signal equation tended to slightly overestimate the signal in this range, while the continuous-wave variant would underestimate the signal either by a large or small amount depending on the type of experiments. This latter trend is consistent with experiments having short relatively intense pulses deviating from the CW model. Compare for example the curves in Figure 3.1a and Figure 3.1b. The latter, a type III experiment, has less frequent and more intense pulses.

In the absence of dipole interaction (i.e. $T_D \rightarrow 0$), the two variants of the signal equation were in good agreement with the ODE simulation beyond 10 kHz. Incorporating dipole interaction increased the deviation of the CW model variant from the ODE solution. Compare for example Figure 3.1b and 3.1d, where for the later the curves only converge just before the MT effect disappears around 30 kHz.

3.2.2 Experimental validation

For each agar gel and each experiment type the various material parameters were estimated by non-linear least squares fitting. On the basis of the numerical simulations of the previous section the analysis was restricted to the RP variant of the signal equation, looking at forms with and without the dipolar terms. The predictions of these two variants of the signal equation along with experimental data for an MTP and MTSPGR type experiment are

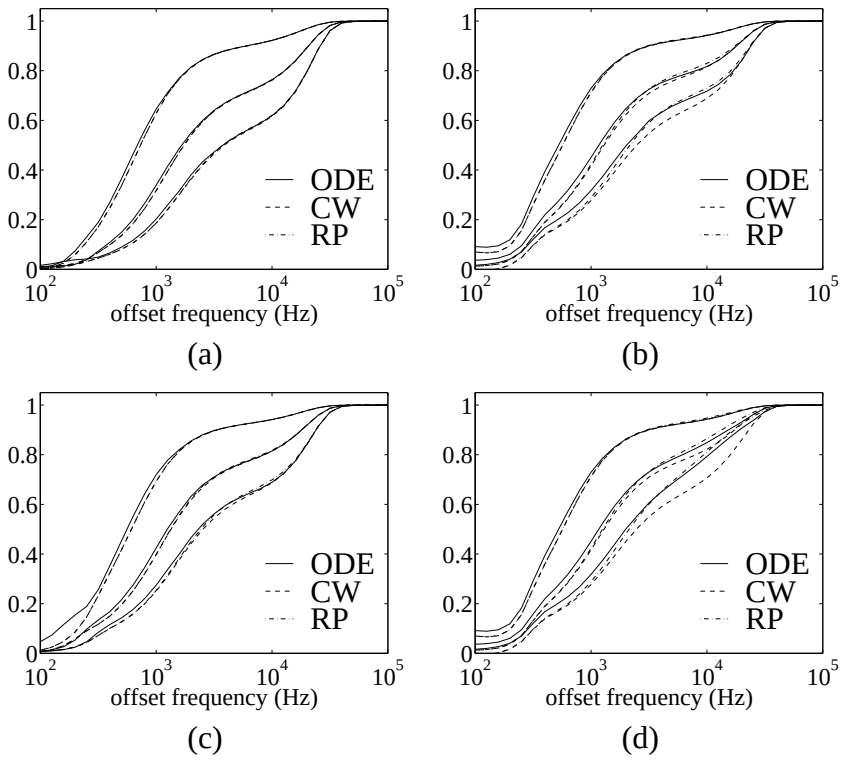

Figure 3.1: Comparison of ODE solutions with two variants of the MTSPGR signal equation for 8% agar. The two variants use the continuous-wave (CW) and rectangular pulse (RP) approximations for the restricted pool. The three curves shown for each case correspond to the three MT pulse powers used throughout (see Table 3.2). (a) Experiment type I, without dipole interaction (i.e. $T_D \to 0$). (b) Experiment type III, without dipole interaction. (c) Experiment type V, without dipole interaction. (d) Experiment type III, with dipole interaction ($T_D = 3\,\text{ms}$).

shown in Figure 3.2. While the parameter estimates derived from the two signal equations differ, the predicted signals are nearly identical except for small differences around 10 kHz for the MTSPGR experiment.

The RMS error for these fits is about 1% for the MTP experiment and 2% for the MTSPGR experiment. Much of the error in the latter is due to errors in the model for

small frequency offsets. Considering only offset frequencies greater than 800Hz, the RMS error for the MTSPGR experiment is about 1%. Attention should be restricted to this range of offset frequencies since the signal change observed at smaller offset frequencies is almost entirely due to direct saturation and largely independent of the MT properties of the material. Furthermore, the large rotations of the spins in the free pool caused by pulses near resonance are difficult to model accurately. The low frequency structure seen in the upper right panel of Figure 3.2 is characteristic of pulsed MT experiments in which the fractional saturation of the free pool due to an individual pulse initially oscillates as the offset frequency is increased.

While these fits, as shown by Figure 3.2 are generally close to the data, there are a number of systematic differences, statistically significant by a χ^2 test[1], that are not accounted for by random variations. While these deviations could be attributed to deficiencies in the signal equation, measurement drift and B_1 inhomogeneity may also be the cause. The latter may account for the mismatch, seen in Figure 3.2 at 8 kHz, between data collected for the three different ranges of offset frequencies, corresponding to the three gradient strengths.

To assess the effect of neglecting the dipole terms in the signal equation, we tested whether the difference between the resulting fitted curves was significant given the measurement noise. Using the test [14]

$$P\left\{Z > \frac{1}{2\sigma}\sqrt{\sum_i \left(m_{dp}(i) - m_z(i)\right)^2}\right\} < 1\%\,, \tag{3.11}$$

it was found that in every case the difference between the two was sufficient to choose the form with dipolar terms. $m_{dp}(i)$ and $m_z(i)$ in equation (3.11) are the points on the fitted curve corresponding to the ith measurement for each signal equation and σ is the standard deviation of the measurement noise. The improvement in fits by including dipolar terms

[1]The statistic $\chi^2/(df\,-\,1)$, where df is the number of degrees of freedom, averaged 45 for these fits, confirming the presence of systematic errors.

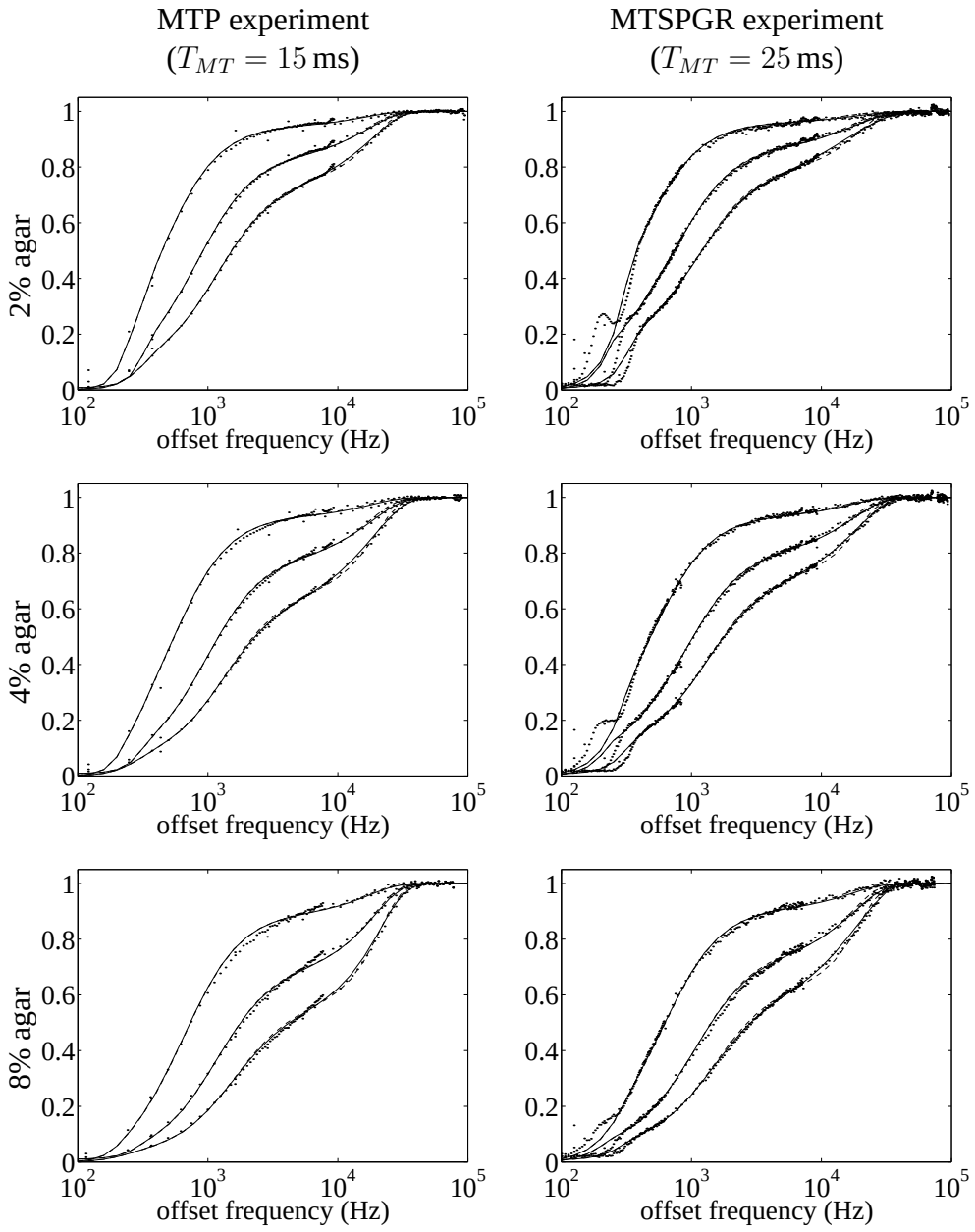

Figure 3.2: Fitted curves for type I and type V experiments. Dots are experimental data; the solid and dashed lines are for the RP variant of the signal equation with and without dipole interaction, respectively. Note that the solid and dashed lines are indistinguishable in most plots.

tended to be subtle, resulting on average in a 5% reduction in that portion of the residual error not accounted for by measurement noise.

In addition, neglecting the dipole terms was investigated by comparing the parameter estimates drawn from simultaneous fits of each model to all five experiment types for each gel. To assess the precision of these estimates the marginal uncertainty was computed for each parameter [7] using both the residual sum of squares error in the measurements and the uncertainties in R_1^{obs} and $R_{1,r}$. Based on the gradient of the objective function for each measurement, this yields a *t* statistic with $N - p$ degrees of freedom and a corresponding confidence interval for the parameter. Since the parameter estimates are based on the resampled data, the fraction of the residual error due to systematic errors is correspondingly larger. As a result, the error bounds on the parameters reflect both the precision or reproducibility of the measurements as well as the accuracy of the model. These parameter estimates and corresponding uncertainties are given in Table 3.3. R_1^{obs} determined from inversion recovery experiments was $0.410 \pm 0.006\, s^{-1}$, $0.504 \pm 0.02\, s^{-1}$, and $0.699 \pm 0.04\, s^{-1}$ respectively for the 2%, 4%, and 8% agar gels.

Inspection of Table 3.3 would suggest that neglecting the dipole terms in the model results in a slight underestimate of the restricted pool size F and the exchange rate k_f as well as a small overestimate of $T_{2,r}$. An analysis of variance of each parameter taking into account the large number of degrees of freedom in the individual entries reveals that only the reduction in F is statistically significant (tested at $p = 0.05$).

Note that $F/(1+F)$ is expected to be proportional to the concentration of gel. Regressing the F values in Table 3.3 using this relation shows the average deviation for F to be 0.0017, somewhat larger than the reported uncertainty. Subsequent results show that such bias tends to be correlated with bias in k_f and $T_{2,f}$.

The effect of experimental design on the parameter estimates was also investigated. In

Table 3.3: Parameter estimates for agar gels based on a simultaneous fit of the signal equation to the five experiments. Values are shown for a model with and without dipole interaction. Uncertainties are for a 95% confidence interval.

		2% agar	4% agar	8% agar
k_f	$*$	0.324 $\pm$0.09 s^{-1}	0.822 $\pm$0.25 s^{-1}	2.035 $\pm$0.56 s^{-1}
	$\diamond$	0.313 $\pm$0.08 s^{-1}	0.784 $\pm$0.23 s^{-1}	1.895 $\pm$0.52 s^{-1}
F	$*$	0.0092 $\pm$0.0011	0.0151 $\pm$0.0012	0.0302 $\pm$0.0016
	$\diamond$	0.0087 $\pm$0.0009	0.0140 $\pm$0.0009	0.0274 $\pm$0.001
$R_{1,f}$	$*$	0.405 $\pm$0.01 s^{-1}	0.497 $\pm$0.022 s^{-1}	0.690 $\pm$0.049 s^{-1}
	$\diamond$	0.406 $\pm$0.01 s^{-1}	0.497 $\pm$0.02 s^{-1}	0.691 $\pm$0.05 s^{-1}
$R_{1,r}$	$*$	1.0 $\pm$1.0 s^{-1}	1.0 $\pm$1.0 s^{-1}	1.0 $\pm$1.0 s^{-1}
	$\diamond$	1.0 $\pm$1.0 s^{-1}	1.0 $\pm$1.0 s^{-1}	1.0 $\pm$1.0 s^{-1}
$T_{2,f}$	$*$	54.4 $\pm$1.3 ms	31.8 $\pm$0.9 ms	16.7 $\pm$0.3 ms
	$\diamond$	54.2 $\pm$1.3 ms	31.5 $\pm$0.9 ms	16.5 $\pm$0.3 ms
$T_{2,r}$	$*$	13.8 $\pm$1.2 μs	13.7 $\pm$0.8 μs	13.6 $\pm$0.5 μs
	$\diamond$	14.4 $\pm$0.9 μs	14.6 $\pm$0.6 μs	14.5 $\pm$0.4 μs
T_D	$*$	0.3 $\pm$0.5 ms	0.5 $\pm$0.4 ms	0.6 $\pm$0.3 ms
	$\diamond$			

$*$ signal equation with dipolar terms

$\diamond$ signal equation without dipolar terms

Figure 3.3, parameter estimates are graphed for each experiment type and each gel using the MTSPGR signal equation including dipole terms. While these parameter estimates are generally in agreement with those derived from a simultaneous fit to all experiment types,

it should be noted that k_f and T_D are not well constrained for these fits, particularly for 2% agar. In addition, there is some disagreement among estimates of F that are matched by a reciprocal trend in the estimates of $T_{2,f}$. An independent measurement of $T_{2,f}$ using the multi-echo T_2 sequence gave a T_2 of 70.1 ± 0.1 ms, 38.5 ± 0.2 ms, and 18.3 ± 3 ms for 2%, 4%, and 8% agar respectively.

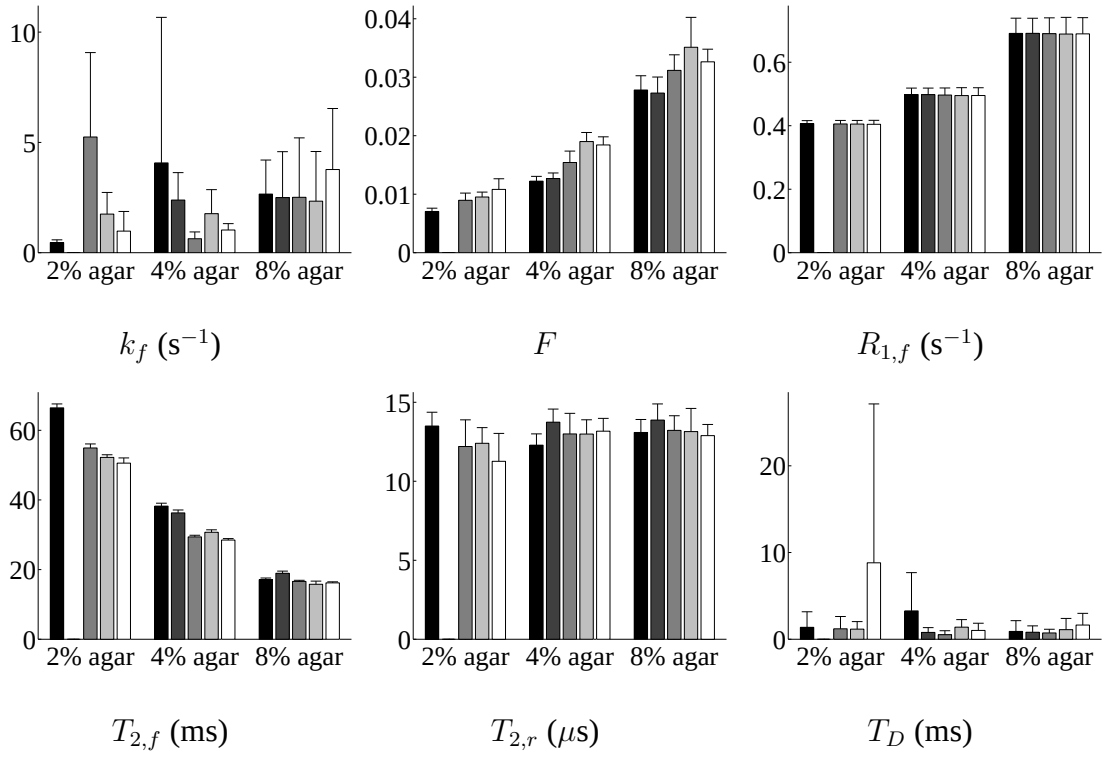

Figure 3.3: Comparison of parameter estimates for various experimental designs. The five bars for each gel correspond to experiment types I through V. Error bars form a 95% confidence interval. Type II experimental data for 2% agar is not available and intentionally left blank.

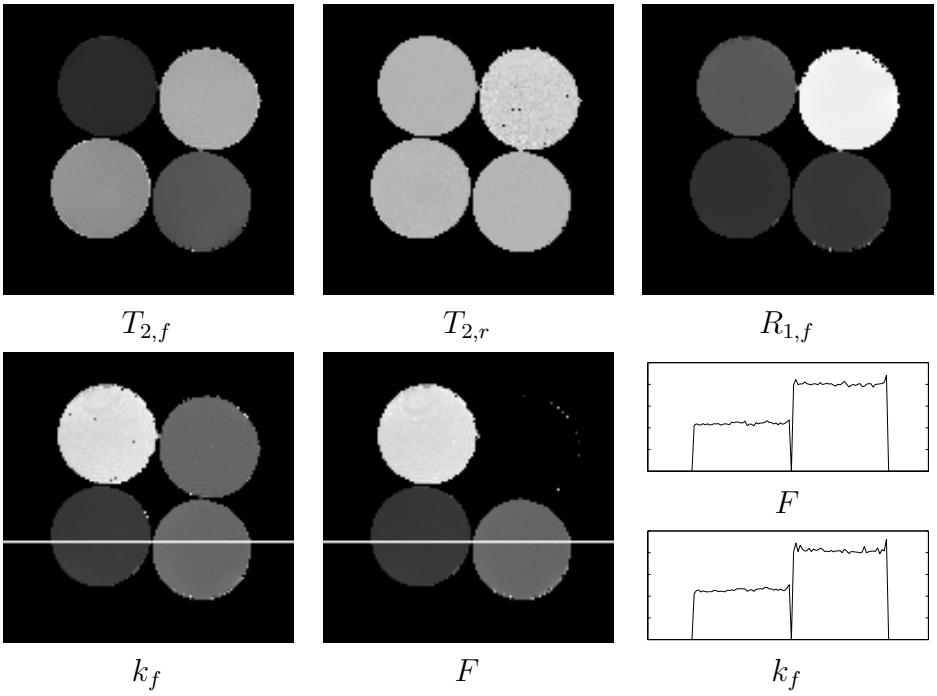

Figure 3.4: Parameter images based on a simultaneous fit of type IV and type V experiments using the RP variant of the MTSPGR signal equation neglecting dipole interaction. The materials shown, moving clockwise from the top-left, are 8% agar, $MnCl_2$ solution, 4% agar, and 2% agar. Also, shown are profiles across the F and k_f parameter maps.

3.2.3 Parameter images

For the imaging data both the accuracy of the estimates, as compared to the non-imaging studies, as well as the precision of the estimates, as reflected by the within image variation, were considered. The estimates were computed using both variants of the model by simultaneously fitting the type IV and type V data as well as by fitting the type V alone. Parameter images derived from the simultaneous fit of the model without dipole terms are shown in Figure 3.4. Also shown are intensity profiles taken along a line in the F and k_f images. These images show good uniformity, as a result of compensation for excitation field and reception sensitivity variations, as well as good SNR.

The precision of these estimates was evaluated by computing the standard deviation within regions of interest corresponding to the four bottles. These regions were defined by thresholding the image and eroding the resulting mask by one voxel. The mean and standard deviation for each bottle and each parameter are given in Table 3.4 for the simultaneous fits. The results of fitting to the type V experimental data alone proved highly unstable and are not shown.

Comparing the parameter estimates for the two variants of the model shows that the two are largely in agreement with subtle differences following the same trend as for the non-imaging experiments. However, variability in the estimates of k_f for the model including dipole interaction is significantly higher than that without. In addition, the variations in T_D suggest that it is not well constrained by this experimental design. Comparing the parameter estimates with those of the non-imaging experiments shows that the estimates of F are consistently lower and the estimates of k_f are consistently higher for the imaging experiments.

3.3 Discussion

The goal of this work was to demonstrate the feasibility of using pulsed MT-weighted MRI sequences to rapidly produce quantitative images of the exchange and relaxation properties within an object. To describe these properties the binary spin bath model was employed with a Gaussian lineshape. While this model well characterizes the gels used in these studies, there are a number of consideration in generalizing this technique to in vivo studies. A number of authors have described alternate lineshapes that are more suitable for tissue [69, 80, 97]. Also, there is some evidence that tissues such as white matter are better characterized by a model with two free water (long T_2) components [63, 142, 85]. While

Table 3.4: Parameter estimates for agar gels averaged over each region of the parameter maps.

		$MnCl_2$	2% agar	4% agar	8% agar
k_f	$*$		$0.842 \pm 0.2\,s^{-1}$	$1.37 \pm 0.3\,s^{-1}$	$2.47 \pm 1\,s^{-1}$
	$\diamond$		$0.734 \pm 0.05\,s^{-1}$	$1.32 \pm 0.2\,s^{-1}$	$2.78 \pm 0.3\,s^{-1}$
F	$*$	0	0.0074 ± 0.0016	0.0121 ± 0.001	0.0271 ± 0.004
	$\diamond$	0	0.0066 ± 0.0004	0.0121 ± 0.002	0.0260 ± 0.002
$R_{1,f}$	$*$	$2.07 \pm 0.05\,s^{-1}$	$0.419 \pm 0.002\,s^{-1}$	$0.483 \pm 0.1\,s^{-1}$	$0.760 \pm 0.04\,s^{-1}$
	$\diamond$	$2.07 \pm 0.05\,s^{-1}$	$0.419 \pm 0.02\,s^{-1}$	$0.483 \pm 0.1\,s^{-1}$	$0.760 \pm 0.04\,s^{-1}$
$R_{1,r}$	$*$		$1.0 \pm 1.0\,s^{-1}$	$1.0 \pm 1.0\,s^{-1}$	$1.0 \pm 1.0\,s^{-1}$
	$\diamond$		$1.0 \pm 1.0\,s^{-1}$	$1.0 \pm 1.0\,s^{-1}$	$1.0 \pm 1.0\,s^{-1}$
$T_{2,f}$	$*$	66.8 ± 3 ms	57.3 ± 3 ms	33.8 ± 3 ms	16.8 ± 1 ms
	$\diamond$	66.8 ± 3 ms	56.4 ± 3 ms	33.7 ± 2 ms	16.8 ± 0.9 ms
$T_{2,r}$	$*$		$13.1 \pm 2\,\mu$s	$14.1 \pm 0.6\,\mu$s	$14.1 \pm 1\,\mu$s
	$\diamond$		$14.3 \pm 0.5\,\mu$s	$14.1 \pm 0.3\,\mu$s	$14.1 \pm 0.3\,\mu$s
T_D	$*$		1.32 ± 3 ms	0.02 ± 0.5 ms	0.14 ± 1 ms
	$\diamond$				

$*$ signal equation with dipolar terms

$\diamond$ signal equation without dipolar terms

changing the lineshape is straight forward it is not clear whether adding additional compartments to the model will be beneficial. The situation may prove to be similar to the results presented here for adding dipolar terms to the model, in which improvements in accuracy are offset by a loss of precision through greater sensitivity to noise. For completeness, the

binary spin bath model should also allow for exchange of transverse magnetization [164]. However, it was found that in ODE simulations of these experiments this effect is negligible.

In implementing the MTSPGR signal equation, both a continuous-wave (CW) and rectangular pulse (RP) approximation for the restricted pool was considered. While the CW approximation was satisfactory for experiments in which the duty cycle of pulsation was large, it proved inadequate at small duty cycles. This is because the time constant for equilibration of the two pools is on the order of a few milliseconds, comparable with the duration of the MT pulses. The RP approximation, by taking into account the duty cycle and pulsation frequency, offers extra freedom in designing experiments, which can be used to advantage in improving estimates of the exchange constant k_f. In particular, it was found that for imaging studies, including experimental data from two different pulse sequences improved the estimates of k_f beyond what could be expected from an equivalent increase in SNR. This result is consistent with findings of [123] in which greater precision was obtained in an MT NMR experiment in which CW and pulsed experimental data were used together.

In choosing a signal equation, it was necessary to establish whether including dipolar terms in the model improved the parameter estimates. The results of the non-imaging studies show that the dipolar terms make a statistically significant improvement in the fit of the model and that neglecting the dipolar terms results in a modest underestimate of the pool size fraction F. However, it was also found that neglecting the dipolar terms substantially improved the precision of the estimates of k_f in the imaging experiments. Hence, there is a tradeoff between accuracy and precision when including the dipolar terms in the model which favours neglecting them. One can not generalize this conclusion to other materials, however, since the uncertainty in k_f tends to decrease as F increases and k_f decreases.

There are a number of factors to consider in designing an experiment. In particular, one needs to select the range of offset frequencies, average irradiation powers, and pulse repetition periods to measure. While not all of these factors were considered in detail, a number of trends were noted. With respect to pulses powers, little benefit was found in choosing more than two pulse powers for an experiment beyond that which can be expected from an equivalent number of repeated measurements. For this reason, in the imaging experiments the number of pulse angles was reduced from three to two. With respect to frequency offsets, there is clearly little benefit in sampling offsets so close to resonance that the free pool is saturated or so far from resonance that the MT effect disappears. Intuitively, one would expect that offsets at which the MT effect or *bite* is largest to be the most useful (2 kHz through 20 kHz for the agar gels considered here); however, taking advantage of this requires a priori knowledge of the linewidth. Since the duration of the pulses is comparable to the equilibration time for the two pools, the behaviour of a sequence depends on both the pulse duration and interpulse interval for a given average power. It was found that sampling more than one of these combinations substantially improved the estimates of k_f.

Besides optimizing the sampling, a variety of fast imaging techniques could be employed to speed up the data acquisition. The MTSPGR sequence with $TR = 50\,\text{ms}$, 128 phase encodes, 8 signal averages, and 12.8 s of preparation takes 64 s per sample image. This sequence easily generalizes to 3D by exchanging signal averages for phase encode steps in the slice direction with little increase in total scan time. Alternately, one can use an MTP type sequence and collect an image in a single shot, or a few shots, following preparatory pulsing. Similar modification can be made to reduce the imaging time required to collect B_0, B_1, and R_1^{obs} data. Given these fast imaging modifications to the pulse sequences, single slice imaging would be feasible within a clinically acceptable scan time of perhaps 30 minutes and likely multislice imaging would be as well.

While the results of these experiments were generally in agreement with those reported in [64] (see Table 3.1), the discrepancies exceed the quoted uncertainties. In particular, R_1^{obs} differs significantly between the two sets of experiments. Since this parameter is determined in a separate inversion recovery experiment and influences the subsequent estimate of the other parameters, the differences between the results may be due to this factor alone. Given that there may also be differences between gel preparations, the consistency of results between the different experiments performed on the same gel is likely a better measure of experimental accuracy.

The results of the imaging experiments were generally in agreement with the results of the non-imaging experiments; however, systematic differences were noted in the estimates of F and k_f. In general, it was found that the uncertainty in F and k_f was correlated such that underestimates of F were matched by overestimates of k_f. A similar correlation was observed between F and $T_{2,f}$. As seen from the parameter estimates for the individual experiment types in Figure 3.3, each experiment has a different bias in this respect. This bias can likely be attributed to subtle differences between the approximations in the signal equation and the putatively correct ODE solution. Since these differences are smallest for pulsation that resembles continuous-wave irradiation one might expect that pulse sequences with frequent pulses to be more accurate. However, since it was found that the k_f parameter is not well constrained by this kind of experiment alone, such a solution is unsatisfactory. In practice, one may prefer a design with some inherent bias to gain greater precision in repeated measurements.

In summary, a method has been described for analyzing general pulsed MT experiments in which the magnetization is driven to steady state. From experiments on agar gel, it was shown that this method can be used to reliably and accurately estimate the exchange and relaxation properties of a material in an imaging context. Such an approach offers

advantages over imaging techniques yielding magnetization transfer contrast ratios (MTR) both from the perspective of providing more information and for being comparable among different pulse sequences and scanning hardware. While minor changes in the model are needed to account for the differences between agar gel and tissue, these results indicate that it is feasible to use this technique in vivo.

3.4 Derivation of the MTSPGR signal equation

In this section, details are given on how to derive the steady-state signal equation for MT-weighted spoiled pulsed imaging (MTSPGR) sequence. The solutions for the steady-state magnetization is computed as follows. Equations (3.1)–(3.5) can be written in matrix form as

$$\frac{\mathbf{M}(t)}{dt} = \mathbf{A}(t)\mathbf{M}(t) + \mathbf{B}\mathbf{M}_0 \tag{3.12}$$

where $\mathbf{M}$ is a magnetization vector, $\mathbf{M}_0$ is the fully relaxed state of the magnetization, and $\mathbf{A}$ and $\mathbf{B}$ are matrices corresponding to the coefficients of equations (3.1)–(3.5). Approximating a pulse sequence as a series of periods of free precession (fp), continuous-wave irradiation (cw) of the restricted pool, or instantaneous saturation (is) of the free pool, the matrix $\mathbf{A}$ is constant for each of these periods. Since the transverse magnetization of the free pool is decoupled from the other components in each of these cases, only the longitudinal components are used for computation and the transverse components are assumed to disappear through relaxation and spoiling. The state of the magnetization after a period τ for each of these cases is notated $F_*(M, \tau)$ and given by

$$F_{fp}(\mathbf{M}, \tau) = e^{-\mathbf{A}_{fp}\tau}\mathbf{M} + [\mathbf{I} - e^{-\mathbf{A}_{fp}\tau}]\mathbf{M}_0 \tag{3.13}$$

$$F_{cw}(\mathbf{M}, \tau) = e^{-\mathbf{A}_{cw}\tau}\mathbf{M} + [\mathbf{I} - e^{-\mathbf{A}_{cw}\tau}]\mathbf{M}_{cw}^{ss} \tag{3.14}$$

$$F_{is}(\mathbf{M}) = \mathbf{S}\mathbf{M}\ . \tag{3.15}$$

$\mathbf{S}$ is a diagonal matrix with elements $[\ S_f \quad 1 \quad 1\ ]$ where S_f is the fractional saturation of the free pool due to the given pulse. S_f is computed by solving for the magnetization of the free pool following the given pulse using equations (3.1)–(3.3) with $R_{1,f}$, k_f, and k_r equal to zero and the initial condition $\mathbf{M} = \mathbf{M}_0$. The ratio of $M_{z,f}$ before and after the pulse is S_f.

$\mathbf{M}_{cw}^{ss}$ is the steady state of the magnetization established after a long period of continuous-wave irradiation of the restricted pool.

$$\mathbf{M}_{cw}^{ss} = \begin{bmatrix} \dfrac{M_{0,f}(R_{1,r}k_f + R_{1,r}R_{1,f} + R_{1,f}k_r + WR_{1,f})}{R_{1,r}R_{1,f} + R_{1,r}k_f + R_{1,f}k_r + WR_{1,f} + Wk_f} \\ \\ \dfrac{M_{0,r}(R_{1,r}R_{1,f} + R_{1,r}k_f + R_{1,f}k_r)}{R_{1,r}R_{1,f} + R_{1,r}k_f + R_{1,f}k_r + WR_{1,f} + Wk_f} \end{bmatrix} \tag{3.16}$$

Using these equations one can solve for the steady-state magnetization of a periodic pulse sequence using the relation

$$\mathbf{M}(t + TR) = \mathbf{M}(t). \tag{3.17}$$

For example, a period from a simplified version of the MTSPGR sequence could be described in three steps: instantaneous saturation of the free pool due to the MT pulse, instantaneous saturation of the free pool by the excitation pulse, and a period of continuous-wave irradiation of the restricted pool of duration TR. Combining these yields the equation

$$\mathbf{M} = F_{cw}(\mathbf{S}_2\mathbf{S}_1\mathbf{M}, TR). \tag{3.18}$$

where $\mathbf{S}_1$ and $\mathbf{S}_2$ are fractional saturation matrices due to the MT and excitation pulses respectively.

The observed magnetization $M_{xy,f}$ is given by

$$M_{xy,f} = cS_{1,f}M_{z,f}^{ss}\sin\theta \tag{3.19}$$

where θ is the flip angle of the excitation pulse and c is a constant reflecting other factors such as proton density and equipment sensitivity. Solving equations (3.18) and substituting the result into (3.19) yields for the case of ($T_D \rightarrow 0$) after some simplification

$$M_{xy,f} = \frac{c(E_1 - 1)(E_2 - 1)(\lambda_2 - \lambda_1)S_{1,f}M_{z,f}^{ss}\sin\theta}{(E_1 - 1)(S_f E_2 - 1)(\lambda_2 - \lambda_1) + (S_f - 1)(E_2 - E_1)(\lambda_2 - R_{1,f} - k_f)} \quad (3.20)$$

where $\lambda_{1,2}$ are the eigenvalues of $\mathbf{A}_{cw}$ given by

$$\lambda_{1,2} = \frac{1}{2}(R_{1,f} + k_f + R_{1,r} + k_r + W) \pm \frac{1}{2}\sqrt{(R_{1,f} + k_f + R_{1,r} + k_r + W)^2 - 4(R_{1,f}R_{1,r} + k_f R_{1,r} + R_{1,f}k_r + R_{1,f}W + k_f W)}$$

with $E_1 = e^{-\lambda_1 t}$ and $E_2 = e^{-\lambda_2 t}$.

For the RP variant of the MTSPGR signal equation the approximate pulse sequence has the following steps: instantaneous saturation of the free pool from the MT and excitation pulse, continuous-wave irradiation of the restricted pool for a period $\tau/2$, a period $TR - \tau$ of free precession, and finally another period of continuous-wave irradiation of duration $\tau/2$. Combining all of these steps and solving for $\mathbf{M}$ as before yields an expression for the steady-state magnetization that is, while cumbersome to write out in full, straightforward to compute.

Chapter 4

Field variations and quantitative imaging

INTENSITY non-uniformity is the smooth intensity variation often seen in MR images caused by such factors as RF excitation field inhomogeneity [93], non-uniform reception coil sensitivity, poor slab selection profiles in 3D acquisitions, as well as electrodynamic interactions with the object often described as RF penetration and standing wave effects [15]. In modern MRI scanners these variations are often subtle enough that they are difficult to detect by visual inspection; however, the accuracy of quantitative measurements is affected. This is particularly true of T_2 measurements, in which bias accumulates with each echo, and of MT measurements, where the rate of saturation is proportional to the square of the RF field strength.

Initial efforts at correcting intensity non-uniformity were based on physical models or external measurements of the field variations [93, 26]; however, these methods are not sufficiently accurate to improve upon modern volumetric scans, such as those produced of the brain using a birdcage coil. Instead, recent efforts have focused on data driven strategies [28, 95, 157, 139] based on statistical definitions of image uniformity. However, statistical methods are unable to distinguish between intensity non-uniformity and true anatomical variation that may resemble the artifact. Moreover, these statistical approach-

es at best yield the true image to within a multiplicative scale factor and hence are not compatible with quantitative measurements.

In order to compensate for this artifact one needs to consider the mechanisms by which it arises. For example, slab selection profile effects can often be eliminated in quantitative measurements by careful pulse sequence design. In contrast, excitation field variations affect most kinds of quantitative measurement and can seldom be eliminated by careful design. Means of compensating for these variation are described in subsequent chapters. However before proceeding, an investigation into the mechanisms and manifestations of these variations is presented. A more mathematical treatment of this subject is given in Appendix A.

4.1 Theory of field variations and imaging

In this section, a physical model of intensity non-uniformity that has sufficient accuracy to predict the variations in a 1.5 T scanner using circularly polarized coils is developed and validated for a simple geometry. While this geometry is too simple to accurately predict the variations in individual anatomical scans, it is sufficient to investigate a number of observations and hypotheses: (i) the widely made assumption that the data is corrupted by a smooth multiplicative field is accurate for images without a T_1 weighting; (ii) the pattern of intensity variation is highly dependent on the shape of the object being scanned; and (iii) elliptically shaped objects produce a diagonal pattern of variation when scanned using circularly polarized coils.

4.1.1 Methods

Modeling the RF excitation field and reception sensitivity

For simplicity, an analytic approach is used to investigate the effect of eccentric geometry on intensity non-uniformity. This treatment considers a long homogeneous dielectric cylinder with elliptic cross section excited by a circularly polarized field perpendicular to the cylinder axis. Interaction with the RF coil is neglected and far from the cylinder the excitation field (B_1) is assumed to be uniform. The propagation of electric and magnetic fields in dielectric media is governed by the equations:

$$\nabla^2 \mathbf{E} = \mu\epsilon \frac{\partial^2 \mathbf{E}}{\partial t^2} + \frac{\mu}{\rho}\frac{\partial \mathbf{E}}{\partial t} \tag{4.1}$$

$$\nabla \times \mathbf{E} = \frac{\partial \mathbf{B}}{\partial t}\,, \tag{4.2}$$

where $\mathbf{E}$ and $\mathbf{B}$ are the electric and magnetic fields respectively, μ is the magnetic permeability, ϵ is the permittivity, and ρ is the resistivity of the media. The magnetic field B_1 is assumed to be oriented perpendicular to the cylinder axis while the electric field is oriented parallel. In addition, the solutions for the real vector fields $\mathbf{E}$ and $\mathbf{B}$ are assumed to vary sinusoidally in time at an angular frequency ω such that

$$\mathbf{E} = \mathsf{Re}\left\{E_z \hat{z} e^{j\omega t}\right\} \tag{4.3}$$

$$\mathbf{B} = \mathsf{Re}\left\{(B_x \hat{x} - jB_y \hat{y}) e^{j\omega t}\right\}\,. \tag{4.4}$$

Solutions to this problem for the cases of circular and elliptic cylinders are given in [47] and [135] (Appendix A) respectively.

A so-called circularly polarized excitation field is created by driving two orthogonal linearly polarized coils 90° out of phase such that the field components that contribute to the MR signal add constructively. In general, the field produced by a linearly polarized coil will vary in magnitude and direction within the object such that the combined field from

the two coils can have arbitrary elliptic polarization. This elliptically polarized field can be decomposed into a (+) rotating field, which causes the excitation, and a typically weaker (-) counter-rotating field that does not [150]. The orientation of this (+) rotating field with respect to the driving field can be interpreted as a phase shift, which is referred to here as a geometric phase shift.

In general, the individual field components will be complex to reflect the phase delays caused by currents induced in the object. Geometric and inductive phase shifts combine to determine the local phase of the excitation field within the object as follows:

$$\mathbf{B}^{+} = B_{xx} + jB_{yx} - jB_{xy} + B_{yy}\,. \tag{4.5}$$

where the notation B_{yx} refers to the magnetic field in the y direction produced by a coil aligned along the x axis. While this derivation is based on two linearly polarized coils aligned with the x and y axes, the result is general for any combination of coils producing a circularly polarized field. Hence, it can used to predict the field pattern of a birdcage coil or a pair of linearly polarized coils not aligned with the x and y axes.

The same solutions for the field components apply when orthogonal coils are used for reception. However, the geometric phase shifts caused by reception cancel with those of the excitation field [93] whereas the phase shifts due to induced currents accumulate. Hence, the reception sensitivity is given by

$$\mathbf{R}^{+} = R_0(B_{xx} - jB_{yx} + jB_{xy} + B_{yy})\,, \tag{4.6}$$

where R_0 is a scale factor reflecting the sensitivity of the coil.

Images produced by a spin echo sequence are simulated using the derived excitation field and reception sensitivity. The signal measured for a spin echo pulse sequence is given by [47]

$$S \;=\; \rho\mathbf{R}^{+}S_{SE} \tag{4.7}$$

$$S_{SE} \;=\; \sin^3\left(\frac{\pi}{2}\frac{|\mathbf{B}^+|}{B_m}\right)\exp(j\arg(\mathbf{B}^+))\,, \tag{4.8}$$

where ρ is the spin density, S_{SE} is the emitted signal, S is the measured signal, and B_m is the nominal field strength needed to produce a 90° flip-angle. This derivation neglects relaxation and assumes complete recovery of the magnetization between repetitions.

Phantom studies

To validate the theoretical model of intensity non-uniformity, two 40cm long plastic cylindrical containers were constructed with elliptic and circular cross sections respectively. The circular cylinder has an inside diameter of 17.5cm, while the elliptic cylinder has major and minor diameters of 20cm and 15cm. Each cylinder was filled with various concentrations of NaCl solutions made from deionized water.

The conductivity and permittivity of each solution was computed based on the concentration of NaCl using data from [101]. The quantities of NaCl were 1.38g/L, 2.83g/L, and 58.2g/L, or roughly 24mM, 48mM, and 100mM, producing resistivities of $4.0\Omega\mathrm{m}$, $2.0\Omega\mathrm{m}$, and $1.0\Omega\mathrm{m}$ respectively. These resistivities span the range typical of biological tissues [15] at frequencies around 64MHz. At this frequency, the relative permittivity of water is essentially unchanged from its D.C. value of $\epsilon_r = 80$, which is comparable to that of brain [133] at 64MHz. In addition to NaCl, a small quantity of $\mathrm{MnCl_2}$ was added to each solution to bring its concentration to $97\mu\mathrm{M}$ so as to reduce T_1 relaxation times to approximately 910ms. Experiments using long repetition times (TR = 30s) showed no measurable change in intensity non-uniformity after addition of $\mathrm{MnCl_2}$.

For the experiments, the cylinders were aligned axially with the isocentre of the body coil of a 1.5T Siemens Vision MRI scanner and scanned transversally using a B_1 field mapping sequence [151] as well as a standard spin echo sequence. All images were acquired at 2mm in-plane resolution and 6mm slice thickness. The spin echo sequence

($\mathrm{TR}/\mathrm{TE} = 8\mathrm{s}/14\mathrm{ms}$) had sufficiently short TE and long TR that relaxation can be neglected. The field mapping sequence is a stimulated echo technique ($90^\circ - \tau_e/2 - 90^\circ - \tau_1 - \alpha - \tau_2 - 90^\circ - \tau_e/2 - acquire$ where $\tau_e/\tau_1/\tau_2/TR = 36\mathrm{ms}/60\mathrm{ms}/8\mathrm{ms}/1\mathrm{s}$) which yields a series of images whose intensities are related by

$$S_i = a \cos b\alpha_i \,. \tag{4.9}$$

The parameters a and b are computed at each voxel by a non-linear least squares fit to the flip angles α_i and complex image values S_i. Images were acquired at $\alpha = 0^\circ,\ 40^\circ,\ \ldots,\ 400^\circ$. The resulting parameter map b is proportional to the excitation field strength, while the parameter map a is roughly proportional to spin density.

4.1.2 Results

Simulated spin echo images

Once the expressions for excitation field and reception sensitivity have been evaluated they can be used to simulate an imaging sequence. A simulated spin echo image for an elliptic geometry having $\mu = \mu_0$, $\epsilon_r = 80$, and $\rho = 2\,\Omega\mathrm{m}$ is shown in Figure 4.1. Also shown are the corresponding excitation field and reception sensitivity.

It should be noted that the pattern of non-uniformity in the spin echo image resembles neither the excitation field nor the reception sensitivity. This is caused by the apparent reversal of the excitation field to produce the sensitivity map. However, close inspection of the phase images for the two cases reveals that the excitation field and reception sensitivity maps differ by more than a reversal. In particular the geometric phase in the two cases is opposite while the inductive phase lag, dominant in this medium, remains unchanged.

Due to the symmetry of the elliptic shape, the magnitude of the excitation and reception sensitivity maps differ only by a reversal of the y axis. However, the resulting spin echo

image is not symmetric as reception sensitivity makes a stronger contribution to image non-uniformity than does excitation field variation.

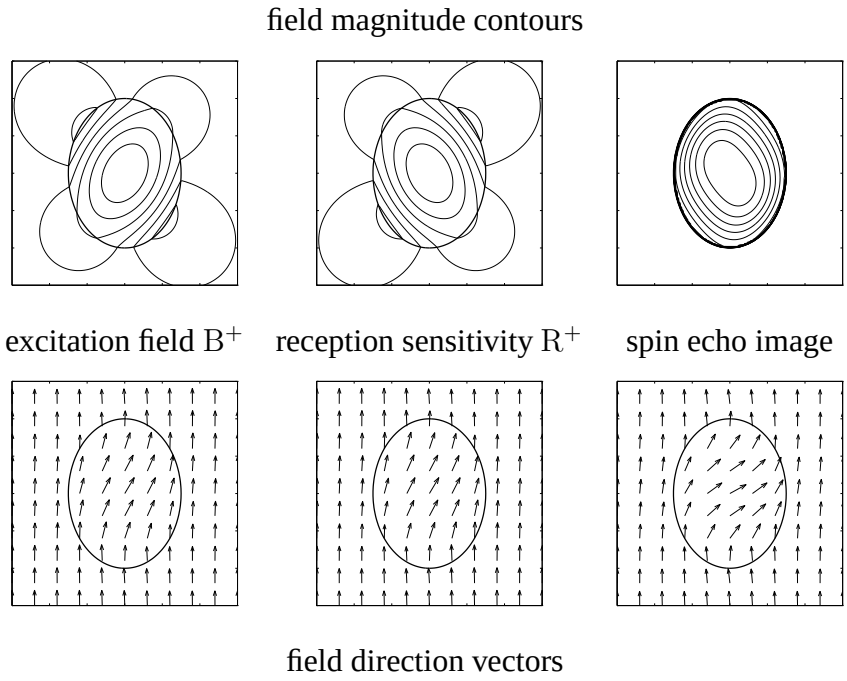

Figure 4.1: Simulated spin echo images with nominal 90° and 180° flip-angles. Contours are at 5% of mean intensity. For the spin echo image the direction vectors can be interpreted as the phase of the complex image.

Comparison with phantom studies

The experimental data admits two types of comparisons with the theoretical model: a direct comparison of the measured excitation field with that predicted, and a comparison of the measured spin echo image with that simulated from the predicted excitation field and reception sensitivity.

Before any comparisons were made all of the measured data was first automatically registered [24, 25] with the spin density map of the corresponding simulated image by linear transformation. A common mask was defined for each pair of images by automatically thresholding each image based on its histogram [104], taking the intersection of the two masks, and eroding it by 2mm. The RMS difference between two images was then computed within the common mask and expressed as a percentage of the mean intensity in the simulated image.

Figure 4.2 shows the excitation fields measured in the elliptic cylinder for each of the three NaCl solutions. Also shown are the predicted field patterns and the differences between the measured and predicted results. The prediction of a diagonal pattern of non-uniformity is confirmed by these experiments. When the gray scale of the difference image is expanded, it reveals minor and largely random differences between the measured and predicted images. The accuracy of the results for the circular cylinder is essentially the same.

The accuracy of the model at predicting the measured images was quantified by computing the root-mean-square (RMS) difference between the two. In all cases, the RMS difference was less than 2% and did not increase as the severity of the non-uniformity increased.

Figure 4.3 shows the measured and predicted spin echo images for the two geometries and three solutions. The pattern of variations in these images is more complicated and the variations are more severe owing to the contribution of the reception sensitivity. Note that the orientation of the diagonal pattern in the elliptic case is reversed with respect to the excitation field map. The RMS difference between measured and predicted images was 1%-2%.

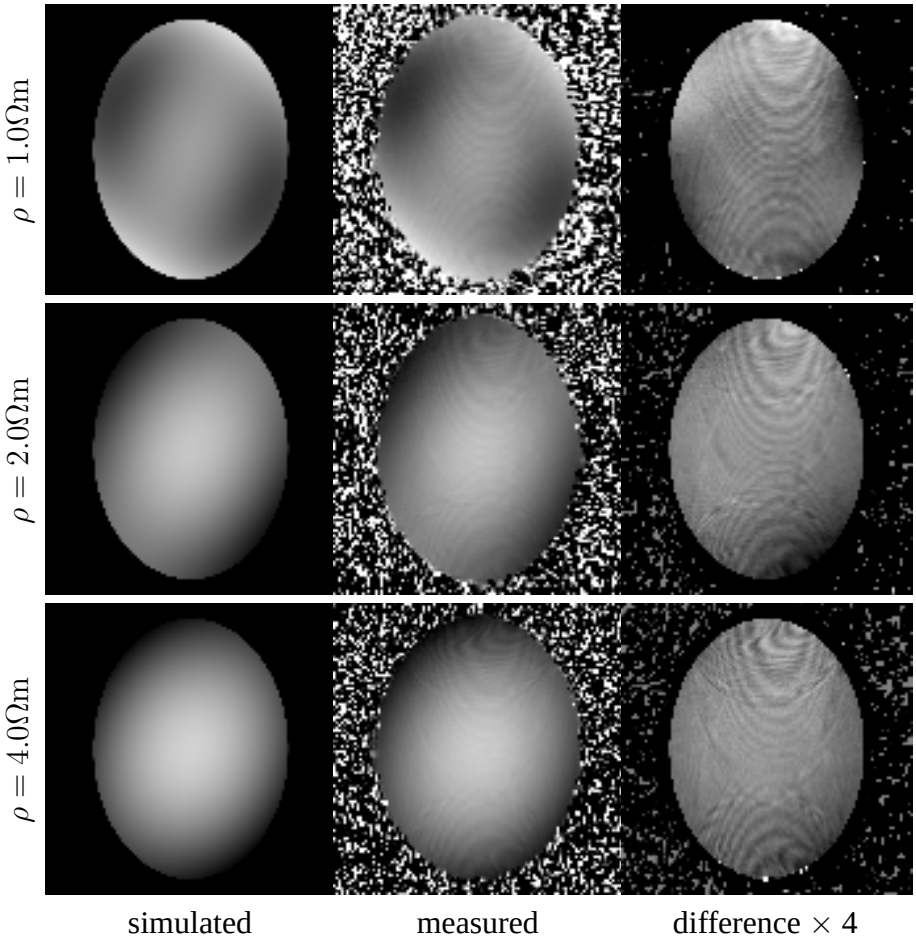

Figure 4.2: Comparison of predicted and measured excitation fields B^+ in an elliptic phantom for three levels of resistivity. The normalized intensity scale for each image is 0.8 to 1.2 except for the difference images which are -0.05 to 0.05.

4.1.3 Discussion

By modeling the electromagnetic interactions with the subject during excitation and reception from first principles, one can account for almost all of the intensity non-uniformity observed in volumetric scans at 1.5 T. This agreement is achieved in spite of making no explicit assumptions of a coil producing the fields. While this is reasonable for a head sized object in a body coil, one can expect that smaller coils such as a head coil would produce

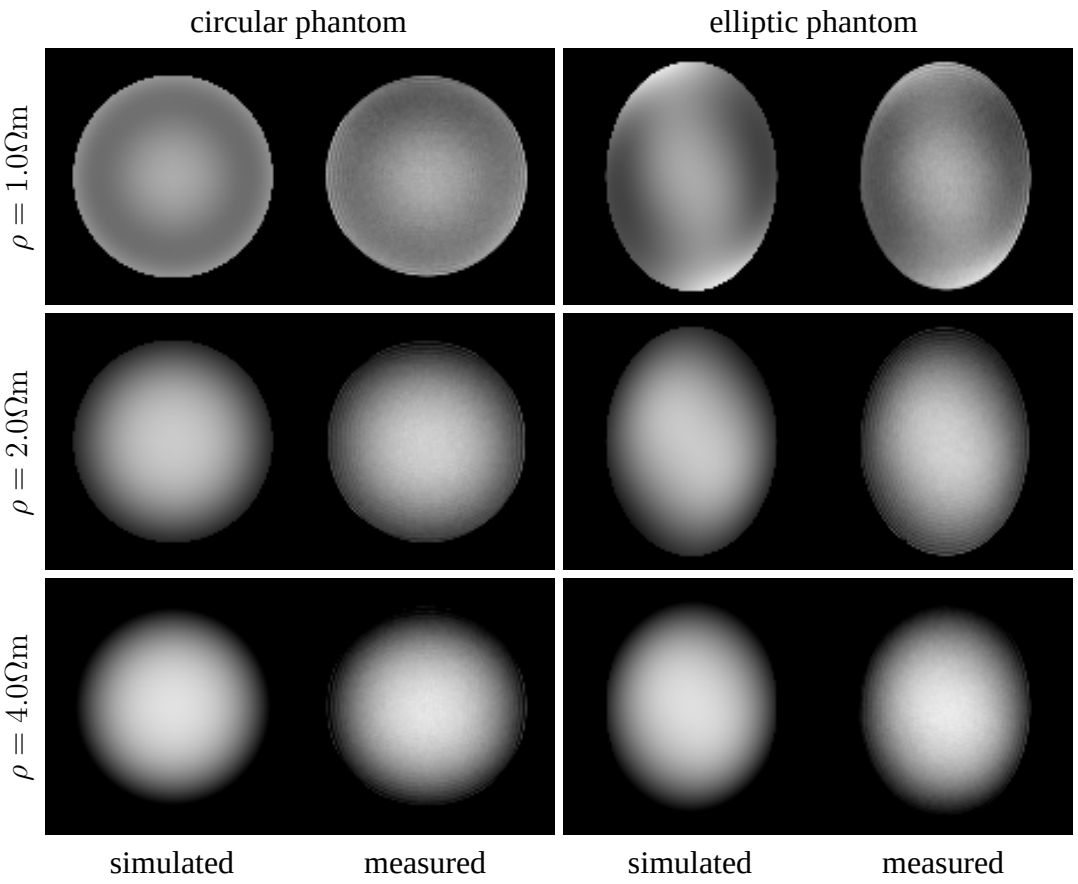

Figure 4.3: Comparison of predicted and measured spin echo images for each level of resistivity. The normalized intensity scale for each image is 0.8 to 1.2.

some variations caused by their interaction with the object. However, in either case electromagnetic interaction with the object is the primary cause of intensity non-uniformity. Hence, the use of equation (4.7) is justified, and verifies that non-uniformity is correctly modeled as a smooth multiplicative field for proton density imaging sequences. However, for other imaging sequences that depend on relaxation, the term S_{SE} in equation (4.7) will depend on the relaxation rates and will not in general be spatially smooth for inhomogeneous media.

It has been shown here that an elliptic geometry imaged using a circularly polarized coil

produces a diagonal intensity non-uniformity pattern qualitatively similar to the quadrapole artifact observed with a linearly polarized coil. Although, one would expect the circularly symmetric pattern seen for circular objects to generalize to an elliptically symmetric pattern for elliptic objects, in the elliptic case the two linear fields interact with the media differently, leading to asymmetric intensity variations that do not cancel in the combined field. Such asymmetry could be incorrectly attributed to right-left hemisphere differences in a sensitive statistical analysis based on neurological scans of a population. Furthermore, since the orientation of this diagonal pattern is determined by the orientation of the object and not the orientation of the coil, one can expect that non-uniformity patterns will, in general, be correlated with anatomy and hence will also be present in averages of multiple scans.

Inspection of the experimental results for the elliptic case would suggest that the reception sensitivity is the mirror image of the excitation field pattern. However, the theoretical results show a more subtle relationship. In particular, for conductive objects there is a distinction between the phase delays associated with induced currents and those inherent in imaging the object in the absence of conductivity. Accounting for excitation and reception, the latter phase terms cancel while the former do not, thereby leading to the non-uniformity pattern in the spin echo image being more complicated than either the excitation or receptions fields.

An important implication of this lack of cancellation is that for arbitrarily shaped conductive objects, measurement of the excitation field is not sufficient to predict the pattern of variations in the resulting image. In addition, since electrodynamic interaction significantly affects the reception sensitivity, neither measurement of the sensitivity in the absence of the subject nor scanning of a standard phantom is sufficient to predict the variations in a given subject. Furthermore, these variations will be present irrespective of the uniformity of the

field produced by the unloaded coil. As has been shown, the variation can be predicted by an electrodynamic model provided it takes into account the pulse sequence, geometry, and resistive and permittive properties of the subject.

4.2 Measuring field variations

Although the pattern of field variations has a complex dependence on the geometry of the object, the pattern of variations is stable for a given set of experiments with a fixed geometry. Hence, the artifact can be compensated for in quantitative studies by measuring the field variations as part of the study. This is true of both main magnetic field variations (B_0) and RF field variations (B_1). A method of measuring each of these is described in what follows. These measurements are incorporated into the analysis that is described in subsequent chapters.

4.2.1 Measuring the main magnetic field

B_0 maps were acquired using a standard shifted readout phase difference technique [134] employing a gradient echo readout ($TR = 53$ ms). This sequence is illustrated schematically in Figure 4.4. The two acquisitions are identical except that the timing of the readout is shifted by 4.48 ms while keeping the repetition period TR constant. A 4.48 ms shift was chosen based on a lipid resonance shift of 223 Hz at 1.5 T. This 223 Hz shift corresponds to a 2π phase shift which brings the lipids in phase with adjacent water in the image. In practice, the chemical shift of lipids may vary, thus biasing the field map in these regions. Another difficulty is that B_0 variations greater than 223 Hz require unwrapping of the resulting phase map. None of the studies presented in this thesis required phase unwrapping.

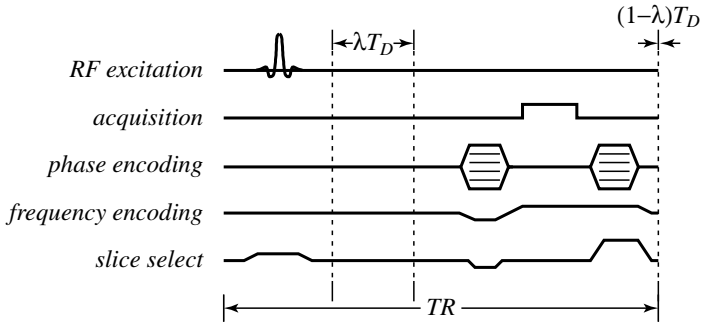

Figure 4.4: Pulse sequence schematic for B_0 measurements. Images are acquired with and without the delay T_D added to the echo time. The two sequences correspond to λ taking the value 0 or 1 while the repetition period TR remains constant.

The B_0 map is calculated as follows

$$B_0 = \frac{\arg I_2 - \arg I_1}{2\pi T_D} \tag{4.10}$$

where I_1 and I_2 are the complex image intensities and T_D is the echo shift (4.8 ms). The B_0 obtained by this calculation is the difference (in Hz) between the resonance frequency and the carrier frequency used to demodulate the measured signal, which is typically the same as the transmitter carrier frequency. Hence, B_0 maps will be shifted by a constant offset if the transmitter frequency changes between acquisitions. In addition, pulse sequences employing strong field gradients can create eddy currents in the magnet that may cause subtle shifts in the apparent field strength. In such situations a more precise field map can be obtained by modifying the sequence in question to have a shifted readout as is shown for the pulse sequence in Figure 4.4.

4.2.2 Measuring the RF field

Although a variety of B_1 field mapping sequences have been proposed [143, 151], a new scheme was implemented for this work based on a fast spin echo readout so as to provide an appropriate balance between acquisition time and image quality while avoiding the errors associated with slice selective pulses. This pulse sequence is shown schematically in Figure 4.5. It consists of a non-selective rectangular pulse followed after a period $\tau/2$ by a standard fast spin echo readout consisting of a slice selective $\pi/2$ pulse and a series of slice selective spin echo π pulses with spacing τ. The sequence is repeated with the flip angle of the rectangular pulse twice that in the first acquisition. Crusher gradients are chosen so as to only retain signal from the longitudinal component of the magnetization following the rectangular pulse. A map of the B_1 field is computed from the ratio of the two images where $y = I_2/I_1$ the ratio of the image intensities is related to the flip angle η_1 of the rectangular pulse for the first image by

$$\eta_1 = \cos^{-1}\left(\frac{y}{4} \pm \frac{1}{4}\sqrt{y^2+8}\right) . \tag{4.11}$$

Normalizing the computed η_1 by its nominal value yields a field map that can then be used to adjust the nominal pulse angles when analyzing the results of other sequences. Equation (4.11) can be modified to account for B_0 variations; however this factor was neglected since the resulting correction is small ($\sim 1\%$ for a frequency shift of 100 Hz). A nominal flip angle for η_1 of 33° was used throughout; the TR was 2 s, corresponding to a 2.5 minute scan for a 256×256 matrix.

While this approach allows one to rapidly acquire single slice B_1 field maps with a minimum of artifacts, it does not generalize well to multi-slice acquisitions. This is because T_1 recovery between the rectangular pulse and the $\pi/2$ excitation pulse biases the field estimate. In the case of single slice acquisitions this period is extremely short and can

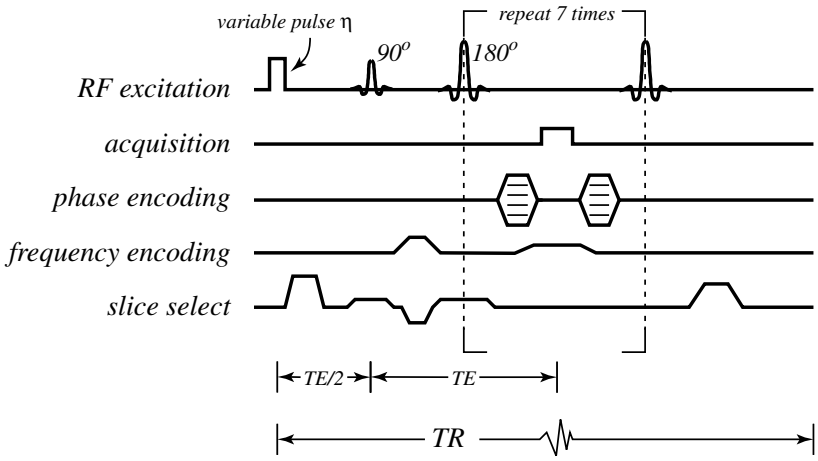

Figure 4.5: Pulse sequence schematic for B_1 measurements. The sequence is repeated twice with $\eta_1 = 33^\circ$ and $\eta_2 = 66^\circ$.

be ignored; however, if multiple slices are acquired in an interleaved fashion following a single rectangular pulse this delay can be significant. An alternative [151], that addresses this limitation is to use a stimulated echo sequence in place of the spin echo. Since the stimulated echo can be encoded with a field gradient, this encoding can be used to distinguish signal modulated by the field strength from the unmodulated signal due to T_1 recovery.

Chapter 5

Relaxometry of the free pool

ACCURATE measurements of the relaxation and exchange rates in a magnetization transfer experiment depend upon accurate measurements of the relaxation properties of the free water protons. Conventional T_2 relaxation measurements on a binary spin bath system yield the T_2 of the free pool ($T_{2,f}$) directly, whereas conventional relaxometry measurements of T_1 yield an apparent T_1, which is the longer of the two T_1 recovery rates exhibited by the system. While only one of T_1 and T_2 needs to be measured independently since the relaxation properties of the free pool can be partially determined from an MT experiment, measuring both allows one to assess the validity of the MT model. In the case of white matter, an independent T_2 measurement allows one to resolve a second, smaller, pool of free water protons that biases the estimates of $T_{2,f}$ derived from the MT data.

In this chapter, a method for measurement of the T_2 and the apparent T_1 ($T_{1,obs}$) of the free pool is described. While these relaxometry techniques are well established, the approach described here is novel for its use of B_1 and B_0 field maps to improve the accuracy of the measured relaxation times.

5.1 Quantitative T_2 measurements

The following manuscript appeared in Magnetic Resonance in Medicine, vol. 43, no. 4, pp. 589–593, April 2000.

Correction for B_1 and B_0 variations in quantitative T_2 measurements using MRI

JOHN G. SLED AND G. BRUCE PIKE

Abstract: A new method is described for compensating for the bias introduced by variations in radio-frequency (RF) field strength and main magnetic field strength when making quantitative T_2 measurements using MRI. Field measurements made during the MRI study are used in combination with a signal model for off-resonance and imperfect RF pulses to correct the estimated T_2 value at every voxel. Applicable to both multi-component and conventional single component T_2 studies, the method has been validated experimentally using paramagnetic salt solutions in a multi-compartment phantom. Studies of the human head are used to demonstrate the method in practice.

Keywords: T_2 relaxation, quantitative imaging, magnetic resonance imaging

5.1.1 Introduction

Quantitative T_2 measurements using MRI have the advantage, as compared to standard T_2-weighted scans, of being independent of the specifics of the acquisition parameters facilitating direct comparisons among populations [148] and longitudinal studies. Such techniques can also yield information about multiple T_2 components and provide greater pathological specificity in some applications [85, 160]. However, T_2 often varies subtly between tis-

sues such that systematic errors caused by B_1 and B_0 field inhomogeneity are an important concern. Flip angle errors and off-resonance pulses tend to result in underestimates of T_2 when using standard multi-echo quantitative techniques. This problem is aggravated by the tendency to use long trains of closely spaced echoes so as to be sensitive to a wide range of T_2 values when imaging heterogeneous media.

A number of authors have described techniques to reduce the effect of pulse imperfections, either through spoiling of unwanted echoes [34, 115] or by reducing the sensitivity of the inversion pulses to B_1 and B_0 variations [78]. These latter techniques usually forgo the use of slice selective inversion pulses so as to eliminate problems caused by incomplete inversion of spins at the edge of the slice profile. The most common inversion pulse for reducing the effect of B_1 variations is the 90x–180y–90x rectangular composite pulse. Composite pulses of arbitrary complexity can be created to reduce sensitivity to field variations; however, these higher order composite pulses tend to be long, increasing both the echo time and power deposition. While one might expect the accuracy of T_2 measurements to continue to improve as new MRI scanners with better field uniformity are produced, much of the field variation is due to electromagnetic interaction with the subject [135] and hence inherent to the measurement technique.

In this communication, we describe a refinement of the standard technique for quantitative T_2 imaging in which we correct for B_1 and B_0 field variations. This is accomplished by rapidly acquiring B_1 and B_0 field maps along with the T_2 relaxation measurements and using these maps to correct the estimates of T_2. This technique can be used in combination with other techniques such as spoiling and composite inversion pulses that reduce the effect of these variations.

Another technique has been described previously for correcting for B_1 and B_0 variations [86] in which a uniform phantom is used to map the attenuation of each echo. These

maps are then used to choose the starting conditions for an iterative numerical technique which estimates T_2, B_1 and B_0 at each voxel. However, since in combination with efficient spoiling, the dominant effect of B_1 and B_0 variations is to attenuate the echoes in a manner indistinguishable from T_2 decay, the estimates of B_1 and B_0 are poorly constrained for small field variations. We overcome this in our approach by measuring these fields directly during acquisition.

5.1.2 Methods

Theory

In a pair of papers, Majumdar et al. described the effect of B_1 and B_0 variations on quantitative T_2 measurements [87, 88] using multi-echo sequences. This approach is based on treating the ensemble of spins undergoing inversions as a system having $j = 1$ angular momentum [13, 149]. Using the notation M_{-1}, M_0, M_{+1} to denote the transverse defocusing, longitudinal, and transverse refocusing states respectively, matrices describing the rotation of a magnetization vector $\mathbf{M} = [\ M_{-1} \quad M_0 \quad M_{+1}\ ]^T$ about the y and z axes are given by

$$R_z(\varphi) = \begin{bmatrix} \mathrm{e}^{-\mathrm{i}\varphi} & 0 & 0 \\ 0 & 1 & 0 \\ 0 & 0 & \mathrm{e}^{\mathrm{i}\varphi} \end{bmatrix} \tag{5.1}$$

$$R_y(\beta) = \begin{bmatrix} \cos^2(\beta/2) & -\frac{1}{\sqrt{2}}\sin\beta & \sin^2(\beta/2) \\ \frac{1}{\sqrt{2}}\sin\beta & \cos\beta & -\frac{1}{\sqrt{2}}\sin\beta \\ \sin^2(\beta/2) & \frac{1}{\sqrt{2}}\sin\beta & \cos^2(\beta/2) \end{bmatrix} \tag{5.2}$$

where φ and β are the rotation angles in radians.

A conventional CPMG technique viewed from a reference frame rotating at the resonance frequency consists of a $\pi/2$ rotation about x followed by a series of $\pm\pi$ rotations

about y and results in only the -1 or $+1$ states being occupied. However, for arbitrary pulse angles a mixture of states is present at every step. The goal of the various spoiling strategies for T_2 measurements is to spatially dephase the components resulting from unwanted transitions. For this work we make the approximation that spoiling is efficient such that only the transitions between -1 and $+1$ states contribute to the measured signal. Under this approximation, a pulse angle error or resonance shift results in a fractional attenuation of the measured signal with every inversion. For example, an on-resonance inversion pulse of angle β corresponds to a rotation about the y axis which from equation (5.2) results in an attenuation of the signal by $\sin^2(\beta/2)$.

The signal measured at the nth echo of a multi-echo experiment, taking into account the attenuation due to the inversion, can be written as

$$S_n = S_0 \mathrm{e}^{-n\tau/T_2} f^n = S_0 \mathrm{e}^{-n\tau/T_2 + n \ln f} \tag{5.3}$$

where τ is the time between echoes, and f is the attenuation factor. An exponential fit to the measurements $\{S_n\}$ yields an apparent $T_{2,obs}$ related to the true T_2 by

$$T_2 = \left(\frac{1}{T_{2,obs}} + \frac{\ln f}{\tau} \right)^{-1} \tag{5.4}$$

By solving this equation for $T_{2,obs}$ and expanding the result as a series up to order $(1-f)^2$

$$T_{2,obs} = T_2 - \frac{T_2^2}{\tau}(1-f) + O(1-f)^2 \,, \tag{5.5}$$

it is apparent that since $f < 1$ and $(1-f)$ is small, T_2 will be underestimated as a result of the attenuation. This error becomes worse as $T_{2,obs}$ increases and echo time decreases. We compensate for this error by computing f based on measurements of B_1 and B_0 and using equation (5.4) to correct the observed T_2.

For on-resonance pulses, the attenuation due to composite rectangular pulses is straightforward to compute using combinations of rotations. The furthest off-diagonal elements

corresponding to the -1 to $+1$ transition of the resulting matrix is the attenuation fraction f.

In the case of off-resonance pulses, in a reference frame rotating at the carrier frequency of the pulse, one needs to account for an effective B_0 field experienced by the spins [88]. Suppose for a rectangular pulse of duration t and nominal flip angle α the spins rotate by an angle δ about an axis inclined at an angle ϕ from the direction of the main magnetic field, z in our coordinate system. Then δ and ϕ are given by

$$\delta = \sqrt{\alpha^2 + (2\pi\Delta t)^2} \tag{5.6}$$

$$\phi = \frac{\pi}{2} - \tan^{-1}\left(\frac{2\pi\Delta t}{\alpha}\right), \tag{5.7}$$

where Δ is the frequency offset in Hz. For a rotation δ about an arbitrary axis expressed in spherical coordinates with polar angle ϕ and azimuth φ, the corresponding rotation matrix can be expressed as series of y and z rotations

$$R(\delta, \varphi, \phi) = R_z(\varphi)R_y(\phi)R_z(\delta)R_y(-\phi)R_z(-\varphi)\,. \tag{5.8}$$

Using this expression to compute the attenuation factor for a hard inversion pulse with rotation matrix $R(\delta, \frac{\pi}{2}, \phi)$ yields

$$f = 2\cos\delta\cos^4(\phi/2) - 2\cos\delta\cos^2(\phi/2) + \frac{1}{2}\sin^2\phi\,. \tag{5.9}$$

The corresponding matrix for a 90x–180y–90x composite pulse

$$R(\delta/2, 0, \phi)R(\delta, \pi/2, \phi)R(\delta/2, 0, \phi) \tag{5.10}$$

yields an attenuation factor which is, while cumbersome to write out in full, easily computed numerically.

The effect of these computed attenuation factors on a typical experiment are illustrated in Figure 5.1. The plots show the observed T_2 as either the offset frequency of the pulse

or the pulse angle are varied. The calculations are for a 32 echo CPMG sequence with an 11 ms echo spacing and either 1 ms rectangular pulses or 2 ms composite rectangular pulses. The true T_2 is 120 ms. Frequency offsets of 50-100 Hz and B_1 variation of 10%–20% are typical for clinical imaging at 1.5 T.

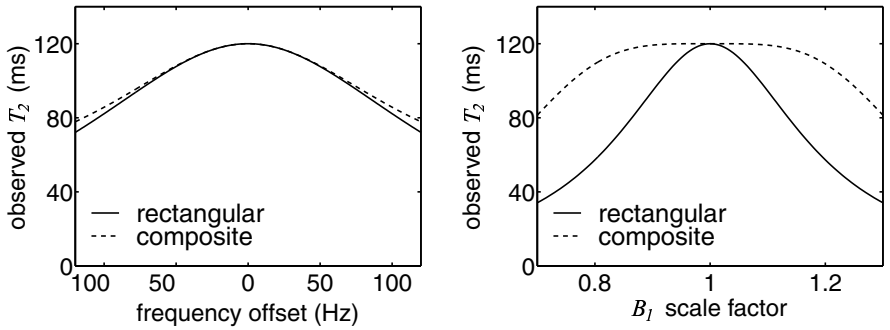

(a) (b)

Figure 5.1: Observed T_2 for a multi-echo experiment when the true T_2 is 120 ms and (a) the offset frequency is varied and (b) the pulse angle is varied. The solid and dashed lines are for rectangular and composite pulses respectively.

Experiments

To validate the method experimentally, we implemented a 32 echo CPMG sequence with crusher gradients for each inversion pulse alternating in sign and decreasing in magnitude [115], illustrated schematically in Figure 5.2. Two versions of the sequence were used, one with non-selective 1 ms rectangular pulses, the other with non-selective 2 ms composite pulses. An echo spacing of 11 ms and a repetition time of 2 s were used throughout.

Although a variety on B_1 field mapping sequences have been proposed [143, 151], we implemented a new scheme based on a fast spin-echo readout so as to provide an ap-

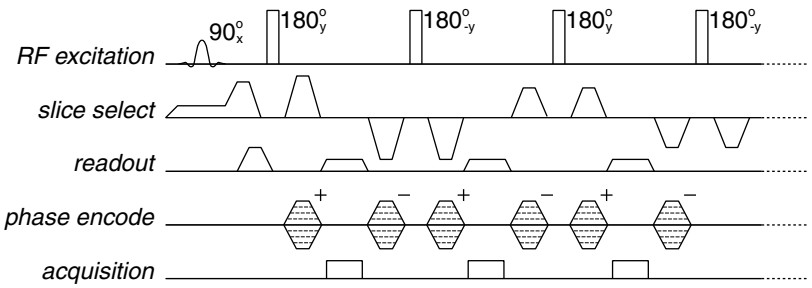

Figure 5.2: Sequence of RF excitation, gradient, and data acquisition steps for the quantitative T_2 sequence. The crushing gradients in the slice direction alternate in sign and decrease in magnitude with each echo.

propriate balance between acquisition time and image quality while avoiding the errors associated with slice selective pulses. The pulse sequence consisted of a non-selective rectangular pulse followed after a period $\tau/2$ by a standard fast spin-echo readout consisting of a slice selective $\pi/2$ pulse and a series of slice selective spin-echo π pulses with spacing τ. The sequence is repeated with the flip angle of the rectangular pulse twice that in the first acquisition. Crusher gradients are chosen so as to only retain signal from the longitudinal component of the magnetization following the rectangular pulse. A map of the B_1 field is computed from the ratio of the two images where $y = I_2/I_1$ the ratio of the image intensities is related to the flip angle η_1 of the rectangular pulse for the first image by

$$\eta_1 = \cos^{-1}\left(\frac{y}{4} \pm \frac{1}{4}\sqrt{y^2+8}\right) . \tag{5.11}$$

Normalizing the computed η_1 by its nominal value yields a field map that is used to scale the nominal inversion pulse angle α in equations (5.6) and (5.7). Equation (5.11) can be modified to account for B_0 variations; however this factor was neglected since the resulting correction is small ($\sim 1\%$ for a frequency shift of 100 Hz). A nominal flip angle for η_1 of 33° was used throughout; the TR was 2 s, corresponding to a 2.5 minute scan for a

256×256 matrix.

B_0 maps were acquired using a standard shifted readout phase difference technique [134] employing a gradient echo readout ($TR = 53$ ms). A readout shift of 4.48 ms between the two acquisitions was chosen based on a lipid resonance shift of 223 Hz at 1.5 T. As a result, resonance shifts greater than 223 Hz require unwrapping of the phase map. None of our studies required phase unwrapping. Both the B_1 and B_0 field maps were smoothed using a tensor cubic B spline approximation with 20 mm between knots.

To test the correction method, a cylindrical phantom with inside diameter 17.5 cm and 40 cm in length, having four inner compartments, was prepared with various concentrations of $MnCl_2$ solution. The one outer and four inner compartments were prepared to have T_2 relaxation times of roughly 120 ms, 30 ms, 60 ms, 90 ms, and 150 ms respectively, based on the empirically determined relation

$$\frac{1}{T_2} \approx (73\,\mathrm{s}^{-1}\mathrm{mM}^{-1}) \left[Mn^{++} \right] . \tag{5.12}$$

Also, each solution was prepared with a 48 mM concentration of NaCl so as to dampen its dielectric resonance. This concentration corresponds to a conductivity of $0.5\,\mathrm{m}^{-1}\Omega^{-1}$, a level typical for tissue [15, 135].

The cylinder was scanned using a standard circularly polarized head coil along a transverse slice at the isocentre of the magnet, and 40 mm from the centre of the coil. To demonstrate the application of the method, two additional scans were performed on normal volunteers. One was along a coronal slice angled perpendicular to the long axis of the hippocampus, 15 mm from the centre of the coil and magnet; the second was a sagittal slice 40 mm from the centre of the coil and magnet.

5.1.3 Results

The results of each T_2 experiment were analyzed using a non-linear least squares fit at each voxel of a simple exponential function with two degrees of freedom. The resulting T_2 maps were then corrected using equation (5.4) and the smoothed B_1 and B_0 maps acquired in the same session. The uncorrected and corrected parameter maps for the cylindrical phantom are shown in Figure 5.3. Also, shown are profiles taken along a line through each parameter map. As shown, the correction makes a substantial change in both the mean T_2 and overall uniformity. While the uniformity of parameter map is improved for both rectangular and composite pulses, the corrected parameter map for composite pulses is clearly superior. The resonance shift for this experiment varied by 40 Hz from the edge to the centre of the cylinder. The RF field strength varied from 0.91 to 1.2, with the maximum at the bottom right of the image.

The effect of correction was quantified for the cylindrical phantom by computing statistics on each of the five compartments. The mean and coefficient of variation were computed within each manually segmented region. The results are tabulated in order of decreasing concentration of [Mn^{++}] in Table 5.1. Note that the corrected rectangular pulse data was more uniform than the uncorrected composite pulse data, while the corrected composite pulse data was superior overall. Also, the expected trend of 30 ms, 60 ms, . . . 150 ms closely follows the mean T_2 values for the corrected composite pulse data.

The computed T_2 parameter maps before and after correction are shown for the brain studies using composite pulses in Figure 5.4. Also, shown are difference images with an expanded intensity scale to highlight the corrections. While the correction makes large changes to the T_2 values outside the brain, there are also smaller corrections within the brain of note. In particular, for the coronal slice the correction is 15–20 ms at the base of the temporal lobe on the right and 3–5 ms within the hippocampi. Also, for the shown

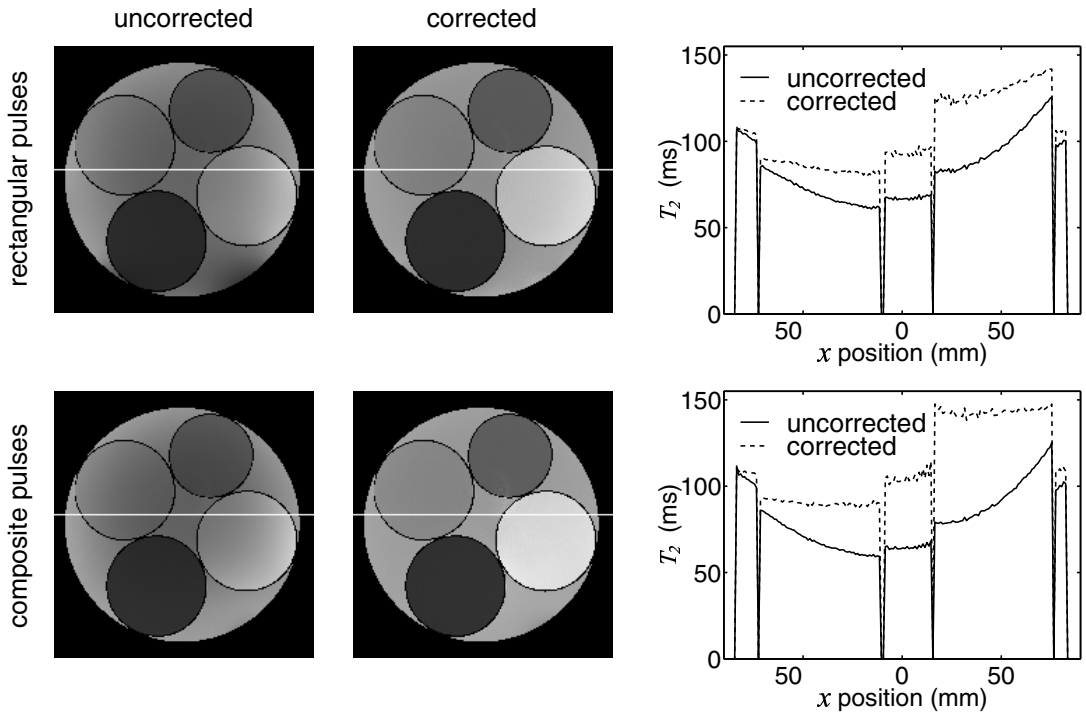

Figure 5.3: Quantitative T_2 images for the cylindrical phantom before and after correction. Also shown are intensity profiles along the white line for each case.

Table 5.1: Average T_2 for cylinder compartments before and after correction. The fourth row corresponds to the outer compartment.

rectangular pulses				composite pulses			
before		after		before		after	
T_2 (ms)	COV	T_2 (ms)	COV	T_2 (ms)	COV	T_2 (ms)	COV
27.5	3.4%	30.7	1.8%	30.2	4.6%	33.1	1.9%
50.6	4.4%	58.4	1.5%	51.2	6.5%	62.7	1.8%
72.0	9.7%	84.1	3.1%	71.3	11.9%	89.8	1.7%
81.1	19.0%	101.4	5.6%	91.3	13.6%	107.2	3.0%
97.8	12.2%	131.8	6.2%	99.1	14.5%	145.8	2.3%

sagittal slice, the correction is 10–15 ms at the base of the cerebellum and 5–10 ms along the dorsal surface of the brain. The range of field variations within the brain for these studies was about 100 Hz in B_0 and from 0.75 to 1.03 in B_1, with the greatest deviations near the ends of the coil.

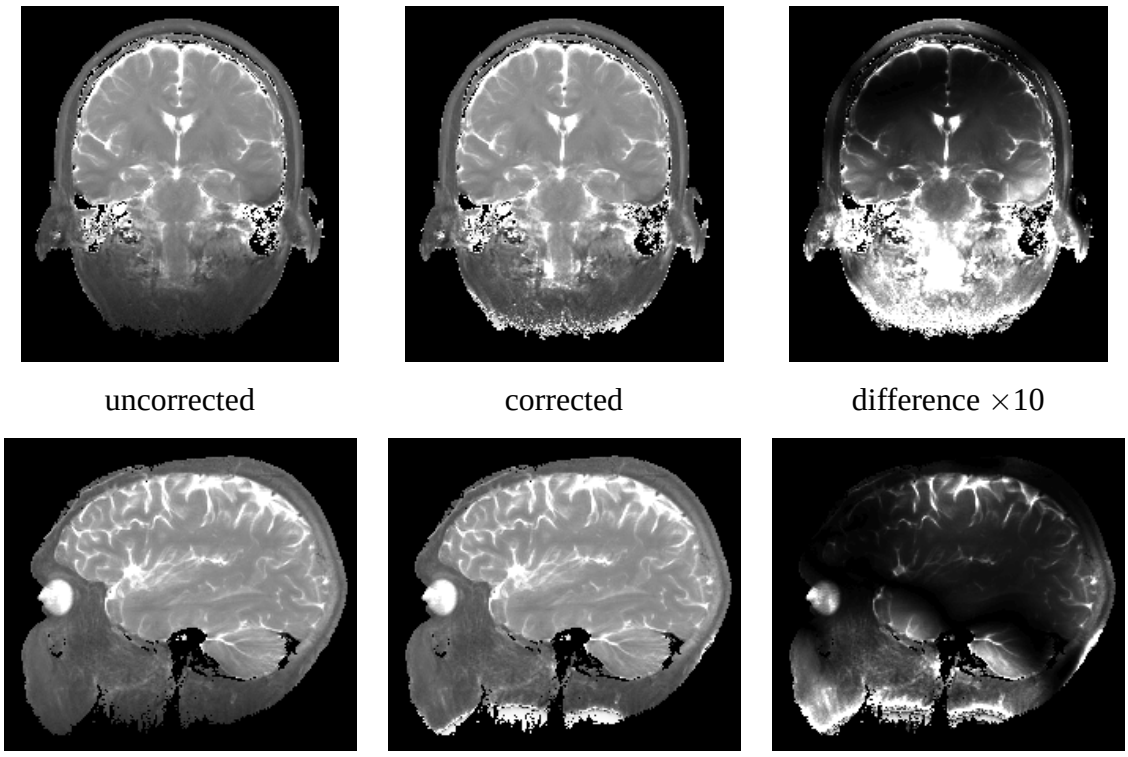

Figure 5.4: Quantitative T_2 images in brain before and after correction. The intensity scale is 0 to 200 ms for the T_2 images and 0 to 20 ms for the difference images.

5.1.4 Discussion and conclusion

We have described a refinement to the usual method of making quantitative T_2 measurements, in which the bias introduced by variations in the B_1 and B_0 field strength is com-

pensated for directly. While quantitative corrections tend to be subtle, they improve the accuracy and reproducibility of sensitive studies. Since the pattern of field variations depends both on the shape and composition of the subject and its position within the coil, the pattern of bias may vary significantly between subjects and with subsequent measurements, thus increasing the variability of uncompensated T_2 measurements.

Since the bias introduced by field variations decreases with increasing echo spacing, one can reduce its effect by increasing the echo spacing to be just short enough to observe the T_2 species of interest. However, maximizing the echo spacing may not be an option when scanning subjects having a number of tissues of interest and a range of T_2 relaxation times. This is also the case in tissues exhibiting multi-exponential behaviour where a short and long T_2 component are expected in the same voxel. The correction method described here can be used with multi-T_2 analysis techniques by correcting each T_2 component separately.

While our analysis has been derived for non-selective inversion pulses, the approach can be generalized to described the slice selective inversion pulses used in multi-slice protocols by integrating the contribution from each off-resonant element in the slice profile. However, unless the portion of the inversion pulse's slice profile which intersects with the slice profile of the excitation pulse remains flat as B_1 field strength varies, there will not be a simple mapping between true and observed T_2.

It is clear from the cylindrical phantom results that the correction method makes a substantial improvement in the uniformity and bias of T_2 measurements. However, some residual non-uniformity remained in the rectangular pulse data after correction. We attribute this to unwanted transitions not fully suppressed by the spoiling technique. These additional terms cause the echoes amplitudes to deviate from a simple exponential decay. Accounting for these terms for more than a few echoes is complex and depends on the details of the

spoiling strategy. While we found that even when neglecting these terms the corrected rectangular pulse data was more uniform and accurate than the uncorrected composite pulse data, it is clearly desirable to use this technique in combination with composite pulses.

In our studies on human subjects we found that the correction made a substantial difference throughout the brain when using rectangular pulses. For the composite pulse data only a few areas, where the field variations were strongest, were substantially changed. However, given that these field variations are generally difficult to predict, it is beneficial when making sensitive quantitative measurements to measure the fields and eliminate this unwanted source of variation.

5.2 Quantitative T_1 measurements

As part of the quantitative MT protocol described in the next chapter, an independent measurement of the apparent T_1 was used to constrain the relaxation and exchange parameters estimated from the MT data. Acquired using a standard Look-Locker multi-echo sequence [16, 169] with TE / TR = 12 ms / 2 s, this pulse sequence consisted of a non-selective composite 90x–180y–90x inversion pulse followed after a period TI_1 by $N = 4$ small angle slice selective excitation pulses. The data was analyzed using a two parameter least-squares fit yielding T_1 and a scaling parameter.

Using the notation of Brix et al. [16], the signal equation for the Look-Locker sequence is as follows. Take α and β to be the flip angles of the inversion and excitation pulses respectively. Defining $c_\beta = \cos\beta$, $E_2 = \exp(-\mathrm{TI}_2/T_1)$, and $F = (1 - E_2)/(1 - c_\beta E_2)$ the longitudinal magnetization before the nth excitation pulse ($1 \leq n \leq N$) is given by

$$M_n = M_{eq}[F + (c_\beta E_2)^{n-1}(Q - F)] \tag{5.13}$$

where Q is the quotient M_1/M_{eq} defined below, TI_2 is the interval between excitation

pulses, and M_{eq} is the equilibrium magnetization. The quotient is given by

$$Q = \frac{Fc_\alpha c_\beta E_r E_1[1-(c_\beta E_2)^{N-1}] + c_\alpha E_1(1-E_r) - E_1 + 1}{1 - c_\alpha c_\beta E_r E_1 (c_\beta E_2)^{N-1}} \tag{5.14}$$

where $c_\alpha = \cos\alpha$, $E_1 = \exp(-\mathrm{TI}_1/T_1)$, $E_r = exp(-t_r/T_1)$, and t_r is the interval between the last excitation pulse and the subsequent inversion pulse.

Since the measured signal is proportional to M_n, T_1 can be estimate by fitting equation (5.13) to the signal recovery curve at each voxel with M_{eq} as a free parameter. A difficulty with this approach is that it requires signed data while MR tends to be either complex or magnitude only. In an ideal experiment the phase of subsequent points on the decay curve should be the same allowing for the change of sign; however, in practice the phase of subsequent points may drift. Assuming the accumulated drift is less than π and that $\mathrm{TI}_1 << T_1$ for a given recovery curve, the drift can be compensated for by first normalizing the measurements at a given voxel such that the first is real and negative. The values of M_n can then be computed from the normalized complex measurements S_n as

$$M_n = \mathrm{sign}\left(\mathsf{Re}\{S_n\}\right)|S_n| \,. \tag{5.15}$$

In designing the T_1 measurement protocol using a Look-Locker sequence one needs to choose the timing parameters TI_1, TI_2, and TR, as well as the values of N and β. TI_1 and TI_2 should be chosen as short and as long as possible respectively. The repetition period TR is chosen on the basis of the available scanning time and the anticipated T_1 of the subject. The precision of the T_1 estimates drops rapidly as the T_1 exceeds TR. As the number of excitations increases the rate of signal recovery decreases thus reducing the precision with which longer T_1 species can be measured. Conversely, reducing the number of excitations while increasing the interval between excitations reduces the precision with which short T_1 species can be measured. If one has an estimate of T_1 in advance these tradeoff favour choosing a short TR and few excitations so as to save scan time. There is a

similar tradeoff between SNR and signal recovery rate in choosing the excitation flip angle β. A flip angle of 20° degrees has been proposed as a suitable compromise [169].

Variation in the flip angles of both the inversion pulse and the excitation pulses lead to systematic errors in the estimate T_1. While one can account for this by estimating the flip angles from the recovery curves [169], these additional free parameters reduce the precision of the T_1 estimates. Instead, one can make an independent measurement of B_1 and B_0 and correct the flip angles directly. In the case of the excitation pulse, B_0 variations result in a shift of the slice profile and can hence be ignored. The effect of B_1 variations on the excitation pulses can be approximated for small flip angles and/or small field variations as a simple scaling of the flip angle β. For the non-selective inversion pulse, one can account for both B_0 and B_1 variations using the formalism described in section 5.1.2. The magnetization starts in the M_0 state and undergoes the rotations described by equation (5.10). The faction of the magnetization that remains in the M_0 state corresponds to $\cos\alpha$ in equation (5.14). It should be noted that for this case the result is equivalent to that obtain using conventional rotation matrices based on the Bloch equations.

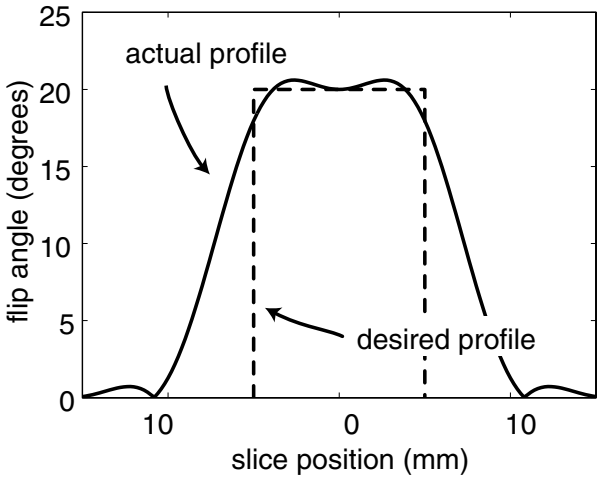

Figure 5.5: Excitation profile for Look-Locker T_1 sequence.

A second consideration in making accurate T_1 measurements is the slice profile of the excitation pulse. For example, if there is a discrepancy between the desired and actual profile such as is shown in Figure 5.5 then T_1 will tend to be overestimated. Using numerical simulations of the Look-Locker sequence taking into account the slice profile, one can generate the recovery curves for a range of T_1 values. Based on the known T_1 and the simulated recovery curves, one can estimate β from equation (5.13) as a function of T_1. In practice, the β estimated in this manner is nearly independent of T_1 [129]. Hence substituting this value of β for the nominal value of β in equation (5.13) compensates for the bias. For the case shown in Figure 5.5, the nominal flip angle is $\beta = 20^\circ$ and the corrected value is $\beta = 17.95 \pm 0.03^\circ$ over the range $0.2\,\mathrm{s} \leq T_1 \leq 3\,\mathrm{s}$. The apparent T_1 before and after correction is plotted in Figure 5.6.

In summary the pulse sequence that was used for T_1 measurements as part of the quantitative MT protocol had the parameters: $\beta = 20^\circ$; $N = 4$; $\mathrm{TI}_1 = 15\,\mathrm{ms}$; $\mathrm{TI}_2 = 495\,\mathrm{ms}$; $\mathrm{TE} = 12\,\mathrm{ms}$; and $\mathrm{TR} = 2\,\mathrm{s}$. The resulting T_1 estimates were compensated for B_1 and

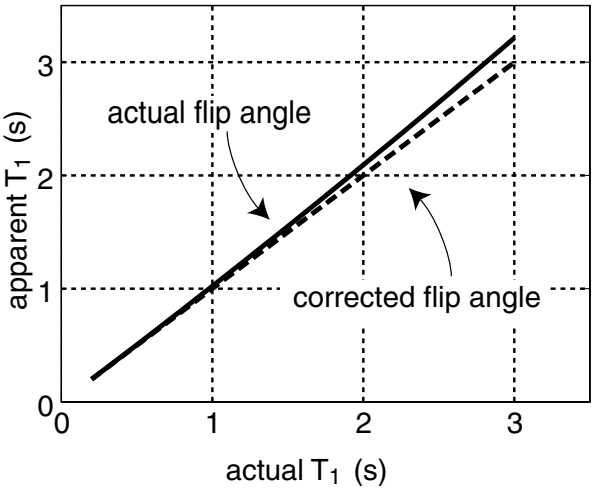

Figure 5.6: Flip angle compensation for slice profile effects in estimating T_1.

B_0 variation using the measured field maps and corrected for slice profile imperfections by adjusting β.

Chapter 6

Magnetization transfer imaging

In this chapter (based on [137]) a novel imaging technique is described that yields all of the observable properties of the binary spin bath model. The application of this method is demonstrated for in vivo studies of the human head. In Chapter 3, different acquisition protocols and signal models used in estimating the parameters of the spin bath model were compared. Based on that analysis, a protocol was designed for in vivo human imaging, which is presented here.

6.1 Theory

The binary spin bath model is formulated as a set of coupled differential equations where the behaviour of the free pool is described by a modified version of the Bloch equation that includes exchange of longitudinal magnetization. The restricted pool is described by an equation for the inverse spin temperature using the Redfield–Provotorov theory [50]. While the field strength and irradiation power in a clinical scanner are such that the restricted pool should be treated in the Provotorov limit where the Zeeman and dipolar terms in the Hamiltonian have their own associated spin temperatures, the experiments with agar gel

described in Chapter 3 [138] as well as NMR experiments with in vitro tissue [97] suggest that the dipolar terms can be safely neglected. The coupled set of differential equations for the spin bath model in a reference frame rotating at a frequency offset Δ from resonance are as follows:

$$\frac{dM_{x,f}}{dt} = -\frac{M_{x,f}}{T_{2,f}} - \Delta M_{y,f} - \mathsf{Im}(\omega_1) M_{z,f} \tag{6.1}$$

$$\frac{dM_{y,f}}{dt} = -\frac{M_{y,f}}{T_{2,f}} + \Delta M_{x,f} + \mathsf{Re}(\omega_1) M_{z,f} \tag{6.2}$$

$$\frac{dM_{z,f}}{dt} = R_{1,f}(M_{0,f} - M_{z,f}) - k_f M_{z,f} + k_r M_{z,r} + \mathsf{Im}(\omega_1) M_{x,f} - \mathsf{Re}(\omega_1) M_{y,f} \tag{6.3}$$

$$\frac{dM_{z,r}}{dt} = R_{1,r}(M_{0,r} - M_{z,r}) - k_r M_{z,r} + k_f M_{z,f} - W M_{z,r} \tag{6.4}$$

where the subscripts f and r denote the free and restricted pools and the subscripts x, y, and z denote the various components of a magnetization vector. The excitation field strength $\omega_1 = \gamma \mathrm{B}_1$ is complex and time varying for general pulses with a circularly polarized coil. By definition, $k_r = k_f / F$ where $F = M_{0,r}/M_{0,f}$ is the ratio of the pool sizes.

The transition rate W for the saturation of the restricted pool for CW experiments in the absence of B_0 field gradients is given by

$$W = \pi \omega_1^2 G(\Delta) \tag{6.5}$$

where G is the lineshape function for the restricted pool and Δ is the frequency offset from resonance of the irradiation. The Gaussian lineshape used in Chapter 3 to model the solid component in gels is replaced here by a super-Lorentzian lineshape which is appropriate for tissues [11, 97]. The lineshape function is given by

$$G(2\pi\Delta) = T_{2,r} \int_0^1 \frac{1}{|3u^2 - 1|} \exp\left(-2 \left(\frac{2\pi \Delta T_{2,r}}{3u^2 - 1} \right)^2 \right) du \,. \tag{6.6}$$

While this expression has a singularity at resonance, other interactions not represented limit its height [158] to an extent that the effect on the restricted pool of the small angle on-resonance pulses used in the imaging experiments is negligible.

To adapt equation (6.5) for the pulsed irradiation typical of an imaging experiment, the lineshape is interpreted as the real part of a complex susceptibility function corresponding to the impulse response of the restricted pool. Since the time lag in the response of such a system is comparable to $T_{2,r}$, this delay is neglected and equation (6.5) is taken to be the time varying transition rate for pulses at an offset frequency Δ.

6.2 Parameter estimation

While equations (6.1) – (6.5) accurately describe the behaviour of the magnetization during a pulsed imaging experiment, the computational complexity of solving these differential equations does not lend itself to rapid estimation of the various model parameters. To contend with this complexity, a number of approximations have been developed that allow one to derive a closed form expression for the signal from a pulsed imaging experiment in which the magnetization system is in a steady state, or more precisely a state in which the time evolution is periodic with the repetition period of the pulses. The speed at which this closed form solution can be computed allows rapid estimation of the model parameters using a curve fitting technique and makes quantitative imaging using the complete 2 pool spin bath model feasible.

A general method for deriving the signal from an MT-weighted pulsed imaging experiment was presented in Chapter 3. Here the focus is restricted to spoiled gradient echo sequences in which shaped off-resonance saturation pulses producing MT contrast are interleaved with small angle on-resonance excitation pulses that are used for gradient echo imaging. A schematic of the pulse sequence used in the imaging experiments is shown in Figure 6.1. For this sequence, the effect that both the off-resonance MT pulses and the on-resonance pulses have on the free pool is approximated as an instantaneous fractional

saturation of the longitudinal magnetization $M_{z,f}$. This saturation fraction, which is denoted S_f, is computed by numerically solving the Bloch equations in the absence of exchange and T_1 recovery and retaining only the fraction of the longitudinal magnetization that remains after the pulse. While at first glance this may seem no more efficient than solving the complete set of differential equations directly, this approach uncouples the direct saturation of the free pool from the exchange process thus allowing one to compute the values of S_f in advance for a particular pulse and a range of $T_{2,f}$. The second advantage of this approach, which becomes apparent after explaining the model of the restricted pool, is in facilitating the steady-state solution of the differential equations.

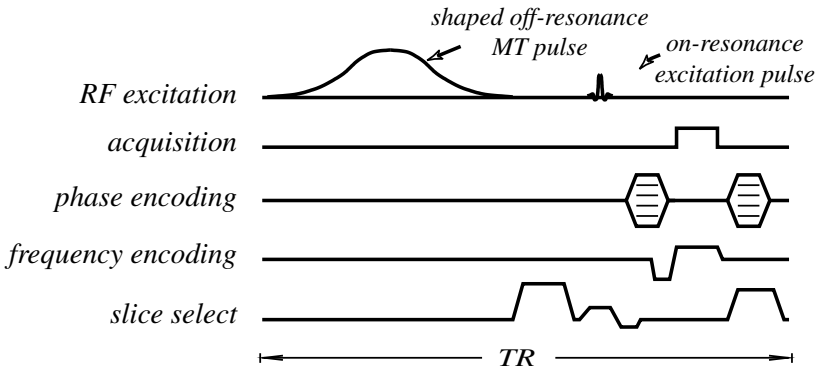

Figure 6.1: An MT-weighted spoiled gradient echo pulse sequence with shaped off-resonance saturation pulses.

In modeling the restricted pool the effect of the on-resonance excitation pulses is neglected and the effect of the off-resonance saturation pulses is modeled in terms of a rectangular pulse of equivalent offset frequency and power. Using these approximations the pulse sequence is broken down into periods of free-precession, off-resonance irradiation at constant power, and instantaneous saturation of the free pool. The decomposition of the

MT-weighted imaging sequence into such periods is shown in Figure 6.2. During each period, the differential equations reduce to a first order system of equations with constant coefficients so that the solution is readily computed without resorting to numerical methods. Solving these equations under the condition that the time evolution is periodic with the repetition period yields a closed form solution for the signal measured when the system has been driven to a steady state.

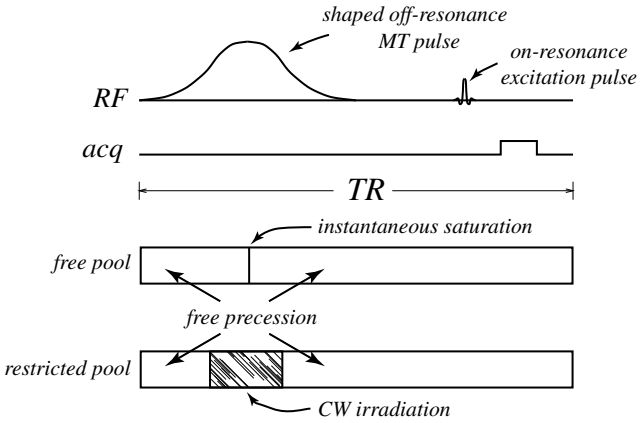

Figure 6.2: Decomposition of the MT-weighted imaging sequence into periods of free-precession, off-resonance irradiation at constant power, and instantaneous saturation of the free pool. The saturation of the free pool due to the MT and excitation pulses has been combined.

Having derived a signal equation for the experiment, the process of parameter estimation is one of choosing a number of combinations of pulse power and offset frequency at which to measure MT-weighted images and then fitting the signal equation at every voxel by choosing the tissue parameters that most closely match the signal equation to the experimental data. Since MT-weighted measurements alone do not constrain all of the parameters

of the model [64], an independent measurement is made of the apparent relaxation rate R_1^{obs} of the system using the inversion recovery type experiment described in section 5.2. R_1^{obs} is the longer of the two apparent relaxation rates for the system and is related to $R_{1,f}$ by equation (3.10) reproduced below

$$R_{1,f} = \frac{R_1^{obs}}{1 + \left(\frac{\left[\frac{k_f}{R_{1,f}} \right] (R_{1,r} - R_1^{obs})}{(R_{1,r} - R_1^{obs}) + k_f/F} \right)} .$$

Since MT experiments of this kind are largely insensitive to $R_{1,r}$ this parameter was set to $1\,\mathrm{s}^{-1}$ with an uncertainty of $\pm 1\,\mathrm{s}^{-1}$ for the purpose of error calculations.

The parameter estimation for the experiments is done on a voxel by voxel basis using a simplex optimization technique [116] to fit the experimental data. To speed the computation, adjacent voxels are used in choosing the starting point of the optimization and lookup tables are employed for repetitive expensive calculations such as the computing of S_f and the super-Lorentzian lineshape function.

6.3 Experiments

While in principle one needs only four MT-weighted images and a T_1 measurement to constrain the five tissue parameters of the spin bath model, in practice such considerations as ensuring a unique solution, verifying the accuracy of the model, and determining the consistency of the data demand more measurements. Since one of the goals of this study was to validate the method, 60 MT-weighted images were collected per study from which the model parameters were derived. Based on the experience with agar gel, a protocol was selected with MT saturation at offset frequencies between 234 Hz and 80 kHz at two different pulse powers. In addition, two sequences were used with two different MT pulse

durations so as to further constrain the estimates of k_f. The complete set of MT-weighted acquisitions in the protocol is summarized in Table 6.1.

Table 6.1: MT-weighted pulse sequence parameters.

protocol	TR	excitation pulse angle	MT pulse angles	MT pulse duration	logarithmic frequency steps
I	25 ms	7°	142°, 710°	10.3 ms	20
II	50 ms	10°	347°, 1388°	30.7 ms	10

Each MT-weighted pulse sequences was designed with 10 s of initial pulsing to drive the system to steady state before the data were acquired (with four signal averages). Since the theory is based on relative saturation, an image was also acquired without MT saturation (with eight signal averages) that was used to normalize the MT-weighted images.

For quantitative imaging it is important to correct for spatial variations in B_1 and B_0. To account for these variations, a B_1 field map was acquired in each session using the spin echo technique described in section 4.2.2. This map was used to correct the MT pulse angles throughout the image. Since the estimates of $T_{2,f}$ are largely determined by the images weighted by MT saturation near the resonance frequency, it is important for the precision of these estimates to control for variations in B_0. This is particularly true of imaging systems in which the transmitter frequency is typically set based on the signal from the whole volume in the absence of field gradients. This frequency can be significantly shifted with respect to the resonance frequency observed during an imaging sequence with strong crushing gradients. To account for this shift, B_0 was measured using the phase

difference technique described in section 4.2.1 based on a modified version of the MT-weighted imaging sequence that has the same pattern of crushing gradients and hence eddy current effects as the MT imaging sequences. These B_0 measurements were then used to shift the offset frequency of the MT pulses in the signal equation on a voxel by voxel basis.

In addition to the MT and field map measurements, R_1^{obs} was measured using the technique described in section 5.2. This data was analyzed using a two parameter fit after correcting the inversion and excitation pulses for B_1 variations and compensating the excitation pulses for slice profile effects [129]. For completeness, an independent measurement of $T_{2,f}$ was made using a 32 echo spin-echo sequence (TE / TR = 10 ms / 2 s). These measurements were compensated for B_1 and B_0 variations using the technique described in section 5.1 [136]. All data was acquired with 2 mm in-plane resolution on a 7 mm thick slice using a 1.5 T clinical MRI system (Siemens Medical Systems, Erlangen GDR).

6.3.1 Validation

To validate the method, experiments were conducted on various concentrations of agar gels as well as a sample of uncooked beef using the imaging protocol described in the previous section. In addition to the imaging experiments, a similar experiment was performed in which a linear field gradient was turned on during the saturation pulses [138, 144]. While this procedure yielded the same information as the imaging experiment, it allowed data to be collected from a homogeneous sample at a large number of offset frequencies in a single measurement. The results of the agar experiments were reported in Chapter 3 and are not repeated here. The agreement of the agar results with published data from NMR experiments [64] establishes the validity of the imaging methodology. Uncooked beef was chosen for validation purposes because it can be obtained in relatively homogeneous samples that facilitate the use of the field gradient technique and because it exhibits a super-Lorentzian

lineshape that is typical for tissue.

6.3.2 In vivo experiments

For the in vivo experiments, two normal subjects and a patient with relapsing / remitting multiple sclerosis were scanned using the complete imaging protocol (35 minutes per subject). Each scan was analyzed on a voxel by voxel basis to yield parametric images for all of the model parameters. In addition, for each subject representative regions of grey and white matter where identified on the R_1^{obs} image. Two lesions were also identified on the scan of the MS patient. The first was a large lesion known to be older than 21 months (based on proton-density-weighted images acquired twice a year prior to this study). The second was a smaller and newer lesion that had appeared during the previous 1 to 9 months.

6.4 Results

6.4.1 Validation results

The fit of the signal equation to the MT data from uncooked beef is shown in Figure 6.3. In this data, a super-Lorentzian lineshape was used to model the restricted pool. The large number of frequency offsets is due the use of the linear gradient. Since the curves are plotted on a logarithmic scale in frequency and the gradient is linear, the sampling appears non-uniform. In fact the data was collected at three different gradient strengths to provide complete coverage of the frequency spectrum. Data was also collected at three different pulse powers rather than the two used in the imaging experiments.

As seen from Figure 6.3, the signal equation accurately predicted the behaviour of the system. The super-Lorentzian shape, which largely determines the lineshape of the curves for large frequency offsets, yielded a close fit for this data as compared to Gaussian or

Lorentzian lineshapes, which produced substantial deviations. As with the agar data, the T_2 estimated from the MT data was lower than that derived from a mono-exponential fit to the spin-echo data. However, the explanation here is likely more straight forward as muscle is known to have multiple free water T_2 components [63]. A T_2 spectral analysis [159] of the spin echo data yielded free water components at $25\,\mathrm{ms}$ and $55\,\mathrm{ms}$. It is likely that both $T_{2,f}$ and T_2^{obs} values reflect a different weighted average of these two water components.

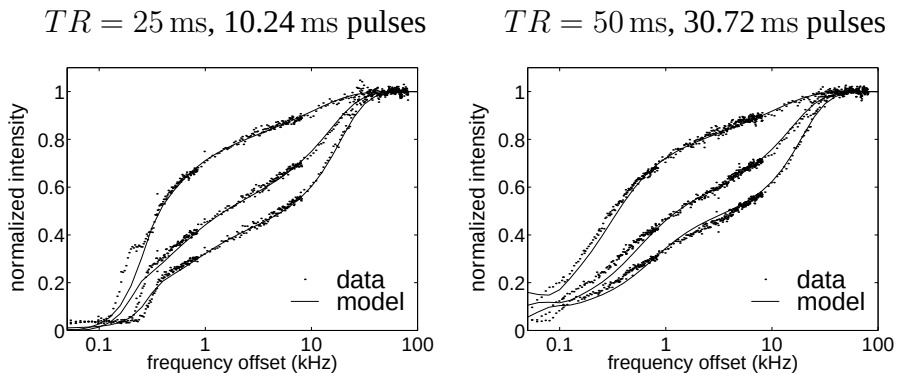

k_f	6.983 $\pm$2.65 s^{-1}	$R_{1,r}$	1.0 $\pm$1.0 s^{-1}
F	0.122 $\pm$0.009	$T_{2,f}$	29.0 $\pm$6.6 ms
$R_{1,f}$	1.69 $\pm$0.13 s^{-1}	$T_{2,r}$	6.6 $\pm$0.5 μs
R_1^{obs}	1.47 $\pm$0.02 s^{-1}	T_2^{obs}	46 $\pm$1 ms

RMS error: 0.026 (frequency offsets $>$ 800 Hz)

Figure 6.3: A fit of the signal equation to data from MT-weighted gradient echo scans with pulsed irradiation at various offset frequencies and powers. These results are for uncooked beef and take into account the super-Lorentzian lineshape typical of the restricted pool in tissue. The parameter estimates are derived from a simultaneous fit to all of the data shown.

6.4.2 In vivo results in normals

Parameter images for a transverse slice through the brain of a normal subject are shown in Figure 6.4. The parameter images for $T_{2,f}$ and $R_{1,f}$ showed the contrast normally seen in T_2-weighted and T_1-weighted scans respectively. It is of note that there was a subtle contrast of approximately 2 μs seen between grey and white matter in the T_2 of the restricted pool ($T_{2,r}$). The fractional pool size F, as expected, was larger in white matter than in grey matter, consistent with the view that the fractional pool size should be correlated with myelination. The fractional pool size seen for white matter was not uniform, with larger values seen across the corpus callosum and in the frontal lobes. The k_f image showed similar contrast to the F image. An alternate formulation of the model is to express magnetization exchange as the product of an exchange constant and the concentrations of the two pools [64]. Computing the ratio of k_f to F suggested that this exchange constant was nearly the same for grey and white matter.

Parameter estimates derived from selected regions of grey and white matter in two normal subjects are given in Table 6.2. The white matter regions of interest for both subjects were selected in the frontal lobes; the grey matter was selected from the caudate nucleus in the first subject and from the cortex in the second. The cortical grey matter sample may have been contaminated by partial volume effects given the relatively large voxel size. As before, a discrepancy was seen between the two measures of $T_{2,f}$. The larger difference seen in white matter is likely due to a second free water component with a T_2 between 20 ms and 40 ms [85]. The MT-weighted measurements along with the fit of the signal equation for the two regions of interest in the first subject are shown in Figure 6.5. The residual errors for these fits were 2.6% and 2.7% for white and grey matter respectively. The high SNR in these measurements means that most of the residual error is due to systematic errors or limitations of the model.

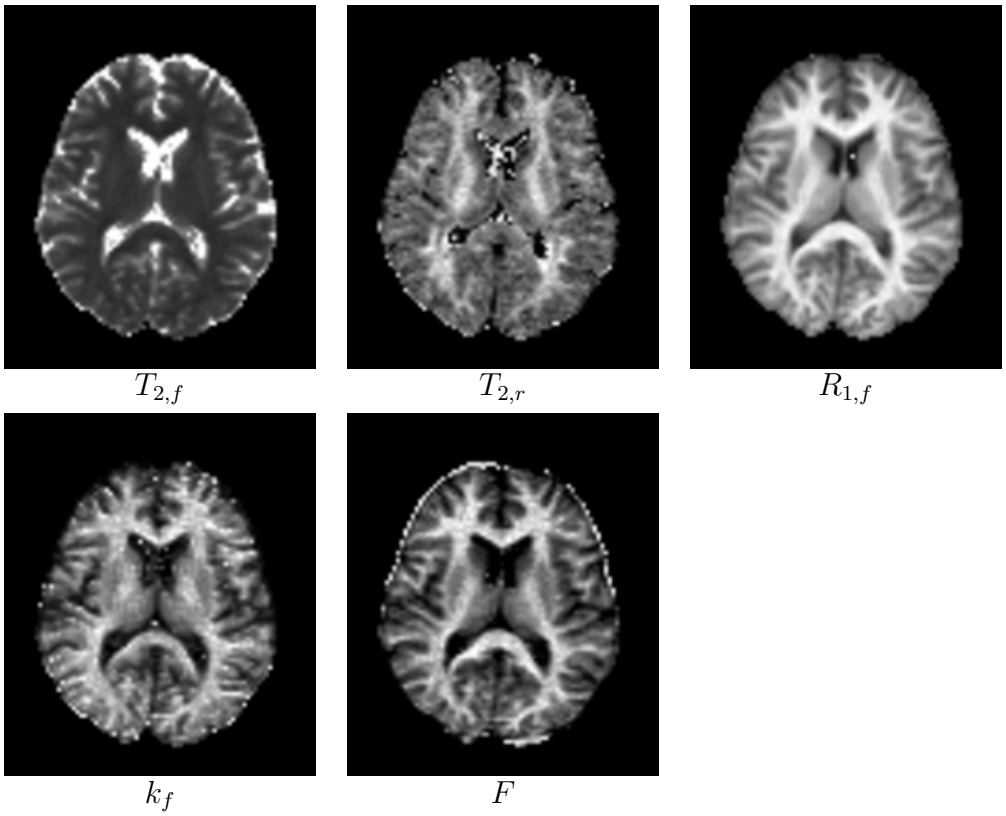

Figure 6.4: Parameter images derived from fitting the signal equation to a series of MT-weighted images of a normal subject.

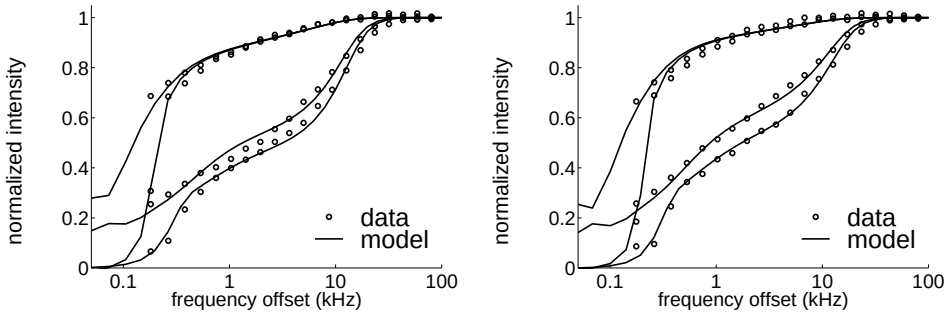

(a) (b)

Figure 6.5: The signal equation fit to in vivo measurements from regions of white matter (a) and grey matter (b) in a normal subject. The residual errors for these fits were 2.6% and 2.7% for white and grey matter respectively.

Table 6.2: Parameter estimates for grey and white matter derived from selected regions in two normal subjects. The error estimates are for a 95% confidence interval derived from the residual error in the fit of the signal equation.

	subject 1		subject 2	
	caudate nucleus	frontal white matter	cortical grey matter	frontal white matter
k_f	2.2 $\pm$1.0 s^{-1}	4.6 $\pm$1.3 s^{-1}	2.4 $\pm$0.8 s^{-1}	4.3 $\pm$1.0 s^{-1}
F	0.056 $\pm$0.010	0.152 $\pm$0.023	0.072 $\pm$0.013	0.161 $\pm$0.025
$R_{1,f}$	0.99 $\pm$0.16 s^{-1}	1.8 $\pm$0.3 s^{-1}	0.93 $\pm$0.2 s^{-1}	1.8 $\pm$0.3 s^{-1}
$T_{2,f}$	55 $\pm$8 ms	31 $\pm$5 ms	56 $\pm$8 ms	37 $\pm$8 ms
$T_{2,r}$	9.7 $\pm$1.6 μs	11.8 $\pm$1.3 μs	11.1 $\pm$1.3 μs	12.3 $\pm$1.6 μs
R_1^{obs}	0.99 $\pm$0.14 s^{-1}	1.72 $\pm$0.25 s^{-1}	0.95 $\pm$0.20 s^{-1}	1.7 $\pm$0.2 s^{-1}
T_2^{obs}	93 $\pm$5 ms	79 $\pm$4 ms	92 $\pm$3 ms	82 $\pm$4 ms

6.4.3 In vivo results in an MS patient

Parametric images derived from a scan of an MS patient are shown in Figure 6.6. On this slice, several lesions are visible, characterized by a smaller fractional pool size, a smaller exchange rate, longer relaxation times in the free pool ($T_{1,f}$ and $T_{2,f}$), and shorter spin-spin relaxation times in the restricted pool ($T_{2,r}$). Two lesion were identified on the $R_{1,f}$ image (see arrows on Figure 6.6) and used to define regions of interest. Parameter estimates derived from these regions of interest along with those for selected regions of normal appearing grey and white matter are given in Table 6.3. The second lesion, the newer of the two, is closer in its properties to white matter, whereas the first has a significantly reduced

fractional pool size and longer $T_{2,f}$.

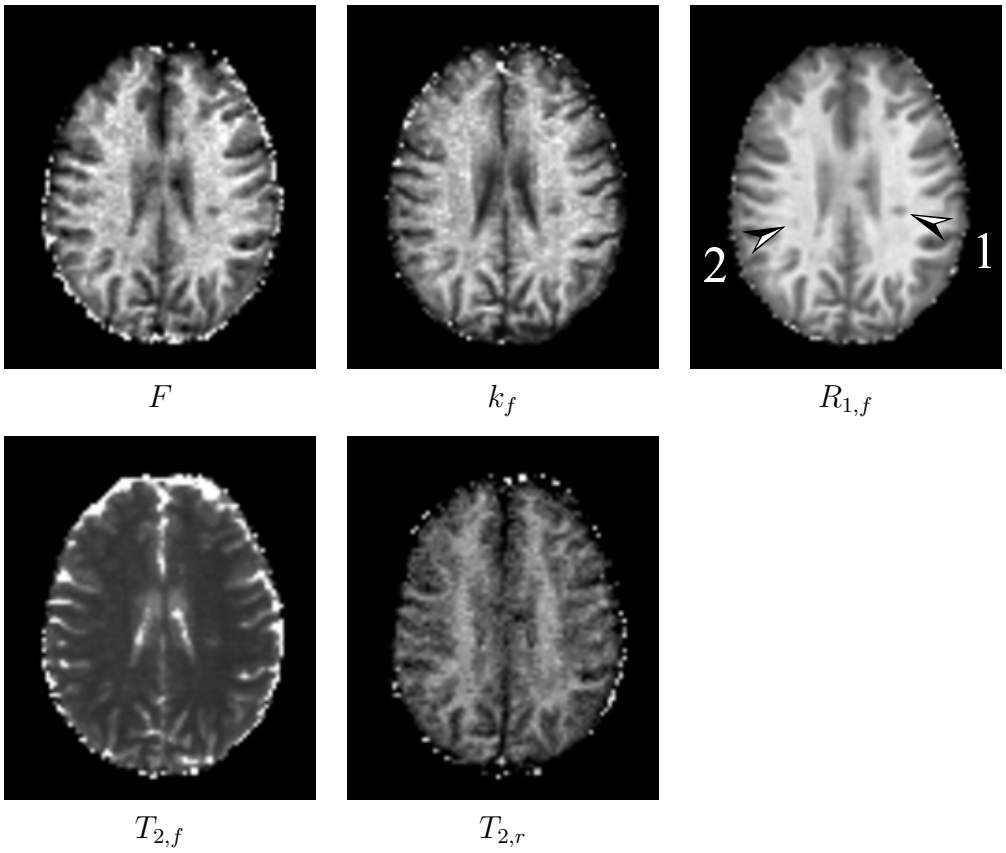

Figure 6.6: Parameter images for a patient with multiple sclerosis. Two lesions have been indicated by arrows on the $R_{1,f}$ $(= 1/T_{1,f})$ parameter image. These are characterized by a smaller fractional pools size (F), a smaller exchange rate (k_f), longer relaxation times in the free pool ($T_{1,f}$ and $T_{2,f}$), and shorter spin-spin relaxation times in the restricted pool ($T_{2,r}$).

Table 6.3: Parameter estimates from four ROIs on a scan of an MS patient.

	cortical grey matter	frontal white matter	lesion 1 (21+ months)	lesion 2 (1–9 months)
k_f	2.6 $\pm 1\,\mathrm{s}^{-1}$	4.9 $\pm 1.3\,\mathrm{s}^{-1}$	2.7 $\pm 0.7\,\mathrm{s}^{-1}$	3.6 $\pm 0.8\,\mathrm{s}^{-1}$
F	0.068 ± 0.011	0.15 ± 0.02	0.094 ± 0.015	0.12 ± 0.02
$R_{1,f}$	0.89 $\pm 0.1\,\mathrm{s}^{-1}$	1.78 $\pm 0.4\,\mathrm{s}^{-1}$	1.26 $\pm 0.3\,\mathrm{s}^{-1}$	1.52 $\pm 0.2\,\mathrm{s}^{-1}$
$T_{2,f}$	62 $\pm 11\,\mathrm{ms}$	38 $\pm 7\,\mathrm{ms}$	51.5 $\pm 9\,\mathrm{ms}$	43 $\pm 6\,\mathrm{ms}$
$T_{2,r}$	9.6 $\pm 1.4\,\mu\mathrm{s}$	11.4 $\pm 1.4\,\mu\mathrm{s}$	10.9 $\pm 1.4\,\mu\mathrm{s}$	10.3 $\pm 1.1\,\mu\mathrm{s}$
R_1^{obs}	1.67 $\pm 0.34\,\mathrm{s}^{-1}$	0.89 $\pm 0.09\,\mathrm{s}^{-1}$	1.23 $\pm 0.22\,\mathrm{s}^{-1}$	1.46 $\pm 0.12\,\mathrm{s}^{-1}$
T_2^{obs}	85 $\pm 4\,\mathrm{ms}$	91 $\pm 4\,\mathrm{ms}$	120 $\pm 5\,\mathrm{ms}$	98 $\pm 5\,\mathrm{ms}$

6.5 Conclusion

In summary, the method described allows, for the first time, the quantitative in vivo imaging of all the observable parameters of the binary spin bath model. Specifically, this yields the fractional size of the restricted pool, the magnetization exchange rate, the T_2 of the restricted pool as well as the relaxation times of the free pool. These are physically independent parameters with the potential to give new information about tissue composition and structure. Their interpretation is discussed further in the following chapter.

Chapter 7

Discussion and conclusions

7.1 Quantitative magnetization transfer imaging

MULTIPLE sclerosis is one of several conditions for which magnetization transfer may provide improved pathological specificity. However, the conventional approach of computing MT ratios limits the interpretation of these results. An MT ratio experiment yields a single point on a curve such as those shown in Figure 6.3 and reflects a complex combination of the various relaxation and exchange properties. Moreover, the values measured in such an experiment, while typically reproducible, cannot be compared between various protocols and sites [9] because the measured signal depends strongly on the pulse sequence details and experimental conditions. By modeling the phenomenon and compensating for experimental factors such as field variations and eddy current effects, it has been shown here that one can derive properties that have a physical interpretation and are comparable with published values from model systems.

In the case of agar gel, there is good agreement between the results of the new method and the published results of Henkelman et al. [64] (compare Table 3.1 and the results without dipolar terms in Table 3.4). While the properties of agar differ in a number of respects

from those of tissue, the experiments on uncooked beef confirm that the pulsed MT model also provides a close fit for tissues. In the case of in vivo measurements of brain tissue, the published data is limited. Chai et al [22] reported the fractional pool size to be three times larger in white matter and 50% smaller in grey matter than the values reported here. However, since the model used was based on a Lorentzian lineshape for the restricted pool, it is not clear that this comparison is meaningful. A more comparable experiment is that of Morrison et al. [97] in which a similar NMR experiment, taking into account the super-Lorentzian lineshape of the restricted pool, was performed on excised bovine brain tissue. These results were presented in terms of the lumped parameters $[k_f/F]$, $[k_f/R_{1,f}]$, $[(R_{1,f}T_{2,f})^{-1}]$, and $[T_{2,r}]$. On average, the ratios $[k_f/F]$ and $[k_f/R_{1,f}]$ measured here were 25% larger than those reported for bovine grey and white matter. The values of $[(R_{1,f}T_{2,f})^{-1}]$ determined here were 30% lower for white matter but in agreement within the error bounds for grey matter. For both white and grey matter, the $T_{2,r}$ found here agreed within the margin of error with the reported values. While one can speculate as to what experimental factors could account for these differences, they may attributable to biological differences alone.

An issue that challenges the physical interpretation of the results is the validity of the model. In particular, the binary spin bath model does not take into account the multiple free water T_2 components observed in white matter [85]. To address this issue, Stanisz et al. [142] have described a four pool model in which two free water components exchange magnetization with their respective restricted pools and with each other. Using a 2D NMR technique combining MT weighting and spectral T_2 measurements, the parameters of this model were determined for bovine optic nerve. In their findings, the free water component with the shorter T_2, roughly 30% of the total water, exchanges rapidly with its restricted pool. In an MT experiment, this rapid exchange manifests itself through exchange between the free water pools as increased indirect saturation of the long T_2 free water component.

A means of reconciling the two models is to view the two pool model as a projection of the four pool model. In fact, the four pool model is likely itself a simplification of a more complete model having many compartments and exchange pathways. In this view, the fractional pool size represents a weighted sum of the various restricted pools present. Given that the time for the two free pools to equilibrate is approximately 200 ms [156] while steady-state conditions in the experiment take several seconds to be established, one can assume that the two free pools are near equilibrium throughout the experiment when the frequency of the irradiation is sufficiently offset from resonance to avoid oscillatory behaviour (ie. greater than about 200 Hz for the human imaging protocol described here). Moreover, the two pool simplification may not introduce significant error since the role that the short T_2 free water component plays in the pulsed MT experiments is small. Given that the exchange rate is large enough that the free and restricted pools equilibrate between saturation pulses and that these pulses are relatively short and intense, the amount of saturation observed has more to do with the size of the pools than the exchange rates. Since the fractional size of the short T_2 free pool is typically 15% in human white matter [85] and the associated restricted pool is perhaps 20% of this amount, the magnetization that can be drawn though this pathway with each repetition, which is at most 3%, is small compared to the 15% observed here as the fractional size of the restricted pool.

In principle, one would like a complete characterization of the relaxation properties of all of the water and macromolecular species present as well as the rates at which they exchange. However, the number of measurements needed to acquire a two or more dimensional spectrum of data at every voxel is incompatible with the time constraints of clinical imaging. The spectrum of MT data acquired using the imaging protocol is in a sense a projection of this multi-dimensional measurement space just as T_2 spectral analysis yields a projection along another axis. While this may be insufficient for the general case of

an arbitrary combination of water and macromolecular species, in practice one can take advantage of in vitro studies as well as an understanding of the structure and chemistry to correctly interpret the results of such experiments. Tissues such as white matter are believed appropriate for study in this manner.

7.2 Future work

The logical direction for this work on quantitative MT imaging to proceed is to apply the methodology to the study of clinical conditions, and in particular multiple sclerosis (MS). For example, a number of authors [32, 38, 45, 83, 94, 109] have reported small reductions in MTR values for normal appearing white matter in MS patients; however, the interpretation of these changes in terms of edema, demyelination, and axonal damage remains uncertain. Scanning of these patient along with normal subjects using the quantitative MT protocol would allow for the respective distributions of the relaxation and exchange properties to determined. Combining these results with an analysis of the T_2 data, the differences could then be interpreted in terms of both: changes in the properties and concentrations of the free and restricted pools; and changes in the properties and concentrations of intra / extra cellular water and myelin water [85].

While a number of clinical questions can be addressed using the existing MT imaging methodology, a comprehensive investigation of the pathology of MS will require further development of both the theory and implementation. First among these developments should be the implementation of a protocol with whole head coverage within perhaps one hour of scan time. Such a protocol would allow for a detailed longitudinal study of MS patients in which one could retrospectively analyse [39, 52, 110, 111] the MT properties of regions of normal appearing white matter that subsequently developed into lesions.

In designing a whole head protocol, one would need advanced readout techniques, such as multi-shot spiral or segmented EPI, that allow for an 8 or 10 fold decrease in the scan time per slice. Given that the multiple signal averages currently acquired translate directly into multiple slices in a 3D acquisition, the MT-weighted measurements could be acquired with 32 slices without increasing the total scan time. Using a similar strategy, the other pulses sequences in the protocol could be generalized to multiple slices with only a modest increase in scan time. This increase could be recovered by optimizing the sampling strategy to reduce the number of MT-weighted measurements that are acquired.

A second aspect of the methodology to develop is a more rigorous theoretical basis for the interpretation of MT and T_2 data in which more than one free water component is present. While one can argue that the additional free water component in white matter does not invalidate the MT model, these arguments are based on the known and hypothesized properties of the different pools as well as the conditions under which the experiments are conducted. If the data could be analysed in a manner that took into account both the T_2 and MT properties, these assumptions could be relaxed, potentially broadening the number of applications and experimental designs to which the theory could be applied.

7.3 Summary and conclusions

Magnetization transfer imaging is an MRI technique that generates contrast dependent upon the phenomenon of magnetization exchange between semi-solid macromolecular protons and water protons. This technique has the ability to image in vivo semi-solids, such as protein matrices and cell membranes, whose magnetization dies away too quickly to be imaged directly. Preliminary in vitro and in vivo results suggest that MT quantification may allow characterization of the pathologically heterogeneous lesions of multiple sclero-

sis (MS) by providing a measure of demyelination. However, MT imaging, as currently applied, is only a semi-quantitative technique that reflects a complex combination of tissue and experimental parameters in addition to MT.

The thesis describes a novel quantitative MT imaging technique based on a two pool model for magnetization exchange. The combination of a new signal equation for pulsed MT experiments, efficient parameter estimation, compensation for excitation field non-uniformity, and precise relaxometry allows images to be formed of the intrinsic properties that characterize the MT phenomenon. Specifically, this approach yields parametric images of the fractional size of the semi-solid pool, the magnetization exchange rate, the spin-spin relaxation rate of the semi-solid pool as well as the relaxation times of the water protons. Validated experimentally on agar gels and in vitro tissue samples, the application of the method is demonstrated on normal subjects and a patient with multiple sclerosis.

Quantitative MT imaging when used in combination with existing techniques such as T_2 spectral analysis allows for a new and more detailed in vivo examination of tissue structure. If current theories of magnetization transfer in white matter are upheld, this approach could provide a means of measuring specific pathological features of disease load and progression in MS patients and thus have a significant impact upon the design and statistical power of future therapeutic trials. The developed methodology provides a general tool for quantitative MRI based tissue characterization with potential applications in a diverse range of diseases.

Appendix A

Radio frequency field variations

The following manuscript appeared in IEEE Transactions on Medical Imaging, vol. 17, no. 4, pp. 653–662, 1998.

Standing-wave and RF penetration artifacts caused by elliptic geometry: an electrodynamic analysis of MRI

JOHN G. SLED AND G. BRUCE PIKE

Abstract: Motivated by the observation that the diagonal pattern of intensity non-uniformity usually associated with linearly polarized radio-frequency (RF) coils is often present in neurological scans using circularly polarized coils, a theoretical analysis has been conducted of the intensity non-uniformity inherent in imaging an elliptically shaped object using 1.5T magnets and circularly polarized RF coils. This first principles analysis clarifies, for the general case of conducting objects, the relationship between the excitation field and the reception sensitivity of circularly and linearly polarized coils. The results, validated experimentally using a standard spin echo imaging sequence and an *in vivo* B_1 field mapping technique, are shown to be accurate to within 1%-2% rms, suggesting that these electromagnetic interactions with the object account for most of the intensity non-uniformity observed.

Keywords: Intensity non-uniformity, magnetic resonance imaging, RF field inhomogeneity, shading artifact.

A.1 Introduction

Intensity non-uniformity is the smooth intensity variation often seen in MR images caused by such factors as inhomogeneous RF excitation [93], non-uniform reception coil sensitivity, eddy currents driven by field gradients [132], as well as the electrodynamic interactions

with the object often described as RF penetration and standing wave effects [15]. In modern MRI scanners using circularly polarized head or body coils that produce nominally uniform fields, these variations are often subtle enough that they are difficult to detect by visual inspection. However, the increasing use of automatic segmentation techniques, which assume homogeneity of intensity within each tissue class, has driven interest in correcting this artifact [28, 95, 100, 157, 139], as it can significantly degrade their performance.

A number of authors have conducted theoretical analyses of the excitation field (B_1) and reception sensitivity variations that contribute to image intensity non-uniformity. This kind of analysis is greatly simplified by treating the excitation field as static and using the Biot-Savart law to compute magnetic field strength by integrating the contributions of nearby currents [93, 99]. While this approach simplifies the modeling of complicated coil shapes, it neglects penetration and standing wave effects that are present under the true dynamic conditions. As main magnetic field strength B_0 increases, the MR resonant frequency increases and the wavelength of the excitation B_1 field decreases. Hence, the approximation of a quasi-static excitation field, which is equivalent to assuming very long wavelengths, becomes less valid at higher field strengths.

The results of an analysis assuming static fields will at best match measurements made by placing a small pickup coil within the unloaded RF coil. Birdcage head coils have been measured in this manner to have in-plane uniformity with as little as 1% variation[1] when operating at 64 MHz (suitable for a standard 1.5 T magnet). However, since image intensity variations of 20% are often observed at this field strength, a model that predicts 1% variation is clearly unsatisfactory.

Initial attempts at dynamic modeling of MR excitation [15, 89] predicted that pene-

[1] Field variation is given as the ratio of the range of field strengths to their mean computed over the volume of interest.

tration effects would significantly degrade performance at frequencies above 30MHz. As 64MHz (1.5T) machines have since become standard for clinical imaging, these predictions were clearly overly pessimistic. It has been suggested [132, 124] that this discrepancy is due to insulating structures in biological tissue that prevent large current loops from forming. However, calculations by Glover et al. [47] show substantially greater field penetration that has been confirmed by experiments with a cylindrical phantom at 64MHz. A similar calculation by Zypman [171], taking into account the influence of the RF coil, arrived at the same solution for the field within a cylindrical phantom. Analysis of this kind predicts image intensity variations of 10% to 20% in a head size structure, which is consistent with typically observed values. The magnitude of these variations suggest that electrodynamic interactions, rather than other effects such as deficiencies in the scanner, are the primary cause of intensity non-uniformity for 1.5 T machines.

A difficulty with analytic modeling is that closed form solutions are only available for simple geometries. Finite elements offer a more flexible approach to dynamic modeling of complicated structures. The problem of modeling the excitation field within the human head has been treated by a number of authors [133, 155, 70]. Šimunić et al. [133] make the approximation of quasi-static conditions outside the head in modeling the fields generated by a linearly polarized saddle coil at 64MHz. The results of these simulations have been validated *in vivo* using the dual flip-angle technique described in [143]. Similar measurements [143] using a birdcage (circularly polarized) head coil did not detect a significant variation in B_1 field strength. These authors did not, however, use their results to predict the effect that these field variations have on image intensity variations.

In this paper, we investigate the extent to which electromagnetic interactions with the object account for the intensity non-uniformity observed in standard volumetric scans. To do so, we develop an analytic solution for the excitation field and reception sensitivity when

imaging a cylinder with elliptic cross section. In the process, we clarify for the general case of a conducting object the relationship between the excitation field and the reception sensitivity of a coil. In addition, we investigate the hypothesis that an elliptically shaped object leads to a diagonal pattern of non-uniformity, even when excited by a circularly polarized coil. Our results are validated with phantom studies using both a standard imaging sequence and an *in vivo* B_1 field mapping technique.

A.2 Methods

A.2.1 Modeling the excitation field and reception sensitivity

While a variety of experimental and numerical approaches are available to investigate the effect of eccentric geometry on intensity non-uniformity, an analytic approach is used here for simplicity.

This treatment considers a long homogeneous dielectric cylinder with elliptic cross section excited by a circularly polarized field perpendicular to the cylinder axis. Only regions far from the ends of the cylinder are considered, interaction with the RF coils is neglected, and far from the cylinder the excitation field (B_1) is assumed to be uniform. The propagation of electric and magnetic fields in dielectric media is governed by the equations:

$$\nabla^2 \mathbf{E} = \mu\epsilon \frac{\partial^2 \mathbf{E}}{\partial t^2} + \frac{\mu}{\rho}\frac{\partial \mathbf{E}}{\partial t} \tag{A.1}$$

$$\nabla \times \mathbf{E} = -\frac{\partial \mathbf{B}}{\partial t}\,, \tag{A.2}$$

where $\mathbf{E}$ and $\mathbf{B}$ are the electric and magnetic fields respectively, μ is the magnetic permeability, ϵ is the permittivity, and ρ is the resistivity of the media. The magnetic field B_1 is assumed to be oriented perpendicular to the cylinder axis while the electric field is oriented parallel. In addition, the solutions for the real vector fields $\mathbf{E}$ and $\mathbf{B}$ are assumed to vary

sinusoidally in time at an angular frequency ω such that

$$\mathbf{E} = \mathsf{Re}\left\{E_z \hat{z} e^{j\omega t}\right\} \tag{A.3}$$

$$\mathbf{B} = \mathsf{Re}\left\{(B_x \hat{x} - jB_y \hat{y}) e^{j\omega t}\right\} . \tag{A.4}$$

Suppose the cross section of the ellipse is as shown in Figure A.1a with major and minor radii r_x and r_y respectively. Let $2l$ be the interfocal distance given by

$$l = \sqrt{r_x^2 - r_y^2} . \tag{A.5}$$

This geometry is simply expressed in a coordinate system formed from confocal ellipses and hyperbolas such that the radial and circumferential elliptic coordinates ξ and η are related to the Cartesian coordinates by:

$$x = l \cosh\xi \cos\eta \tag{A.6}$$

$$y = l \sinh\xi \sin\eta \tag{A.7}$$

$$z = z . \tag{A.8}$$

Lines of constant ξ are ellipses, while lines of constant η are hyperbolas. Some examples are shown in Figure A.1b.

This change of coordinates is one-to-one for $\xi > 0$ and $-\pi < \eta \leq \pi$ and can be inverted as follows

$$r_1 = \sqrt{(x-l)^2 + y^2} \tag{A.9}$$

$$r_2 = \sqrt{(x+l)^2 + y^2} \tag{A.10}$$

$$\xi = \cosh^{-1}\left(\frac{r_1 + r_2}{2l}\right) \tag{A.11}$$

$$\eta = \mathrm{sign}(y) \cos^{-1}\left(\frac{r_2 - r_1}{2l}\right) . \tag{A.12}$$

Using equations (A.3) and (A.4), equations (A.1) and (A.2) can be rewritten in elliptic

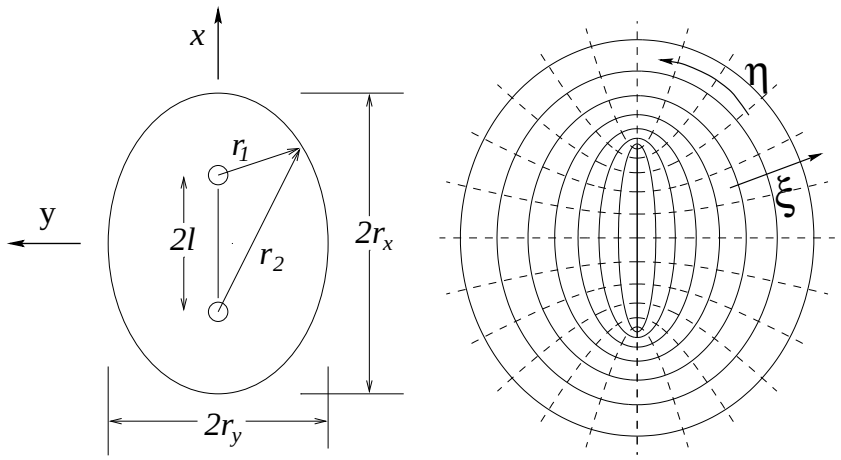

(a) (b)

Figure A.1: Elliptic cylinder geometry and corresponding coordinate system.

coordinates as

$$\frac{1}{\frac{1}{2}l^2(\cosh 2\xi - \cos 2\eta)}\left(\frac{\partial^2 E_z}{\partial \xi^2} + \frac{\partial^2 E_z}{\partial \eta^2}\right) + \frac{\partial^2 E_z}{\partial z^2} + k^2 E_z = 0 \tag{A.13}$$

$$\mathbf{B} = \frac{j}{\omega l\sqrt{\frac{1}{2}(\cosh 2\xi - \cos 2\eta)}}\left(\frac{\partial E_z}{\partial \eta}\hat{\xi} - \frac{\partial E_z}{\partial \xi}\hat{\eta}\right), \tag{A.14}$$

where $\hat{\xi}$ and $\hat{\eta}$ are unit vectors in the direction of the respective coordinates. k is the complex wave number given by $k = 2\pi/\lambda$, where

$$\lambda = \lambda_0/\sqrt{\epsilon_r - j/\omega\epsilon_0\rho} \tag{A.15}$$

$$\lambda_0 = \frac{2\pi}{\omega\sqrt{\mu_0\epsilon_0}}. \tag{A.16}$$

λ is the reduced wavelength in the medium, λ_0 is the free space wavelength, ϵ_0 and μ_0 are the permittivity and permeability of free space, and $\epsilon_r = \epsilon/\epsilon_0$ is the relative permittivity of the media. While in general ϵ_r is complex to account for losses due to bound electrons, these losses are typically small at the frequencies of interest for MRI. The magnetic permeability of biological materials differs little from that of free space [1] so we let $\mu = \mu_0$.

Since the cylinder is long, the z dependence of E_z can be ignored. Equation (A.13) is separable and admits solutions of the form $E_z = \Psi(\xi)\Phi(\eta)$ where Ψ and Φ are solutions of Mathieu's circumferential differential equation

$$\frac{d^2\Phi}{d\eta^2} + \left(c - \frac{h^2}{2}\cos 2\eta\right)\Phi = 0 \tag{A.17}$$

and Mathieu's radial differential equation

$$\frac{d^2\Psi}{d\xi^2} - \left(c - \frac{h^2}{2}\cosh 2\xi\right)\Psi = 0\,. \tag{A.18}$$

The two solutions Ψ and Φ are linked by c, referred to as the separation constant or Mathieu characteristic number (MCN). The constant $h = lk$.

For a given value of h there is an infinite set of discrete MCNs for which the solution to (A.17) is of period 2π. These solutions come in even and odd varieties referred to as $\mathrm{Se}_n(h,\eta)$ and $\mathrm{So}_n(h,\eta)$ respectively, and are analogous to the set of sines and cosines that are solutions to the problem of a cylinder with circular section. The corresponding solutions to the radial equation (A.18) are even and odd radial Mathieu functions of the first through fourth kind. Radial Mathieu functions of the first and second kind, evoked by an elliptic geometry, are analogous to Bessel functions, evoked by a circular geometry.

The Mathieu functions Se and So can be represented in terms of a sum of sines and cosines where the coefficients are related by a recurrence relation [2, 5]. The same set of coefficients is used to compute the corresponding radial Mathieu function expressed in terms of Bessel functions. The coefficients along with their corresponding MCNs are found using the non-linear numerical optimization technique described in [5].

The problem of excitation by a circularly polarized coil is treated as excitation by two linearly polarized coils producing magnetic fields parallel to the x and y axes respectively. The problem is simplified by assuming, as in [47, 133], that the conditions outside the cylinder can be treated quasi-statically by taking k to be zero. This is valid provided the

wavelength λ is much larger than the region of interest. At 64MHz, λ is $4.7\mathrm{m}$ in air but only $53\mathrm{cm}$ in water; hence the quasi-static approximation is valid outside the cylinder but not inside for the cases considered in the following sections[2].

Taking $h = 0$, equations (A.17) and (A.18) reduce to the Helmholtz equation and admit solutions of the form

$$\Psi_n(\xi) = e^{\pm n\xi} \tag{A.19}$$

$$\Phi_n(\eta) = \cos n\eta \tag{A.20}$$

$$\Phi_n(\eta) = \sin n\eta\,. \tag{A.21}$$

Treating the linearly polarized coil with axis oriented in the y direction first, the amplitude of the magnetic field far from the cylinder is required to be constant and oriented along y. The general solution for E_z satisfying this constraint is

$$E^e_{zy} = j\omega h B_1 \left(e^{\xi}\cos\eta + \sum_{m=1}^{\infty} p_m e^{-m\xi}\cos m\eta \right)\,, \tag{A.22}$$

where B_1 is the magnitude of the magnetic field far from the cylinder and the notation E^e_{zy} refers to the z component of the electric field external to the cylinder due to a y polarized coil.

Applying equation (A.14) to this solution leads to an expression for the radial and circumferential components of the magnetic field:

$$B^e_{\xi y} = B_1 G(\xi,\eta)\left(e^{\xi}\sin\eta + \sum_{m=1}^{\infty} m p_m e^{-m\xi}\sin m\eta \right) \tag{A.23}$$

$$B^e_{\eta y} = B_1 G(\xi,\eta)\left(e^{\xi}\cos\eta - \sum_{m=1}^{\infty} m p_m e^{-m\xi}\cos m\eta \right) \tag{A.24}$$

where

$$G(\xi,\eta) = \frac{1}{\sqrt{\frac{1}{2}(\cosh 2\xi - \cos 2\eta)}}\,. \tag{A.25}$$

[2]The analysis of an elliptic cylinder is tractable without the assumption of quasi-static conditions outside the cylinder. However for the cases considered, the effect on the solution within the cylinder is negligible.

These solutions have the desired property that far from the cylinder the field is aligned with the y axis. That is

$$lim_{\xi\to\infty} B^e_{\xi y} = lim_{\xi\to\infty} \frac{B_1 e^{\xi}\sin\eta}{\cosh\xi} = B_1 \sin\eta \tag{A.26}$$

$$lim_{\xi\to\infty} B^e_{\eta y} = lim_{\xi\to\infty} \frac{B_1 e^{\xi}\cos\eta}{\cosh\xi} = B_1 \cos\eta\,. \tag{A.27}$$

The general solutions with corresponding symmetry for the interior of the cylinder are

$$E^i_{zy} = j\omega h B_1 \sum_{n=0}^{\infty} q_n \mathrm{Je}_n(h,\xi)\mathrm{Se}_n(h,\eta) \tag{A.28}$$

$$B^i_{\xi y} = -B_1 G(\xi,\eta) \sum_{n=0}^{\infty} q_n \mathrm{Je}_n(h,\xi)\mathrm{Se}'_n(h,\eta) \tag{A.29}$$

$$B^i_{\eta y} = B_1 G(\xi,\eta) \sum_{n=0}^{\infty} q_n \mathrm{Je}'_n(h,\xi)\mathrm{Se}_n(h,\eta) \tag{A.30}$$

where Je_n are even radial Mathieu functions of the first kind. The radial functions of the first kind have been chosen to satisfy the requirement that the magnetic field be continuous across the cut in the coordinate system corresponding to $\xi = 0$.

It should be noted that, unlike the case of a cylinder with circular section, there is not a one-to-one correspondence between the individual terms of the interior solution and the exterior solution. The problem of matching the interior solutions at the boundary is overcome by truncating the series solutions and solving for the coefficients numerically. Similarly, the series expressions for the individual Mathieu functions are truncated to make numerical evaluation tractable. In practice, the coefficients in these series drop off extremely rapidly and the series can be accurately approximated by a small number of terms. Details of this calculation are given in the appendix.

The solution for the linearly polarized coil oriented along x is similar. The expressions for the electric and magnetic fields are

$$E^e_{zx} = -j\omega h B_1 \left(e^{\xi}\sin\eta + \sum_{m=1}^{\infty} p_m e^{-m\xi}\sin m\eta \right) \tag{A.31}$$

$$B^e_{\xi x} = B_1 G(\xi,\eta)\left(e^{\xi}\cos\eta + \sum_{m=1}^{\infty} m p_m e^{-m\xi}\cos m\eta\right) \tag{A.32}$$

$$B^e_{\eta x} = -B_1 G(\xi,\eta)\left(e^{\xi}\sin\eta - \sum_{m=1}^{\infty} m p_m e^{-m\xi}\sin m\eta\right) \tag{A.33}$$

$$E^i_{zx} = -j\omega h B_1 \sum_{n=0}^{\infty} q_n \mathrm{Jo}_n(h,\xi)\mathrm{So}_n(h,\eta) \tag{A.34}$$

$$B^i_{\xi x} = B_1 G(\xi,\eta) \sum_{n=0}^{\infty} q_n \mathrm{Jo}_n(h,\xi)\mathrm{So}'_n(h,\eta) \tag{A.35}$$

$$B^i_{\eta x} = -B_1 G(\xi,\eta) \sum_{n=0}^{\infty} q_n \mathrm{Jo}'_n(h,\xi)\mathrm{So}_n(h,\eta) \tag{A.36}$$

and the coefficients p_n and q_m can be solved for in an analogous manner. It should be noted that the MCNs for the odd Mathieu functions are not the same as those of the even functions. As a result, the field patterns generated by the two orthogonal coils are not related in a simple way.

Following the derivation in [47, 150], the individual linearly polarized fields can be decomposed into two counter rotating fields, only one of which causes MR excitation. That is

$$\mathbf{B} = 1/2(B_\xi + jB_\eta)e^{j\alpha(\xi,\eta)}\mathbf{a}^+ + 1/2(B^*_\xi + jB^*_\eta)e^{j\alpha(\xi,\eta)}\mathbf{a}^- \,, \tag{A.37}$$

where * denotes complex conjugate and $\mathbf{a}^{\pm}$ represent vectors rotating at angular frequency w in the clockwise (-) and counterclockwise (+) directions. $\alpha(\xi,\eta)$ is the angle of rotation between the $(\hat{\xi},\hat{\eta})$ and $(\hat{x},\hat{y})$ coordinate systems, where

$$e^{j\alpha(\xi,\eta)} = \frac{\sinh\xi\cos\eta + j\cosh\xi\sin\eta}{\sqrt{\frac{1}{2}(\cosh 2\xi - \cos 2\eta)}} \tag{A.38}$$

The convention that the $\mathbf{a}^+$ component produces MR excitation is followed here.

A so-called circularly polarized excitation field is created by driving the linear coils 90° out of phase such that the two signal producing fields add constructively. However, in general the field produced by a linearly polarized coil will vary in magnitude and direction within the object such that the combined field from the two coils can have arbitrary elliptic

polarization. This elliptically polarized field can be decomposed into a (+) rotating field which causes the excitation and a typically weaker (-) rotating field that does not [150]. The orientation of this (+) rotating field with respect to the driving field can be interpreted as a phase shift, which we refer to as a geometric phase shift.

In general, the individual field components will be complex to reflect the phase delays caused by currents induced in the object. Geometric and inductive phase shifts combine to determine the local phase of the excitation field within the object as follows:

$$\mathrm{B}^{+} = 1/2(B_{\xi x} + jB_{\eta x} - jB_{\xi y} + B_{\eta y})e^{j\alpha(\xi,\eta)}\,. \tag{A.39}$$

Note that since the $\hat{\xi}$ and $\hat{\eta}$ directions are orthogonal, the field components B_{ξ} and B_{η} can be interpreted as being 90° out of phase. While this derivation is based on two linearly polarized coils aligned with the x and y axes, equation (A.39) is general for any combination of coils producing a circularly polarized field. Hence, it can used to predict the field pattern of a birdcage coil or a pair of linearly polarized coils not aligned with the x and y axes.

The same solutions for the field components apply when orthogonal coils are used for reception. However, the geometric phase shifts caused by reception cancel with those of the excitation field [93] whereas the phase shifts due to induced currents accumulate. Hence, the reception sensitivity is given by

$$\mathrm{R}^{+} = \mathrm{R}_0/2(B_{\xi x} - jB_{\eta x} + jB_{\xi y} + B_{\eta y})e^{-j\alpha(\xi,\eta)}\,, \tag{A.40}$$

where R_0 is a scale factor reflecting the sensitivity of the coil.

A.2.2 Simulating spin echo images

Images produced by a spin echo sequence are simulated using the excitation fields and reception sensitivity derived in the previous section. The signal measured for a spin echo

pulse sequence, as shown in [47], is given by

$$S(\xi,\eta) = \mathrm{R}^{+}(\xi,\eta) S_{SE}(\xi,\eta) \tag{A.41}$$

$$S_{SE}(\xi,\eta) = \sin^3\left(\frac{\pi}{2}\frac{|\mathrm{B}^{+}|}{B_m}\right)\exp(j\arg(\mathrm{B}^{+}))\,, \tag{A.42}$$

where S_{SE} is the emitted signal, S is the measured signal, and B_m is the nominal field strength needed to produce a 90° flip-angle. This derivation neglects relaxation and assumes complete recovery of the magnetization between repetitions. It also assumes that the pulses are non-selective or so-called hard pulses.

We refine equation (A.42) by taking into account the variations in slice profile caused by variations in excitation field strength. This is done by simulating frequency selective RF pulses using the Bloch equations [10] across the range of frequencies corresponding to a slice. The strength of the measured signal is proportional to the integral of the resulting slice profile. This simulation was carried out for a range of field strengths to determine the variations in signal intensity with field strength. A comparison of S_{SE} for selective and non-selective pulses is shown in Figure A.2. Equation (A.42) is a good approximation for selective pulses except at the high B_1 field strengths corresponding to severe intensity non-uniformity.

In simulating a spin echo image, the factor B_m is arbitrary. Typically, an MRI machine will calibrate B_m for each subject to maximize signal intensity.

A.2.3 Phantom studies

We constructed two plastic cylindrical containers with elliptic and circular cross sections respectively to validate our model of intensity non-uniformity. The circular cylinder has an inside diameter of 17.5cm, while the elliptic cylinder has major and minor diameters of 20cm and 15cm. Each cylinder was filled with various concentrations of NaCl solutions

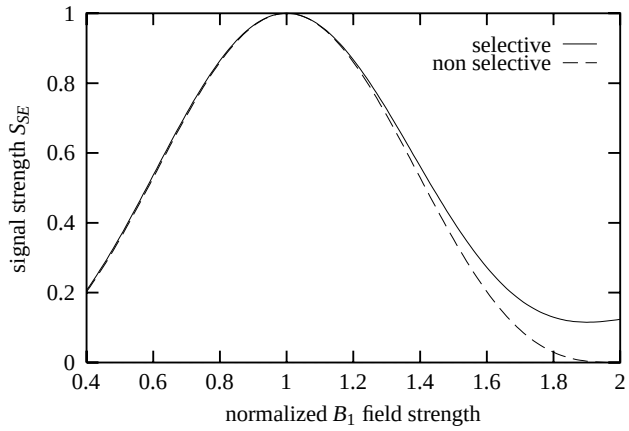

Figure A.2: Signal intensity versus B_1 field strength for selective and non-selective pulses. The results for selective pulses are based on simulation of a standard spin echo sequence for a 1.5T Siemens Vision MRI machine, which uses numerically optimized pulse profiles.

made from deionized water.

The conductivity and permittivity of each solution was computed based on the concentration of NaCl using data from [101]. The quantities of NaCl were 1.38g/L, 2.83g/L, and 58.2g/L, or roughly 24mM, 48mM, and 100mM, producing resistivities of $4.0\Omega\mathrm{m}$, $2.0\Omega\mathrm{m}$, and $1.0\Omega\mathrm{m}$ respectively. These resistivities span the range typical of biological tissues [15] at frequencies around 64MHz. At this frequency, the relative permittivity of water is essentially unchanged from its D.C. value of $\epsilon_r = 80$, which is comparable to that of brain [133] at 64MHz. In addition to NaCl, a small quantity of $\mathrm{MnCl_2}$ was added to each solution to bring its concentration to $97\mu\mathrm{M}$ and reduce T_1 relaxation times to approximately 910ms. Experiments using long repetition times (TR = 30s) showed no measurable change in intensity non-uniformity after addition of $\mathrm{MnCl_2}$.

The cylinders were designed to have a length, 40cm, such that for transverse measurements near the centre, the field patterns are essentially the same as for a cylinder of infinite

length. This is true if the cylinder is longer than twice the skin depth for the medium [47] and the region being considered is close enough to the centre to avoid variations caused by dielectric resonance along the cylinder's length. In practice, the former was found to be the more restrictive criteria. The skin depth is given by $\delta = \sqrt{2\rho/\mu\omega}$ which corresponds to between 6.3cm and 12.6cm for the given solutions.

For the experiments, the cylinders were aligned axially with the isocentre of the body coil of a 1.5T Siemens Vision MRI scanner and scanned transversally using a B_1 field mapping sequence [151] as well as a standard spin echo sequence. All images are acquired at 2mm in-plane resolution with 6mm thick slices. The spin echo sequence ($\mathrm{TR}/\mathrm{TE} = 8\,\mathrm{s}/14\,\mathrm{ms}$) had sufficiently short TE and long TR that relaxation can be neglected. The field mapping sequence is a stimulated echo technique ($90^\circ - \tau_e/2 - 90^\circ - \tau_1 - \alpha - \tau_2 - 90^\circ - \tau_e/2 - acq.$ where $\tau_e/\tau_1/\tau_2/TR = 36\mathrm{ms}/60\mathrm{ms}/8\mathrm{ms}/1\mathrm{s}$) which yields a series of images whose intensities are related by

$$S_i = a \cos b\alpha_i \,. \tag{A.43}$$

The parameters a and b are computed at each voxel by a non-linear least squares fit to the flip angles α_i and complex image values S_i. Images were acquired at $\alpha = 0^\circ,\, 40^\circ,\, \ldots,\, 400^\circ$. The resulting parameter map b is proportional to the excitation field strength, while the parameter map a is roughly proportional to spin density.

A.2.4 Comparing fields and images

The experimental data admits two types of comparisons with the theoretical model: a direct comparison of the measured excitation field with that predicted, and a comparison of the measured spin echo image with that simulated from the predicted excitation field and reception sensitivity. Before any comparisons were made all of the measured data was first

automatically registered [24, 25] with the spin density map of the corresponding simulated image by linear transformation. The effect of non-uniformity on the registration was minimized by matching smoothed gradient images rather than the images themselves. The measured field maps, which lack well defined object boundaries, were registered indirectly by registering the a parameter map to the simulation then applying the same transformation to the field map.

For quantitative comparison a common mask was defined for each pair of images within which differences could be calculated. The mask was defined by automatically thresholding each image based on its histogram [104], taking the intersection of the two masks, and eroding it by 2mm. The standard of comparison we use is the rms difference between two images computed within the common mask and expressed as a percentage of the mean intensity in the simulated image.

In the case of comparisons involving simulated spin echo images there is the factor B_m which remains uncertain. Since this factor is not readily determined for an experimental measurement, a single factor B_m is chosen to minimize the rms difference between the simulated and measured image.

A.3 Results

A.3.1 Variations in field strength

The resulting pattern of variations in image intensity can be understood by considering the simpler pattern of variations that appear in the excitation field and reception sensitivity. These in turn can be better understood by decomposing the circularly polarized field into two orthogonal linear fields acting in quadrature. Consider the field patterns arising in the elliptic and circular cylinders described earlier. We illustrate in Figure A.3 the case

of a homogeneous medium having the properties: $\mu = \mu_0$, $\epsilon_r = 80$, and $\rho = 2\,\Omega\mathrm{m}$. Figures A.3a and A.3b show the two geometries, while Figures A.3c and A.3d show the magnitude of the rotating excitation field B^+ when driven by a coil whose nominal field is oriented parallel to the minor axis of the ellipse. This linearly polarized coil produces the expected "quadrapole" pattern with brighter intensities to the top-right and bottom-left. The orientation of this diagonal pattern depends on the properties of the media as well as the eccentricity of the cylinder section.

The corresponding magnitude contours for a coil producing a field oriented along the major axis of the ellipse are shown for the two geometries in Figures A.3e and A.3f. In the case of the circular section, the field pattern is rotated by ninety-degrees, while in the case of the elliptic section the field pattern is rotated but is also more uniform. Each contour in these plots is a five percent increment in field strength. Combining the two linearly polarized cases, taking into account the ninety-degree phase difference, produces the field patterns shown in Figures A.3g and A.3h. In the case of the circular section, the low intensity regions of one coil cancel with the high intensity regions of the other to produce a field that is axially symmetric and relatively uniform. In the case of the elliptic section these regions do not fully cancel and some of the diagonal pattern remains. It is this lack of cancellation that accounts for the diagonal pattern seen in MR images of eccentric objects. It should be noted that since the fields are complex, combining the fields is not the same as adding the two magnitude images. It is also of note that despite having similar volume to the circular cylinder, the range of variation in field magnitude is greater in the elliptic cylinder.

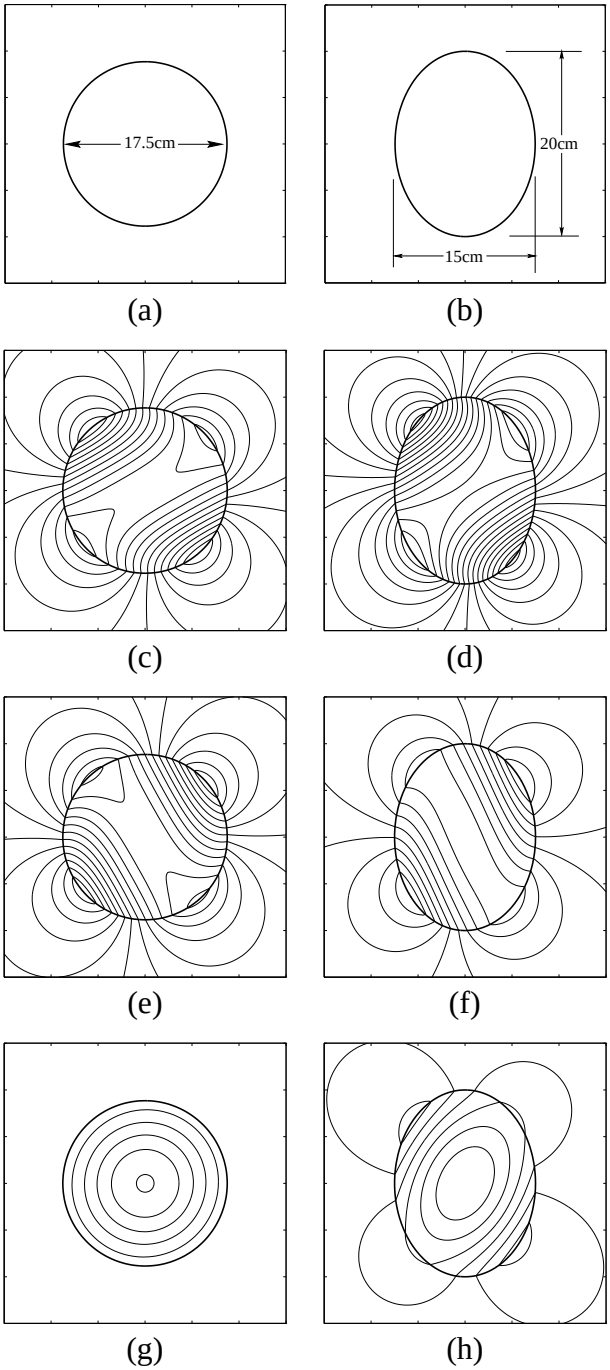

Figure A.3: Magnitude contours of B^+, the rotating component of the magnetic field resulting in excitation. Each field is normalized to have a mean of 1.0 and contours are drawn at 5% intervals. See text for explanation.

A.3.2 Simulated spin echo images

Once the excitation field and reception sensitivity have been evaluated they can be used to simulate an imaging sequence. A simulated spin echo image for an elliptic geometry having the same properties as for Figure A.3 is shown in Figure A.4. Also shown are the corresponding excitation field and reception sensitivity.

It should be noted that the pattern of non-uniformity in the spin echo image resembles neither the excitation field nor the reception sensitivity. This is caused by the apparent reversal of the excitation field to produce the sensitivity map. However, close inspection of the phase images for the two cases reveals that the excitation field and reception sensitivity maps differ by more than a reversal. In particular the geometric phase in the two cases is opposite while the inductive phase lag, dominant in this medium, remains unchanged.

Due to the symmetry of the elliptic shape, the magnitude of the excitation and reception sensitivity maps differ only by a reversal of the y axis. However, the resulting spin echo image is not symmetric as reception sensitivity makes a stronger contribution to image non-uniformity than does excitation field variation.

A.3.3 Pulse sequence sensitivity

To explain the relative contribution of excitation field and reception sensitivity variation to image non-uniformity, consider a first order perturbation on the measured signal $S = S_m + \delta S$ caused by a perturbation $B = B_m + \delta B$ to the B_1 field strength and receiver sensitivity. Substituting these expressions into equation (A.41) and treating the signal as real leads to an expression for the sensitivity of a spin echo imaging sequence

$$\begin{aligned} \frac{S_m + \delta S}{S_m} &= \frac{B_m + \delta B}{B_m} \sin^3\left(\frac{\pi}{2}\frac{B_m + \delta B}{B_m}\right) \\ 1 + \frac{\delta S}{S_m} &= \left(1 + \frac{\delta B}{B_m}\right) \cos^3\left(\frac{\pi}{2}\frac{\delta B}{B_m}\right) \end{aligned}$$

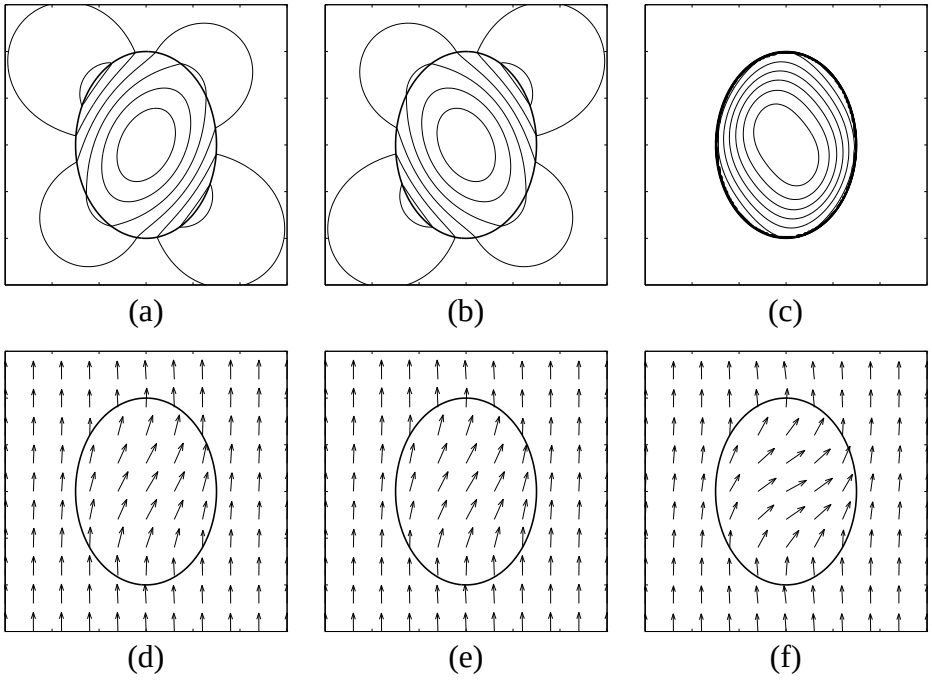

Figure A.4: Simulated spin echo images with nominal 90° and 180° flip-angles. Contours are at 5% of mean intensity. (a) and (d): magnitude and phase respectively of the excitation field B^+. (b) and (e): magnitude and phase of the reception sensitivity R^+. (c) and (f): magnitude and phase of the resulting spin echo image.

$$1 + \frac{\delta S}{S_m} = \underbrace{\left(1 + \frac{\delta B}{B_m}\right)}_{\text{reception}} \underbrace{\left(1 - \frac{3\pi^2}{8}\left(\frac{\delta B}{B_m}\right)^2 + \mathrm{O}\left(\frac{\delta B}{B_m}\right)^3\right)}_{\text{excitation}} \tag{A.44}$$

$$\frac{\delta S}{S_m} = \frac{\delta B}{B_m} - \frac{3\pi^2}{8}\left(\frac{\delta B}{B_m}\right)^2 + \mathrm{O}\left(\frac{\delta B}{B_m}\right)^3 \tag{A.45}$$

This expression represents the fractional change in measured signal caused by a given fractional variation in field magnitude and reception sensitivity.

It should be noted from equation (A.45) that, while the dependence on reception sensitivity is first order, the dependence on excitation uniformity is second order. Hence, the sequence is less sensitive to variations in the excitation field than variations in reception sensitivity.

The comparable expression for a gradient echo sequence which only involves a single 90° RF excitation and neglects relaxation effects is

$$\frac{\delta S}{S_m} \approx \frac{\delta B}{B_m} - \frac{\pi^2}{8}\left(\frac{\delta B}{B_m}\right)^2 + \mathrm{O}\left(\frac{\delta B}{B_m}\right)^3 \tag{A.46}$$

While the sensitivities of 90° gradient echo and 90°–180° spin echo sequences differ only in the second order terms, it should be noted that gradient echo sequences are commonly used with lower flip-angles. For example, the expression for the sensitivity of a gradient echo sequence with a 45° degree flip-angle is given by

$$\frac{\delta S}{S_m} \approx \left(1+\frac{\pi}{4}\right)\frac{\delta B}{B_m} + \frac{\pi}{4}\left(1-\frac{\pi}{8}\right)\left(\frac{\delta B}{B_m}\right)^2 + \mathrm{O}\left(\frac{\delta B}{B_m}\right)^3 \tag{A.47}$$

which means that the sequence is 78% more sensitive to field variations than the other two.

A.3.4 Influence of media properties

In continuing to investigate the character of intensity non-uniformity, consider the effect that the properties of the media have on the shape of the non-uniformity observed. Simulated images for a number of combinations of ϵ_r and ρ are shown in Figure A.5. Increasing the resistivity of the media from its nominal value of $2\,\Omega\mathrm{m}$ to $20\,\Omega\mathrm{m}$, as shown in Figure A.5a, decreases the image uniformity by enhancing the signal in the centre of the cylinder. This cup shaped intensity variation is normally attributed to standing wave effects. Decreasing the resistivity to $0.5\,\Omega\mathrm{m}$, as shown in A.5b, reverses the cup shaped variation and produces the strongest intensity in a rim at the edge. The reduced intensity at the centre is often described as an RF penetration effect, caused by induced currents. Reducing the relative permittivity to 40, as in A.5c, produces the most uniform image. This is consistent with making the properties of the media more like the surrounding space. Increasing the relative permittivity to 160, a value larger than typically found in biological tissue, produces

the wave like non-uniformity pattern shown in A.5d. This behaviour is consistent with the reduced wavelength being smaller than the dimensions of the cylinder. To some extent, RF penetration and standing wave effects are complementary in that one enhances the intensity near the centre while the other diminishes it. The properties of biological tissue are such that there is cancellation between the two effects, perhaps accounting for the better than predicted uniformity of 1.5T MRI images.

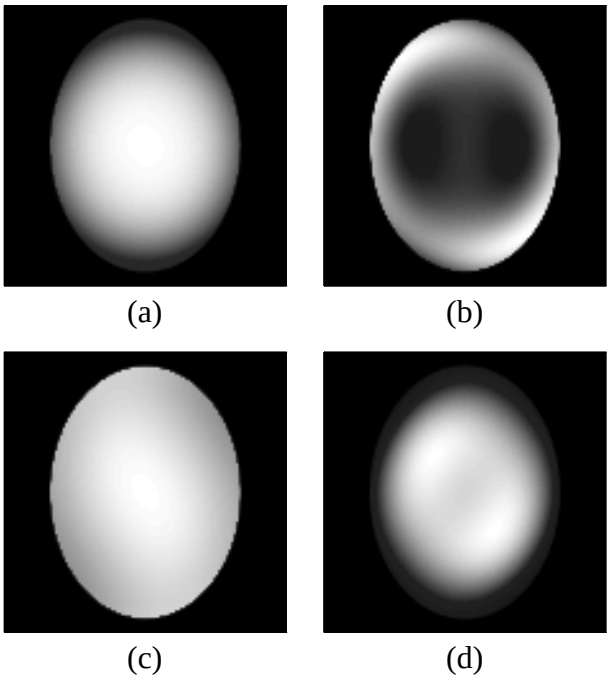

Figure A.5: Simulated spin echo images of a cylinder with elliptic section for various values of ϵ_r and ρ. (a) $\rho = 20\,\Omega\mathrm{m}$ and $\epsilon_r = 80$. (b) $\rho = 0.5\,\Omega\mathrm{m}$ and $\epsilon_r = 80$. (c) $\rho = 2\,\Omega\mathrm{m}$ and $\epsilon_r = 40$. (d) $\rho = 2\,\Omega\mathrm{m}$ and $\epsilon_r = 160$.

A.3.5 Comparison with phantom studies

Validation of our model for intensity non-uniformity is provided by comparing the predicted results with experimental results obtained from flood phantoms. The excitation field patterns were compared with direct measurements of the excitation field using the pulse sequence described previously. As the reception sensitivity cannot be measured directly, we evaluated our predictions indirectly through their impact on spin echo images.

Figure A.6 shows the excitation fields measured in the elliptic cylinder for each of the three NaCl solutions. Also shown are the predicted field patterns and the differences between the measured and predicted results. The prediction of a diagonal pattern of non-uniformity is confirmed by these experiments. When the gray scale of the difference image is expanded, it reveals minor and largely random differences between the measured and predicted images. The accuracy of the results for the circular cylinder is essentially the same.

The accuracy of the model at predicting the measured images was quantified by computing the root-mean-square (rms) difference between the two. These results are given for the two geometries and three NaCl solutions in Table A.1 along with the standard deviation (SD) of the intensity in each image. Table A.1 shows that the SD, a measure of the severity of the non-uniformity, increases with resistivity while the absolute accuracy of the model remains constant.

Figure A.7 shows the measured and predicted spin echo images for the two geometries and three solutions. The pattern of variations in these images is more complicated and the variations are more severe owing to the contribution of the reception sensitivity. Note that the orientation of the diagonal pattern in the elliptic case is reversed with respect to the excitation field map.

The accuracy of the predicted spin echo images, quantified in terms of image SD and

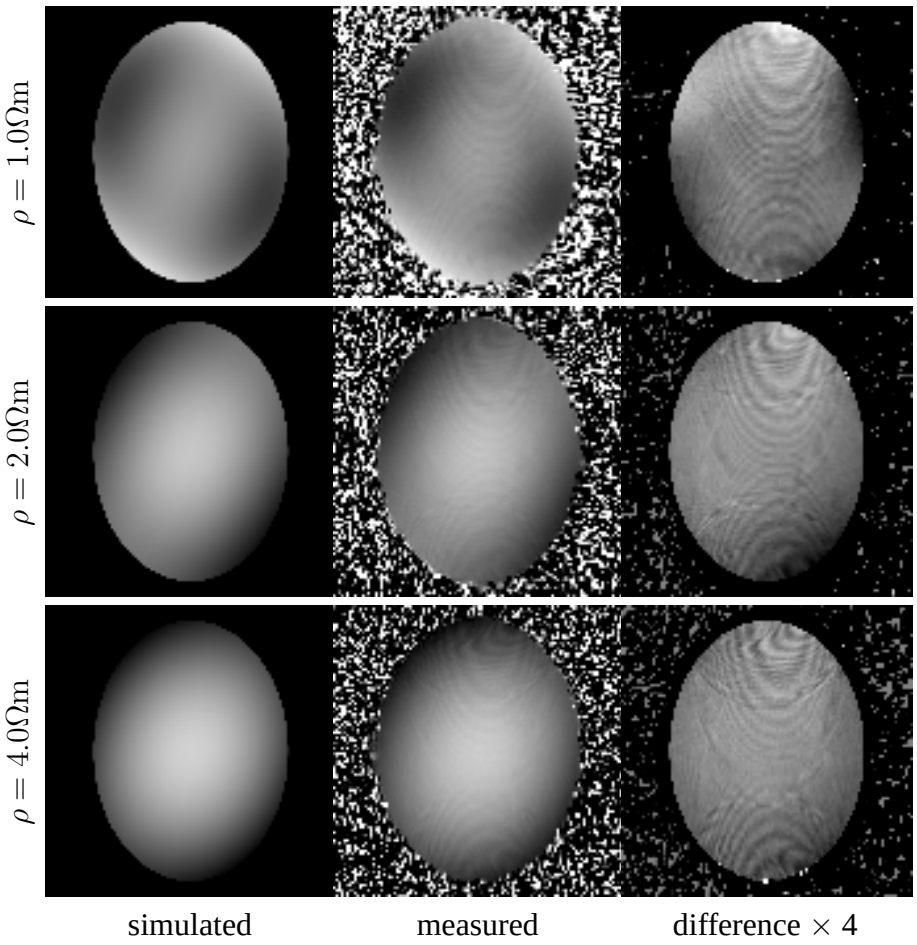

Figure A.6: Comparison of predicted and measured excitation fields B^+ in an elliptic phantom for three levels of resistivity. The normalized intensity scale for each image is 0.8 to 1.2 except for the difference images which are -0.05 to 0.05.

Table A.1: Summary of comparisons between simulated and measured excitation fields. All values are expressed as a percentage of the mean intensity in the simulated image.

	circular phantom			elliptic phantom		
	$1.0\Omega\mathrm{m}$	$2.0\Omega\mathrm{m}$	$4.0\Omega\mathrm{m}$	$1.0\Omega\mathrm{m}$	$2.0\Omega\mathrm{m}$	$4.0\Omega\mathrm{m}$
SD of simulated field	2.02%	6.05%	7.43%	5.40%	6.59%	7.42%
SD of measured field	2.31%	5.17%	6.28%	5.49%	5.98%	6.84%
rms difference	1.37%	1.37%	1.61%	1.31%	1.21%	0.99%

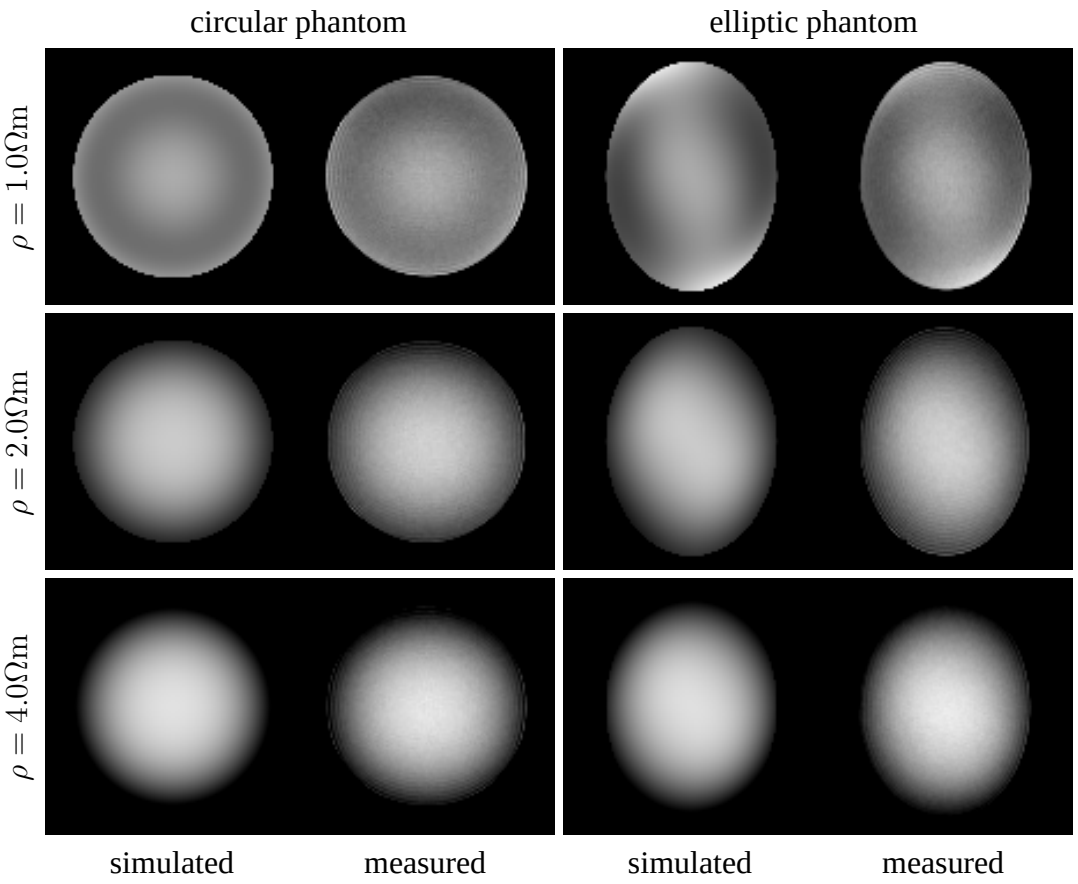

Figure A.7: Comparison of predicted and measured spin echo images for each level of resistivity. The normalized intensity scale for each image is 0.8 to 1.2.

the rms difference between measured and predicted results, is given in Table A.2. The accuracy of these results is slightly poorer than for the excitation fields; however, the non-uniformity is also more severe. Hence, in relative terms the accuracy of the predicted spin echo images is comparable to that for the excitation fields. As before, the absolute accuracy of the results remains unchanged as the resistivity increases.

Table A.2: Summary of comparisons between simulated and measured spin echo images. All values are expressed as a percentage of the mean intensity in the simulated image.

	circular phantom			elliptic phantom		
	$1.0\Omega\mathrm{m}$	$2.0\Omega\mathrm{m}$	$4.0\Omega\mathrm{m}$	$1.0\Omega\mathrm{m}$	$2.0\Omega\mathrm{m}$	$4.0\Omega\mathrm{m}$
SD of simulated image	3.09%	7.65%	10.04%	4.68%	7.98%	10.85%
SD of measured image	3.19%	7.57%	10.39%	5.22%	8.04%	11.14%
rms difference	1.83%	1.65%	1.81%	2.25%	1.83%	2.01%

A.3.6 Field variations in the human head

As a final result, a transverse image of the excitation field was acquired for a human subject using a circularly polarized body coil and the B_1 field mapping sequence described in section A.2.3. This image and a corresponding spin echo image ($TE/TR = 14\mathrm{ms}/500\mathrm{ms}$) are shown in Figure A.8. The standard deviation of field intensity computed within a hand drawn brain mask is 4.0%, comparable to that measured in the phantoms. Also note that, while less pronounced, the field map shows a diagonal pattern of variation suggestive of that observed in the elliptic phantom.

A.4 Discussion

Through an electrodynamic treatment of the MR excitation and reception process, it has been shown that an elliptic geometry imaged using circularly polarized coils produces a diagonal intensity non-uniformity pattern qualitatively similar to the quadrapole artifact observed with linearly polarized coils. Although, one would expect the circularly symmet-

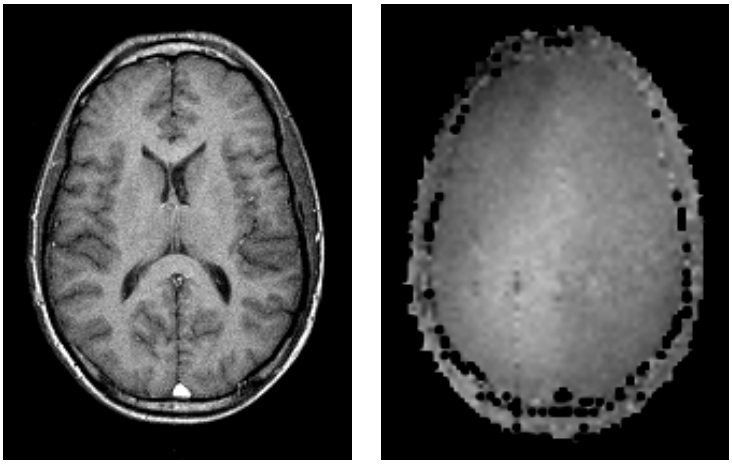

(a) (b)

Figure A.8: A transverse spin echo image (a) and corresponding excitation field map (b) for a human subject. The normalized intensity scale for the field map is 0.8 to 1.2.

ric pattern seen for circular objects to generalize to an elliptically symmetric pattern for elliptic objects, decomposition of the circularly polarized field into two linearly polarized fields acting in quadrature reveals a difference between the two cases. In particular, in the circular case the two linear fields are mirror images of one another, whereas in the elliptic case the two linear fields interact differently with the media leading to asymmetric intensity variations that do not cancel in the combined field. Such asymmetry might be incorrectly attributed to right-left hemisphere differences in a sensitive statistical analysis of neurological scans. In addition, an elliptic geometry excited by a circularly polarized field is not equivalent to a circular geometry excited by an elliptically polarized field. The impact that this asymmetry has on the intensity variations observed in typical images is further complicated by the asymmetry between the excitation field and reception sensitivity for conductive objects.

Inspection of the experimental results for the elliptic case would suggest that the recep-

tion sensitivity is the mirror image of the excitation field pattern. However, the theoretical results show a more subtle relationship. In particular, for conductive objects there is a distinction between the phase delays associated with induced currents and those inherent in imaging the object in the absence of conductivity. The cancellation of the latter between excitation and reception but not the former leads to the non-uniformity pattern in the spin echo image being more complicated than either the excitation or receptions fields. An implication of this result is that for arbitrarily shaped conductive objects, measurement of the complex excitation field is not sufficient to predict the pattern of variations in the resulting image.

While the difficulty of measuring both the excitation field and reception sensitivity has motivated the development of a variety of data driven techniques for correcting for intensity non-uniformity [28, 95, 100, 157, 139], none of these methods accurately account for the underlying physics. The fact that a diagonal pattern of non-uniformity appeared in both the scans of an elliptic phantom and a human head, suggests that one may predict the pattern of variations without a detailed model of the particular subject. Such an approach to correcting for non-uniformity would require numerical techniques to properly treat the 3D problem and to account for the influence of the smaller coils typically used in head imaging.

The good agreement between the predicted and measured results suggests that most of the non-uniformity is accounted for by the electromagnetic interactions described in the model. This agreement is achieved in spite of making no explicit assumptions of a coil producing the fields. While this is reasonable for a head sized object in a body coil, one can expect that smaller coils such as a head coil would produce some variations caused by their interaction with the object. However, in either case electromagnetic interaction with the object is the primary cause of intensity non-uniformity and further improvements in the uniformity of the unloaded coil will yield little improvement in uniformity.

A.5 Conclusions

Intensity non-uniformity is largely caused by interaction of the subject with the excitation field and reception sensitivity and will be present irrespective of the uniformity of the field produced by the unloaded coil. While the magnitude of the artifact depends on the pulse sequence, its shape has been shown to depend on geometry as well the resistive and permittive properties of the subject. In particular, an elliptic geometry is found to produce a diagonal pattern of non-uniformity. Despite the similarity between this artifact and the quadrapole artifact seen with linearly polarized coils, an elliptic geometry driven by a circularly polarized field is not equivalent to a circular geometry driven by an elliptically polarized field. While this fact prevents simple compensation for an elliptic geometry, the results of our analysis can be used as a guide in developing methods to correct for this artifact.

A.6 Computing an approximate solution

The following is the appendix to the original manuscript.

Coefficients p_m from equation (A.22) and q_n from equation (A.28) are found by matching the solutions for the interior and exterior of the cylinder as follows. Suppose that $\mathrm{Se}_n(h,\eta)$ and $\mathrm{Se}'_n(h,\eta)$ are approximated as

$$\mathrm{Se}_n(h,\eta) \;=\; \sum_{m=0}^{M} r_{mn}\cos m\eta \tag{A.48}$$

$$\mathrm{Se}'_n(h,\eta) \;=\; -\sum_{m=0}^{M} m r_{mn}\sin m\eta \tag{A.49}$$

for n = 0 . . . N. Then the coefficients r_{mn} can be taken as the terms of a matrix R. Similarly, if the cylinder boundary is taken to be $\xi = \xi_0$ then the following matrices are defined as

$$Q \;=\; [q_0 \;\; q_1 \;\; \ldots \;\; q_N]^T \tag{A.50}$$

$$P = [0 \;\; p_1 \;\; \ldots \;\; p_M]^T \tag{A.51}$$

$$J = \mathrm{diag}\left(\mathrm{Je}_0(h,\xi_0),\, \mathrm{Je}_1(h,\xi_0),\, \ldots\,,\, \mathrm{Je}_N(h,\xi_0)\right) \tag{A.52}$$

$$J' = \mathrm{diag}\left(\mathrm{Je}'_0(h,\xi_0),\, \mathrm{Je}'_1(h,\xi_0),\, \ldots\,,\, \mathrm{Je}'_N(h,\xi_0)\right) \tag{A.53}$$

$$X = \mathrm{diag}(0,\, 1,\, 2,\, \ldots\,,\, M) \tag{A.54}$$

$$Y = \mathrm{diag}\left(0,\, e^{-\xi_0},\, 2e^{-2\xi_0},\, \ldots\,,\, Me^{-M\xi_0}\right) \tag{A.55}$$

$$Z = [0 \;\; e^{-\xi_0} \;\; 0 \;\; 0 \;\; \ldots \;\; 0]^T\,. \tag{A.56}$$

where the notation $\mathrm{diag}(\cdot)$ refers to a matrix with the given elements along its diagonal.

Equating the internal and external fields at the cylinder boundary leads to the following matrix equations

$$B^i_{\xi y}(\xi_0,\eta) = B^e_{\xi y}(\xi_0,\eta) \;\Rightarrow\; XRJQ = Z + YP \tag{A.57}$$

$$B^i_{\eta y}(\xi_0,\eta) = B^e_{\eta y}(\xi_0,\eta) \;\Rightarrow\; RJ'Q = Z - YP \tag{A.58}$$

which can be solved for the coefficients p_m and q_n as

$$Q = 2(RJ' + XRJ)^{-1}Z \tag{A.59}$$

$$P = Y^{-1}(XRJQ - Z)\,. \tag{A.60}$$

Bibliography

[1] *CRC Handbook of Chemistry and Physics, 55th ed.,* pages E126–E134. CRC Press, 1974-75.

[2] M. Abramowitz and I. A. Stegun, editors. *Handbook of Mathematical Functions*. Dover, New York, 9th edition, 1972.

[3] R. S. Adler, S. D. Swanson, K. Doi, J. G. Craig, and A. M. Aisen. The effect of magnetization transfer in meniscal fibrocartilage. *Magn. Reson. Med.*, 35(4):591–5, Apr 1996.

[4] R. S. Adler and H. Y. Yeung. Transient decay of longitudinal magnetization in heterogenous spin systems under selective saturation. III solution by projection operators. *Journal of Magnetic Resonance, Series A*, 104:321–330, 1993.

[5] F. A. Alhargan. Complete method for the computations of Mathieu characteristic numbers of integer orders. *SIAM Review*, 38(2):239–255, Jun 1996.

[6] R. S. Balaban, S. Chesnick, K. Hedges, F. Samaha, and F. W. Heineman. Magnetization transfer contrast in MR imaging of the heart. *Radiology*, 180(3):671–5, Sep 1991.

[7] D. M. Bates and D. G. Watts. *Nonlinear regression analysis and its applications*. Wiley, New York, 1988.

[8] C. Beaulieu and P. S. Allen. Some magnetization properties of water in myelinated and nonmyelinated nerves. In *Second Meeting of the Society of Magnetic Resoance*, page 169, San Francisco, 1994.

[9] I. Berry, G. J. Barker, F. Barkhof, A. Campi, V. Dousset, J. M. Franconi, A. Gass, W. Schreiber, D. H. Miller, and P. S. Tofts. A multicenter measurement of magnetization transfer ratio in normal white matter. *J. Magn. Reson. Imaging*, 9(3):441–6, Mar 1999.

[10] F. Bloch, W. Hanson, and M. Packard. Nuclear induction. *Phys. Rev.*, 69:127, Feb. 1946.

[11] M. Bloom, K. T. Holmes, C. E. Mountford, and P. G. Williams. Complete proton magnetic resonance in whole cells. *J. Magn. Reson.*, 69:73–91, 1986.

[12] M. Bloom, M. I. Valic, E. E. Burnell, and S. B. W. Roeder. Nuclear magnetic resonance line shapes in lyotropic liquid crystals and related systems. *Journal of Chemical Physics*, 66(7):3012–3020, 1977.

[13] G. Bodenhausen, H. Kogler, and R. R. Ernst. Selection of coherence-transfer pathways in NMR pulse experiments. *J. Magn. Reson.*, 58:370–388, 1984.

[14] D. S. Borowiak. *Model discrimination for nonlinear regression models*. M. Dekker, New York, 1989.

[15] P. A. Bottomley and E. R. Andrew. RF magnetic field penetration, phase shift and power dissipation in biological tissue: implications for NMR imaging. *Phys. Med. Biol.*, 23(4):630–43, Jul 1978.

[16] G. Brix, L. R. Schad, M. Deimling, and W. J. Lorenz. Fast and precise T_1 imaging using a TOMROP sequence. *Magn. Reson. Imaging*, 8:351–356, 1990.

[17] B. Brochet and V. Dousset. Pathological correlates of magnetization transfer imaging abnormalities in animal models and humans with multiple sclerosis. *Neurology*, 53(5 Suppl 3):S12–7, 1999. 17 refs, Review.

[18] R. G. Bryant and C. C. Lester. Magnetic relaxation coupling in hetrogeneous systems. *J. Magn. Reson. B*, 101:121–125, 1993.

[19] G. H. Caines, T. Schleich, and J. M. Rydzewski. Incorporation of magnetization transfer into the formalism for rotating-frame spin-lattice NMR relaxation in the presence of an off-resonnace-irradiation field. *J. Magn. Reson.*, 95:558–566, 1991.

[20] T. L. Ceckler, K. Karino, P. F. Kador, and R. S. Balaban. Magnetic resonance imaging of the rabbit eye. improved anatomical detail using magnetization transfer contrast. *Investigative Ophthalmology & Visual Science*, 32(12):3109–13, Nov 1991.

[21] T. L. Ceckler, S. D. Wolff, A. Simon, V. Yip, and R. S. Balaban. Dynamic and chemical factors affecting water proton relaxation by macromolecules. *J. Magn. Reson.*, 98:637–645, 1992.

[22] J. W. Chai, C. Chen, J. H. Chen, S. K. Lee, and H. N. Yeung. Estimation of in vivo proton intrinsic and cross-relaxation rate in human brain. *Magn. Reson. Med.*, 36(1):147–52, Jul 1996.

[23] J. Charvolin and P. Rigny. Pulsed NMR in dynamically hetrogeneous systems. *J. Magn. Reson.*, 4:40–46, 1971.

[24] D. L. Collins, P. Neelin, T. M. Peters, and A. C. Evans. Automatic 3D intersubject registration of MR volumetric data in standardized Talairach space. *J. Comput. Assist. Tomogr.*, 18(2):192–205, 1994.

[25] D. L. Collins and G. Ward. MNI Automated Linear Registration Package, Version 0.98, 1997. Available by anonymous ftp at
`ftp://ftp.bic.mni.mcgill.ca/pub/mni_autoreg/`

[26] B. R. Condon, J. Patterson, D. Wyper, et al. Image non-uniformity in magnetic resonance imaging: its magnitude and methods for its correction. *Br. J. Radiology*, 60:83–87, 1987.

[27] N. P. Davies, I. R. Summers, and W. Vennart. Optimum setting of binomial pulses for magnetization transfer contrast. *J. Magn. Reson. Imaging*, 11(5):539–48, May 2000.

[28] B. M. Dawant, A. P. Zijdenbos, and R. A. Margolin. Correction of intensity variations in MR images for computer-aided tissue classification. *IEEE Trans. Med. Imag.*, 12(4):770–781, Dec. 1993.

[29] M. D. Does, C. Beaulieu, P. S. Allen, and R. E. Snyder. Multi-component T_1 relaxation and magnetisation transfer in peripheral nerve. *Magn. Reson. Imaging*, 16(9):1033–41, Nov 1998.

[30] V. Dousset, J. P. Armand, D. Lacoste, S. Mieze, L. Letenneur, J. F. Dartigues, and J. M. Caill. Magnetization transfer study of HIV encephalitis and progressive multifocal leukoencephalopathy. groupe d'epidemiologie clinique du sida en aquitaine. *AJNR Am. J. Neuroradiol.*, 18(5):895–901, May 1997.

[31] V. Dousset, B. Brochet, A. Vital, C. Gross, A. Benazzouz, A. Boullerne, A. M. Bidabe, A. M. Gin, and J. M. Caille. Lysolecithin-induced demyelination in primates: preliminary in vivo study with MR and magnetization transfer. *AJNR Am. J. Neuroradiol.*, 16(2):225–31, Feb 1995.

[32] V. Dousset, R. I. Grossman, K. N. Ramer, M. D. Schnall, L. H. Young, F. Gonzalez-Scarano, E. Lavi, and J. A. Cohen. Experimental allergic encephalomyelitis and multiple sclerosis: lesion characterization with magnetization transfer imaging [published erratum appears in radiology 1992 jun;183(3):878]. *Radiology*, 182(2):483–91, Feb 1992.

[33] V. Dousset, R. J. Grossman, K. N. Ramer, M. D. Schnall, L. H. Young, F. Conzalez-Scarano, E. Lavi, and J. A. Cohen. Experimental allergic encephalomyelitis and multiple sclerosis: Lesion characterization with magnetization transfer imagng. *Radiology*, 182:483–491, 1992.

[34] J. H. Duijn, J. H. N. Creyghton, and J. Smidt. Suppression of artifacts due to imperfect π-pulses in multiple echo fourier imaging. In *Proc. 3^{rd} Soc. Mag. Res.*, pages 197–198, 1984.

[35] H. T. Edzes and E. D. Samulski. Cross relaxation and spin diffusion in the proton NMR of hydrated collagen. *Nature*, 265:521–523, 1977.

[36] H. T. Edzes and E. D. Samulski. The measurement of cross-relaxation effects in the proton NMR spin-lattice relaxation of water in biological systems: Hydrated collagen and muscle. *J. Magn. Reson.*, 31(2):207–229, 1978.

[37] L. Ferini-Strambi, M. Bozzali, M. Cercignani, A. Oldani, M. Zucconi, and M. Filippi. Magnetization transfer and diffusion-weighted imaging in nocturnal frontal lobe epilepsy. *Neurology*, 54(12):2331–3, Jun 27 2000.

[38] M. Filippi, A. Campi, V. Dousset, C. Baratti, V. Martinelli, N. Canal, G. Scotti, and G. Comi. A magnetization transfer imaging study of normal-appearing white matter in multiple sclerosis. *Neurology*, 45(3 Pt 1):478–82, Mar 1995.

[39] M. Filippi, M. A. Rocca, G. Martino, M. A. Horsfield, and G. Comi. Magnetization transfer changes in the normal appearing white matter precede the appearance of enhancing lesions in patients with multiple sclerosis. *Ann. Neurol.*, 43(6):809–14, Jun 1998.

[40] M. Filippi, M. A. Rocca, L. Minicucci, V. Martinelli, A. Ghezzi, R. Bergamaschi, and G. Comi. Magnetization transfer imaging of patients with definite ms and negative conventional MRI. *Neurology*, 52(4):845–8, Mar 10 1999.

[41] S. Forsen and R. A. Hoffman. Study of moderately rapid chemical exchange reactions by means of nuclear magnetic double resonance. *Journal of Chemical Physics*, 39(11):2892–2901, 1962.

[42] T. A. Fralix, T. L. Ceckler, S. D. Wolff, S. A. Simon, and R. S. Balaban. Lipid bilayer and water proton magnetization transfer: Effect of cholesterol. *Magn. Reson. Med.*, 18(2):214–223, 1991.

[43] B. Fung. Nuclear magnetic resonance study of water interactions with proteins, biomolecules, membranes, and tissues. In L. Packer, editor, *Methods in Enzymology*, volume 127, page 151. Academic Press, San Diego, 1986.

[44] B. M. Fung and T. W. McGaughy. Cross relaxation in hydrated collagen. *J. Magn. Reson.*, 39:413–420, 1980.

[45] A. Gass, G. J. Barker, D. Kidd, J. W. Thorpe, D. MacManus, A. Brennan, P. S. Tofts, A. J. Thompson, W. I. McDonald, and D. H. Miller. Correlation of magnetization transfer ratio with clinical disability in multiple sclerosis. *Annals of Neurology*, 36(1):62–7, Jul 1994.

[46] G. Glover and E. Schneider. Three-point Dixon technique for true water/fat decomposition with B_0 inhomogeneity correction. *Magn. Reson. Med.*, 18:371–383, 1991.

[47] G. O. Glover, C. E. Hayes, N. J. Pelc, W. A. Edelstein, O.M.Mueller, H. R. Hart, C. J. Hardy, M. O'Donnel, and W. D. Barber. Comparison of linear and circular polarization for magnetic resonance imaging. *J. Magn. Reson.*, 64:255–270, 1985.

[48] D. F. Gochberg, R. P. Kennan, and J. C. Gore. Quantitative studies of magnetization transfer by selective excitation and T1 recovery. *Magn. Reson. Med.*, 38(2):224–31, Aug 1997.

[49] D. F. Gochberg, R. P. Kennan, M. D. Robson, and J. C. Gore. Quantitative imaging of magnetization transfer using multiple selective pulses. *Magn. Reson. Med.*, 41:1065–1072, 1999.

[50] M. Goldman. *Spin Temperature and Nuclear Magnetic Resoance in Solids*. Oxford University Press, London, 1970.

[51] M. Goldman and L. Shen. Spin-spin relaxation in $\mathrm{LaF_3}$. *Phys. Rev.*, 144:321–331, 1966.

[52] D. E. Goodkin, W. D. Rooney, R. Sloan, P. Bacchetti, L. Gee, M. Vermathen, E. Waubant, M. Abundo, S. Majumdar, S. Nelson, and M. W. Weiner. A serial

study of new MS lesions and the white matter from which they arise. *Neurology*, 51(6):1689–97, Dec 1998.

[53] J. Grad and R. G. Bryant. Nuclear magnetic cross-relaxation spectroscopy. *J. Magn. Reson.*, 90:1–8, 1990.

[54] J. Grad, D. A. Mendelson, F. Hyder, and R. G. Bryant. Applications of nuclear magnetic cross-relaxation spectroscopy to tissues. *Magn. Reson. Med.*, 17(2):452–459, 1991.

[55] S. J. Graham and R. M. Henkelman. Quantifying the magnetization transfer produced by RF irradiation with multiple frequency components. In *Proc. 4^{th} Int. Soc. Mag. Res. Med.*, volume 1, page 469, 1996.

[56] S. J. Graham and R. M. Henkelman. Understanding pulsed magnetization transfer. *J. Magn. Reson. Imaging*, 7(5):903–912, 1997.

[57] S. J. Graham and R. M. Henkelman. Pulsed magnetization transfer imaging: evaluation of technique. *Radiology*, 212(3):903–10, Sep 1999.

[58] S. J. Graham, S. Ness, B. S. Hamilton, and M. J. Bronskill. Magnetic resonance properties of ex vivo breast tissue at 1.5 t. *Magn. Reson. Med.*, 38(4):669–77, Oct 1997.

[59] D. Grenier, S. Deval, and A. Briguet. A new approach for on-resonance magnetization transfer parameter optimization. *Magma*, 7(3):131–40, Dec 1998.

[60] R. K. Gupta, M. K. Kathuria, and S. Pradhan. Magnetization transfer MR imaging in CNS tuberculosis. *AJNR Am. J. Neuroradiol.*, 20(5):867–75, May 1999.

[61] S. Hamatake, M. Onomichi, Y. Korogi, Y. Sakamoto, M. Furusawa, I. Ikushima, T. Hirai, and M. Takahashi. Determination of the optimal pulses in MR imaging with magnetization transfer contrast at 7 Tesla. *Radiation Medicine*, 15(5):335–40, Sep-Oct 1997.

[62] H. Hanyu, T. Asano, H. Sakurai, Y. Imon, T. Iwamoto, M. Takasaki, H. Shindo, and K. Abe. Diffusion-weighted and magnetization transfer imaging of the corpus callosum in Alzheimer's disease. *Journal of the Neurological Sciences*, 167(1):37–44, Aug 1 1999.

[63] R. Harrison, M. J. Bronskill, and R. M. Henkelman. Magnetization transfer and T_2 relaxation components in tissue. *Magn. Reson. Med.*, 33(4):490–6, Apr 1995.

[64] R. M. Henkelman, X. Huang, Q. S. Xiang, G. J. Stanisz, S. D. Swanson, and M. J. Bronskill. Quantitative interpretation of magnetization transfer. *Magn. Reson. Med.*, 29(6):759–66, Jun 1993.

[65] R. A. Hoffman. Transient and steady-state Overhauser experiments in the investigation of relaxation processes. Analogies between chemical exchange and relaxation. *Journal of Chemical Physics*, 45(6), Sept. 1966.

[66] B. S. Hu, S. M. Conolly, G. A. Wright, D. G. Nishimura, and A. Macovski. Pulsed saturation transfer contrast. *Magn. Reson. Med.*, 26(2):231–240, 1992.

[67] B. S. Hu, D. G. Nishimura, and A. Macovski. Pulsed magnetization transfer contrast. In *Proceedings of the Ninth Annual Meeting of the SMRM*, page 352, New York, 1990.

[68] G. Iannucci, L. Minicucci, M. Rodegher, M. P. Sormani, G. Comi, and M. Filippi. Correlations between clinical and MRI involvement in multiple sclerosis: as-

sessment using T_1, T_2 and MT histograms. *Journal of the Neurological Sciences*, 171(2):121–9, Dec 15 1999.

[69] M. Iino. Transition from Lorentzian to Gaussian line shape of magnetization transfer spectrum in bovine serum albumin solutions. *Magn. Reson. Med.*, 32(4):459–63, Oct 1994.

[70] J. Jin and J. Chen. On the SAR and field inhomogeneity of birdcage coils loaded with the human head. *Magn. Reson. Med.*, 38(6):953–963, Dec. 1997.

[71] R. A. Jones, O. Haraldseth, J. Schjott, H. Brurok, P. Jynge, A. N. Oksendal, and P. A. Rinck. Effect of Gd-DTPA-BMA on magnetization transfer: application to rapid imaging of cardiac ischemia. *J. Magn. Reson. Imaging*, 3(1):31–9, Jan-Feb 1993.

[72] S. H. Koenig. Cholesterol of myelin is the determinant of gray-white contrast in MRI of brain. *Magn. Reson. Med.*, 20(2):285–291, 1991.

[73] S. H. Koenig, R. D. Brown, M. Spiller, and N. Lundbom. Relaxometry of brain: Why white matter appears bright in MRI. *Magn. Reson. Med.*, 14(3):482–495, 1990.

[74] S. H. Koenig, R. G. Bryant, K. Hallenga, and G. S. Jacob. Magnetic cross-relaxation among protons in protein solutions. *Biochemistry*, 17(20):4348–4358, 1978.

[75] W. Kucharczyk, P. M. Macdonald, G. J. Stanisz, and R. M. Henkelman. Relaxivity and magnetization transfer of white matter lipids in MR imaging: importance of cerebrosides and pH. *Radiology*, 192(2):521–9, Aug 1994.

[76] R. R. Lee and A. P. Dagher. Low power method for estimating the magnetization transfer bound-pool macromolecular fraction. *J. Magn. Reson. Imaging*, 7(5):913–917, Sep-Oct 1997.

[77] D. Lentz, J. E. Jordan, G. B. Pike, and D. R. Enzmann. MRI in varicella-zoster virus leukoencephalitis in the immunocompromised host. *J. Comput. Assist. Tomogr.*, 17(2):313–6, Mar-Apr 1993.

[78] M. H. Levitt and R. Freeman. Compensation for pulse imperfections in NMR spin-echo experiments. *J. Magn. Reson.*, 43:65–80, 1981.

[79] F. J. Lexa, R. I. Grossman, and A. C. Rosenquist. Dyke award paper. MR of wallerian degeneration in the feline visual system: characterization by magnetization transfer rate with histopathologic correlation. *AJNR Am. J. Neuroradiol.*, 15(2):201–12, Feb 1994.

[80] J. G. Li, S. J. Graham, and R. M. Henkelman. A flexible magnetization transfer line shape derived from tissue experimental data. *Magn. Reson. Med.*, 37(6):866–71, Jun 1997.

[81] J. Listerud. Off-resonance pulsed magnetization transfer in clinical MR imaging: optimization by an analysis of transients. *Magn. Reson. Med.*, 37(5):693–705, May 1997.

[82] L. A. Loevner, R. I. Grossman, J. A. Cohen, F. J. Lexa, D. Kessler, and D. L. Kolson. Microscopic disease in normal-appearing white matter on conventional MR images in patients with multiple sclerosis: assessment with magnetization-transfer measurements. *Radiology*, 196(2):511–5, Aug 1995.

[83] L. A. Loevner, R. I. Grossman, J. C. McGowan, K. N. Ramer, and J. A. Cohen. Characterization of multiple sclerosis plaques with T1-weighted MR and quantitative magnetization transfer. *AJNR Am. J. Neuroradiol.*, 16(7):1473–9, Aug 1995.

[84] F. M. Lurie and C. P. Slichter. Spin temperature in nuclear double resonance. *Physical Review*, 133(4A):1108–1122, 1964.

[85] A. MacKay, K. Whittall, J. Adler, D. Li, D. Paty, and D. Graeb. In vivo visualization of myelin water in brain by magnetic resonance. *Magn. Reson. Med.*, 31(6):673–7, Jun 1994.

[86] S. Majumdar, A. Gmitro, S. C. Orphanoudakis, D. Reddy, and J. C. Gore. An estimation and correction scheme for system imperfections in multiple-echo magnetic resonance imaging. *Magn. Reson. Med.*, 4(3):203–20, 1987.

[87] S. Majumdar, S. C. Orphanoudakis, A. Gmitro, M. O'Donnell, and J. C. Gore. Errors in the measurements of T_2 using multiple-echo MRI techniques. I. Effects of radiofrequency pulse imperfections. *Magn. Reson. Med.*, 3(3):397–417, 1986.

[88] S. Majumdar, S. C. Orphanoudakis, A. Gmitro, M. O'Donnell, and J. C. Gore. Errors in the measurements of T_2 using multiple-echo MRI techniques. II. Effects of static field inhomogeneity. *Magn. Reson. Med.*, 3(4):562–74, 1986.

[89] P. Mansfield and P. G. Morris. *NMR Imaging in Biomedicine*, pages 181–191. Academic Press, New York, 1982. Advances in Magnetic Resonance, Suppl. 2.

[90] J. Mao and J. R. Ballinger. Power efficient on-resonance saturation pulses for magnetization transfer in magnetic resonance imaging. *Magn. Reson. Med.*, 36(3):481–6, Sep 1996.

[91] J. D. McDaniel, J. L. Ulmer, R. W. Prost, M. B. Franczak, S. Jaradeh, C. A. Hamilton, and L. P. Mark. Magnetization transfer imaging of skeletal muscle in autosomal recessive limb girdle muscular dystrophy. *J. Comput. Assist. Tomogr.*, 23(4):609–14, Jul-Aug 1999.

[92] J. C. McGowan, J. H. Yang, R. C. Plotkin, R. I. Grossman, E. M. Umile, K. M. Cecil, and L. J. Bagley. Magnetization transfer imaging in the detection of injury associated with mild head trauma. *AJNR Am. J. Neuroradiol.*, 21(5):875–80, May 2000.

[93] E. R. McVeigh, M. J. Bronskill, and R. M. Henkelman. Phase and sensitivity of receiver coils in magnetic resonance imaging. *Med. Phys.*, 13(6):806–814, Nov./Dec. 1986.

[94] R. C. Mehta, G. B. Pike, and D. R. Enzmann. Measure of magnetization transfer in multiple sclerosis demyelinating plaques, white matter ischemic lesions, and edema. *AJNR Am. J. Neuroradiol.*, 17(6):1051–5, Jun-Jul 1996.

[95] C. R. Meyer, P. H. Bland, and J. Pipe. Retrospective correction of intensity inhomogeneities in MRI. *IEEE Transactions on Medical Imaging*, 14(1):36–41, Mar. 1995.

[96] G. A. Morris and A. J. Freemont. Direct observation of the magnetization exchange dynamics responsible for magnetization transfer contrast in human cartilage in vitro. *Magn. Reson. Med.*, 28(1):97–104, Nov 1992.

[97] C. Morrison and R. M. Henkelman. A model for magnetization transfer in tissues. *Magn. Reson. Med.*, 33(4):475–82, Apr 1995.

[98] C. Morrison, G. Stanisz, and R. M. Henkelman. Modeling magnetization transfer for biological-like systems using a semi-solid pool with a super-Lorentzian lineshape and dipolar reservoir. *J. Magn. Reson. B*, 108(2):103–13, Aug 1995.

[99] S. E. Moyher, D. B. Vigneron, and S. J. Nelson. Surface coil MR imaging of the human brain with an analytic reception profile correction. *Journal of Magnetic Resonance Imaging*, 5(2):139–144, Mar./Apr. 1995.

[100] P. A. Narayana, W. W. Brey, M. V. Kulkarni, and C. L. Sievenpiper. Compensation for surface coil sensitivity variation in magnetic resonance imaging. *Magn. Reson. Imaging*, 6(3):271–274, 1988.

[101] P. S. Neelakanta. *Handbook of electromagnetic materials : monolithic and composite versions and their applications*, pages 577–584. CRC Press, 1995.

[102] A. Okumura, K. Takenaka, Y. Nishimura, Y. Asano, N. Sakai, K. Kuwata, and S. Era. The characterization of human brain tumor using magnetization transfer technique in magnetic resonance imaging. *Neurological Research*, 21(3):250–4, Apr 1999.

[103] R. J. Ordidge, R. A. Knight, and J. A. Helpern. Magnetization transfer contrast (MTC) in flash MR imaging. *Magn. Reson. Imaging*, 9(6):889–93, 1991.

[104] N. Otsu. A threshold selection method from gray-level histograms. *IEEE Transactions on Biomedical Engineering*, 9:63–66, 1979.

[105] U. J. Patel, R. I. Grossman, M. D. Phillips, J. K. Udupa, J. C. McGowan, Y. Miki, L. Wei, M. Polansky, M. A. van Buchem, and D. Kolson. Serial analysis of magnetization-transfer histograms and expanded disability status scale scores in patients with relapsing-remitting multiple sclerosis [see comments]. *AJNR Am. J. Neuroradiol.*, 20(10):1946–50, Nov-Dec 1999.

[106] M. D. Phillips, R. I. Grossman, Y. Miki, L. Wei, D. L. Kolson, M. A. van Buchem, M. Polansky, J. C. McGowan, and J. K. Udupa. Comparison of T_2 lesion volume and magnetization transfer ratio histogram analysis and of atrophy and measures

of lesion burden in patients with multiple sclerosis. *AJNR Am. J. Neuroradiol.*, 19(6):1055–60, Jun-Jul 1998.

[107] W. B. Pierce, S. E. Harms, D. P. Flamig, R. H. Griffey, W. P. Evans, and J. E. Hagans. Three-dimensional gadolinium-enhanced MR imaging of the breast: Pulse sequence with fat suppression and magnetization transfer contrast. *Radiology*, 181:757–763, 1991.

[108] G. B. Pike. Pulsed magnetization transfer contrast in gradient echo imaging: A two-pool analytic description of signal response. *Magn. Reson. Med.*, 36(1):95–103, Jul 1996.

[109] G. B. Pike, N. De Stefano, L. Fu, S. Narayanan, G. Francis, J. Antel, and D. Arnold. Magnetization transfer and proton spectroscopic imaging of multiple sclerosis. In *Third Meeting of the Society of Magnetic Resoance*, page 112, Nice, France, 1995.

[110] G. B. Pike, N. De Stefano, S. Narayanan, G. Francis, J. Antel, and D. L. Arnold. A longitudinal study of magnetization transfer in multiple sclerosis. In *Proceedings of the International Society for Magnetic Resonance in Medicine*, page 122, Sydney, Australia, 1998.

[111] G. B. Pike, N. De Stefano, S. Narayanan, K. J. Worsley, D. Pelletier, G. S. Francis, J. P. Antel, and D. L. Arnold. Multiple sclerosis: magnetization transfer MR imaging of white matter before lesion appearance on T2-weighted images. *Radiology*, 215(3):824–30, Jun 2000.

[112] G. B. Pike, G. H. Glover, B. S. Hu, and D. R. Enzmann. Pulsed magnetization transfer spin-echo imaging. *J. Magn. Reson. Imaging*, 3(3):531–539, 1992.

[113] G. B. Pike, G. H. Glover, B. S. Hu, and D. R. Enzmann. Pulsed magnetization transfer spin-echo MR imaging. *J. Magn. Reson. Imaging*, 3(3):531–9, May-Jun 1993.

[114] G. B. Pike, B. S. Hu, G. H. Glover, and D. R. Enzmann. Magnetization transfer time-of-flight magnetic resonance angiography. *Magn. Reson. Med.*, 25(2):372–9, Jun 1992.

[115] C. S. Poon and R. M. Henkelman. Practical T_2 quantitation for clinical applications. *J. Magn. Reson. Imaging*, 2(5):541–53, Sep-Oct 1992.

[116] W. H. Press, B. P. Flannery, S. A. Teukolsky, and W. T. Vetterling. *Numerical Recipes, the Art of Scientific Computing*. Cambridge University Press, Cambridge, 1986.

[117] B. Quesson, A. K. Bouzier, E. Thiaudiere, C. Delalande, M. Merle, and P. Canioni. Magnetization transfer fast imaging of implanted glioma in the rat brain at 4.7 T: Interpretation using a binary spin-bath model. *J. Magn. Reson. Imaging*, 7(6):1076–83, Nov-Dec 1997.

[118] B. Quesson, E. Thiaudiere, C. Delalande, J. . F. Chateil, C. T. W. Moonen, and P. Canioni. Magnetization transfer imaging of rat brain under non-steady-state conditions. Contrast prediction using a binary spin-bath model and a super-Lorentzian lineshape. *J. Magn. Reson.*, 130(2):321–8, 1998.

[119] B. Quesson, E. Thiaudiere, C. Delalande, V. Dousset, J. . F. Chateil, and P. Canioni. Magnetization transfer imaging in vivo of the rat brain at 4.7 T: Interpretation using a binary spin-bath model with a superLorentzian lineshape. *Magn. Reson. Med.*, 38(6):974–80, 1997.

[120] J. P. Ranjeva, J. M. Franconi, C. Manelfe, and I. Berry. Magnetization transfer with echo planar imaging. *Magma*, 5(4):259–65, Dec 1997.

[121] N. D. Richert and J. A. Frank. Magnetization transfer imaging to monitor clinical trials in multiple sclerosis. *Neurology*, 53(5 Suppl 3):S29–32, 1999.

[122] S. A. Roell, W. Dreher, and D. Leibfritz. A general solution of the standard magnetization transfer model. *J. Magn. Reson.*, 132(1):96–101, 1998.

[123] S. A. Roell, W. Dreher, and D. Leibfritz. Combining CW and pulsed saturation allows in vivo quantitation of magnetization transfer observed for total creatine by (1)H-NMR-spectroscopy of rat brain. *Magn. Reson. Med.*, 42(2):222–7, 1999.

[124] P. Roschmann. Radiofrequency penetration and absorption in the human body: limitations to high-field whole-body nuclear magnetic resonance imaging. *Med. Phys.*, 14(6):922–31, Nov-Dec 1987.

[125] G. E. Santyr, F. Kelcz, and E. Schneider. Pulsed magnetization transfer contrast for MR imaging with application to breast. *J. Magn. Reson. Imaging*, 6(1):203–12, Jan-Feb 1996.

[126] M. D. Schnall, L. Dougherty, E. Outwater, and V. Dousset. Technique for magnetization transfer imaging at 1.5T using steady state pulsed saturation. In *Proceedings of the Tenth Annual Meeting of the SMRM*, page 175, San Francisco, 1991.

[127] E. Schneider and G. H. Glover. A quantitative comparison of CW and pulsed saturation transfer. In *Proceedings of the Tenth Annual Meeting of the SMRM*, page 672, San Francisco, 1991.

[128] E. Schneider, R. W. Prost, and G. H. Glover. Pulsed magnetization transfer versus continuous wave irradiation for tissue contrast enhancement. *J. Magn. Reson. Imaging*, 3(2):417–23, Mar-Apr 1993.

[129] K. Sidaros, I. Andersen, and H. B. W. Lamson. Effect of slice profiles on the accuracy of fast T_1 measurements. In *Proc. 8^{th} Int. Soc. Mag. Res. Med.*, page 429, 2000.

[130] N. C. Silver, G. J. Barker, D. G. MacManus, D. H. Miller, J. W. Thorpe, and R. S. Howard. Decreased magnetisation transfer ratio due to demyelination: a case of central pontine myelinolysis. *Journal of Neurology, Neurosurgery & Psychiatry*, 1996.

[131] N. C. Silver, G. J. Barker, and D. H. Miller. Standardization of magnetization transfer imaging for multicenter studies. *Neurology*, 53(5 Suppl 3):S33–9, 1999. 48 refs, Review.

[132] A. Simmons, P. S. Tofts, G. J. Barker, and S. R. Arridge. Sources of intensity nonuniformity in spin echo images. *Magn. Reson. Med.*, 32:121–128, 1994.

[133] D. Simunic, P. Wach, W. Renhart, and R. Stollberger. Spatial distribution of high-frequency electromagnetic energy in human head during MRI: numerical results and measurements. *IEEE Trans. Biomed. Eng.*, 43(1):88–94, Jan 1996.

[134] T. E. Skinner and G. H. Glover. An extended two-point dixon algorithm for calculating separate water, fat, and B_0 images. *Magn. Reson. Med.*, 37(4):628–30, Apr 1997.

[135] J. G. Sled and G. B. Pike. Standing-wave and RF penetration artifacts caused by elliptic geometry: an electrodynamic analysis of MRI. *IEEE Trans. Med. Imag.*, 17(4):653–662, 1998.

[136] J. G. Sled and G. B. Pike. Correction for B_1 and B_0 variations in quantitative T_2 measurements using MRI. *Magn. Reson. Med.*, 43(4):589–593, 2000.

[137] J. G. Sled and G. B. Pike. Quantitative imaging of magnetization transfer exchange and relaxation properties in vivo using MRI. *Magn. Reson. Med.*, Sept. 2000. (submitted).

[138] J. G. Sled and G. B. Pike. Quantitative interpretation of magnetization transfer in spoiled gradient echo MRI sequences. *J. Magn. Reson.*, 145:24–36, 2000.

[139] J. G. Sled, A. P. Zijdenbos, and A. C. Evans. A non-parametric method for automatic correction of intensity non-uniformity in MRI data. *IEEE Trans. Med. Imag.*, 17(1):87–97, 1998.

[140] W. T. Sobol and M. M. Pintar. NMR spectroscopy of hetrogeneous solid-liquid mixtures. Spin grouping and exchange analysis of proton spin relaxation in a tissue. *Magn. Reson. Med.*, 4:537–554, 1987.

[141] I. Solomon. Relaxation processes in a system of two spins. *Physical Review*, 99(2):559–565, 1955.

[142] G. J. Stanisz, A. Kecojevic, M. J. Bronskill, and R. M. Henkelman. Characterizing white matter with magnetization transfer and T_2. *Magn. Reson. Med.*, 42:1128–1136, 1999.

[143] R. Stollberger and P. Wach. Imaging of the active B_1 field in vivo. *Magn. Reson. Med.*, 35:246–251, 1996.

[144] S. D. Swanson. Broadband excitation and detection of cross-relaxation NMR spectra. *J. Magn. Reson.*, 95:615–618, 1991.

[145] S. D. Swanson. Transient and steady-state effects of indirect RF saturation in heterogeneous systems. In *Proceedings of the Eleventh Annual Meeting of the SMRM*, Berlin, 1992.

[146] J. L. Tanabe, F. Ezekiel, W. J. Jagust, B. R. Reed, D. Norman, N. Schuff, M. W. Weiner, H. Chui, and G. Fein. Magnetization transfer ratio of white matter hyperintensities in subcortical ischemic vascular dementia. *AJNR Am. J. Neuroradiol.*, 20(5):839–44, May 1999.

[147] J. J. Tessier, N. Dillon, T. A. Carpenter, and L. D. Hall. Interpretation of magnetization transfer and proton cross-relaxation spectra of biological tissues. *Journal of Magnetic Resonance Series B*, 107(2):138–44, May 1995.

[148] L. O. Thomas, O. B. Boyko, D. C. Anthony, and P. C. Burger. MR detection of brain iron. *AJNR Am. J. Neuroradiol.*, 14(5):1043–8, Sep-Oct 1993.

[149] W. J. Thompson. *Angular Momentum*. John Wiley & Sons Inc., New York, 1994.

[150] P. S. Tofts. Standing waves in uniform water phantoms. *J. Magn. Reson. B*, 104:143–147, 1994.

[151] S. Topp, E. Adalsteinsson, and D. M. Spielman. Fast multislice B_1-mapping. In *Proc. 5^{th} Int. Soc. Mag. Res. Med.*, volume 1, page 281, 1997.

[152] C. Tortorella, B. Viti, M. Bozzali, M. P. Sormani, G. Rizzo, M. F. Gilardi, G. Comi, and M. Filippi. A magnetization transfer histogram study of normal-appearing brain tissue in MS. *Neurology*, 54(1):186–93, Jan 11 2000.

[153] M. A. van Buchem, J. C. McGowan, and R. I. Grossman. Magnetization transfer histogram methodology: its clinical and neuropsychological correlates. *Neurology*, 53(5 Suppl 3):S23–8, 1999.

[154] J. H. T. M. van Waesberghe, M. A. A. van Walderveen, and C. de Groot. Postmortem correlation between axonal loss, MTR, and hypointensity on T_1 SE in MS. In *Proc. 6^{th} Int. Soc. Mag. Res. Med.*, volume 2, page 1334, 1998.

[155] J. T. Vaughan, H. P. Hetherington, J. O. Otu, J. W. Pan, and G. M. Pohost. High frequency volume coils for clinical NMR imaging and spectroscopy. *Magn. Reson. Med.*, 32(2):206–18, Aug 1994.

[156] I. M. Vavasour, K. P. Whittall, D. K. B. Li, and A. L. MacKay. Different magnetization transfer effects exhibited by the short and long T_2 components in human brain. *Magn. Reson. Med.*, 44(6):860–866, 2000.

[157] W. M. Wells III, W. E. L. Grimson, R. Kikinis, and F. A. Jolesz. Adaptive segmentation of MRI data. *IEEE Trans. Med. Imag.*, 15(4):429–442, 1996.

[158] H. Wennerström. Proton nuclear magnetic resonance lineshapes in lamellar liquid crystals. *Chemical Physics Letters*, 18(1):41–44, 1973.

[159] K. P. Whittall and A. L. MacKay. Quantitative interpretation of NMR relaxation data. *J. Magn. Reson.*, 84(1):134–152, 1989.

[160] F. G. Woermann, G. J. Barker, K. D. Birnie, H. J. Meencke, and J. S. Duncan. Regional changes in hippocampal T_2 relaxation and volume: a quantitative magnetic resonance imaging study of hippocampal sclerosis. *J. Neurol. Neurosurg. Psychiatry.*, 65(5):656–64, Nov 1998.

[161] S. D. Wolff and R. S. Balaban. Magnetization transfer contrast (MTC) and tissue water proton relaxation in vivo. *Magn. Reson. Med.*, 10(1):135–44, Apr 1989.

[162] S. D. Wolff and R. S. Balaban. Magnetization transfer imaging: practical aspects and clinical applications. *Radiology*, 192(3):593–9, Sep 1994.

[163] X. Wu. Lineshape of magnetization transfer via cross relaxation. *J. Magn. Reson.*, 94:186–190, 1991.

[164] X. Wu and J. J. Listinsky. Effects of transverse cross relaxation on magnetization transfer. *J. Magn. Reson. B*, 105(1):73–76, Sept. 1994.

[165] H. N. Yeung. Transient responses of a hetrogeneous spin system to binomial pulse saturation. *J. Magn. Reson. A*, 102:8–15, 1993.

[166] H. N. Yeung, R. S. Adler, and S. D. Swanson. Transient decay of longitudinal magnetization in hetrogeneous spin systems under selective saturation. IV. Reformulation of the spin-bath-model equations by the Redfield-Provotorov theory. *J. Magn. Reson. A*, 106:37–45, 1994.

[167] H. N. Yeung and A. M. Aisen. Magnetization transfer contrast with periodic pulsed saturation. *Radiology*, 183:209–214, 1992.

[168] H. N. Yeung and S. D. Swanson. Transient decay of longitudinal magnetization in hetrogeneous spin systems under selective saturation. *J. Magn. Reson.*, 99:466–479, 1992.

[169] Y. T. Zhang, H. N. Yeung, P. L. Carson, and J. H. Ellis. Experimental analysis of T_1 imaging with a single-scan, multiple-point, inversion-recovery technique. *Magn. Reson. Med.*, 25(2):337–43, 1992.

[170] Y. Zur, M. L. Wood, and L. J. Neuringer. Spoiling of transverse magnetization in steady-state sequences. *Magn. Reson. Med.*, 21(2):251–63, Oct 1991.

[171] F. R. Zypman. MRI electromagnetic field penetration in cylindrical objects. *Computers in Biology & Medicine*, 26(2):161–175, Mar 1996.